

ROLE OF STABLE EIGENMODES IN SHEAR-FLOW INSTABILITY
SATURATION AND TURBULENCE

by

ADRIAN E. FRASER

A dissertation submitted in partial fulfillment of
the requirements for the degree of

DOCTOR OF PHILOSOPHY
(PHYSICS)

at the

UNIVERSITY OF WISCONSIN-MADISON

2020

Date of final oral examination: 8/12/2020

The dissertation is approved by the following members of the Final Oral Committee:

Paul W. Terry, Professor, Physics

Ellen G. Zweibel, Professor, Astronomy, Physics

M.J. Pueschel, Scientist, University of Texas at Austin

Chris C. Hegna, Professor, Engineering Physics

Abstract

A flow in which two fluids slide by one another or two layers of a single fluid flow at different speeds is called a shear flow. These flows are of interest in a broad range of physical systems, including atmospheric and astrophysical ones. Their potential to be unstable, with small perturbations growing by feeding off the flow's kinetic energy, motivates their study. Particularly in astrophysical systems, these instabilities often drive turbulence that dramatically modifies the rate at which heat, particles, and momentum are transported across the flow. This thesis studies the nature of these instabilities and the ensuing turbulence, investigating the canonical shear-flow instability, the Kelvin-Helmholtz (KH) instability, in three systems. Specifically, large-scale stable modes are explored, which transfer energy from perturbations back to the shear flow and tend to decay in time, in contrast to unstable modes which take energy away from the flow and tend to grow.

In systems where stable modes were investigated prior to this work, the same nonlinear interactions that transfer energy from large to small scales were shown to transfer energy from unstable to stable modes. Thus, they can potentially reach significant amplitudes despite their tendency to decay in the absence of nonlinear interactions. At large amplitudes, the energy sink they present can significantly modify the turbulent state, and accounting for them can significantly improve reduced models of turbulent transport. These prior studies all concerned plasma micro-instabilities or systems that were otherwise quasi-homogeneous. The KH instability is importantly macroscopic and inhomogeneous.

Thus, this thesis presents a significant expansion to the set of systems in which stable modes have been investigated.

Three studies are described in this thesis. Each study concerns a different flow configuration and a different set of physical effects: a piecewise-linear, fixed shear layer in hydrodynamics, a reinforced, sinusoidal shear flow in gyrokinetics, and a smooth, freely-evolving shear layer in MHD. It is shown that stable modes are nonlinearly coupled to unstable modes in each system. When stable modes are not suppressed by added physical effects, the transfer of energy from unstable to stable modes plays an important role in saturation, and stable modes are expected or directly shown to be excited to significant amplitudes in the ensuing turbulence. The excitation of stable modes is linked to the transport of momentum against its gradient, an effect previously observed in experiments. It is shown that accounting for stable modes can significantly improve reduced models of momentum transport in regimes where they reach significant amplitude.

The major contributions of this work are twofold. First, nonlinear coupling to large-scale stable modes is shown to be a generic feature of KH-unstable shear flows. Stable modes are shown to provide a valuable interpretive framework for explaining how features of the turbulence change with system parameters (e.g. understanding why adding a magnetic field in the direction of the shear flow enhances small-scale fluctuations), and they inform improvements to reduced models. Second, in carrying out this work, tools developed for studying stable modes in quasi-homogeneous systems have been extended to apply to inhomogeneous systems, with stable modes shown to be relevant in inhomogeneous systems for the first time. Thus, this work motivates investigations into stable modes more broadly in inhomogeneous systems and provides the necessary tools for these investigations.

Further details of each study are given in the abstracts of Chapters 2, 3, and 4.

Dedication

To my brothers, Andrew and Jamie.

Acknowledgments

First and foremost I am grateful to my advisors Paul Terry and Ellen Zweibel for their brilliant mentorship, the outstanding work environments they provided in which I was able to learn and grow as a scientist, and the examples they set as exceptional and ethical researchers, instructors, and academic community members. I am also grateful to my mentor and collaborator M.J. Pueschel for teaching me so many of the practical details of academia and for getting me started on high performance computing, working with pseudospectral codes, and gyrokinetics. Thanks also to the exceptional graduate-level plasma physics, fluid dynamics, and quantum mechanics instructors I had, who are too many to list, but whose dedication to outstanding teaching provided me with the strong background I needed to conduct this research.

The outstanding work environments I was lucky to be a part of would not have been half as enjoyable without the peers and friends I got to know in Paul and Ellen's groups. I'm especially thankful to have worked with Chad,

whose brilliant ideas for what we would do if we left the program eased some of the anxieties first years face in our program, Jacqueline, who is responsible for most of what I know about stellar oscillations, science communication, and organizing work, and the Cascave, including Ben, Garth, Ian, Jason, Justin, and Zach, for the camaraderie and helpful discussions over the years.

Thank you to everyone I met through the TAA, everyone who got involved in PGSC over the years, and the people who started the important conversations in our department: GMaWiP and especially Emily Lichko. These communities helped show what grad student advocacy can do, and that some of the uglier sides of academia can be addressed with hard work. Thanks also to Lisa Everett for her incredible efforts to listen to and guide students and address various concerns.

Thank you to the Dedalus developers for creating such an outstandingly flexible and user-friendly code that made much of the work presented in this thesis possible, and for their tireless efforts supporting the user group by answering questions on the group page. Special thanks to Daniel Lecoanet and Keaton Burns for several lengthy and helpful discussions on both the physics and code aspects of my work involving Dedalus.

To Jack Schroeder, thank you for all your hard work that you put into our collaboration, especially when paying you was no longer possible.

Without your contribution, the calculation would still just be a speculative idea.

Finally, I can't possibly thank Kendra Turk-Kubo and Mike Kubo enough for the endless kindness they showed me when I first arrived in Santa Cruz. They helped in more ways than are reasonable to list here, but above all they made sure I was situated and felt welcomed. Without them, the final stretch towards defending would have been extremely stressful and difficult.

Contents

Abstract	i
Contents	vii
List of Tables	xii
List of Figures	xiii
1 Introduction	1
1.1 Shear flow	1
1.2 Stable modes	7
1.3 Thesis summary	13
References	20
2 Shear flow instability saturation, hydrodynamics	22
Abstract	23
2.1 Introduction	24
2.2 Linear Modes	29
2.3 Eigenmode Projection	35

2.4	The Threshold Parameter	44
2.5	Momentum Transport	52
2.6	Conclusion	55
A	Coupling Coefficients	57
	References	59
3	Driven shear flows, gyrokinetics	61
	Abstract	62
3.1	Introduction	63
3.2	Shear Flow Instability	69
3.2.1	Rayleigh's Stability Equation	69
3.2.2	Kolmogorov Flow	71
3.2.3	Numerical implementation and benchmarking	72
3.2.4	Forcing and dissipation terms	78
3.3	Eigenspectrum	81
3.3.1	Subdominant modes	81
3.3.2	Forcing and dissipation effects	84
3.4	Instability saturation	85
3.4.1	Saturation and decaying turbulence	85
3.4.2	Driven turbulence	87
3.4.3	Momentum transport	90

3.5	Eigenmode analysis	93
3.5.1	Eigenmode Expansion	93
3.5.2	Truncated eigenmode expansions	99
3.5.3	Influence of forcing and dissipation	102
3.5.4	Influence of stable modes in analytical models	105
3.6	Conclusions	109
	References	114
4	Free shear layer, MHD	118
	Abstract	119
4.1	Introduction	121
4.2	System setup	127
4.2.1	Equilibrium, governing equations	127
4.2.2	Perturbation equations	129
4.2.3	Numerical implementation	131
4.3	Eigenmodes, eigenvalues for the $U = \tanh(z)$, $B_x = 1$ equilibrium	134
4.4	Hydrodynamic evolution	140
4.5	MHD system, weak-field regime	144
4.5.1	Flow, field features	147
4.5.2	Energy content	149

4.5.3	Momentum transport	156
4.5.4	Directly calculating stable mode excitation	162
4.5.5	Approximating fluctuations with truncated eigenmode decompositions	170
4.6	Conclusions	173
A	Constructing a basis with the linear modes	177
B	Details of inner product used in this work	182
C	Nonlinear coupling of linear modes	183
	References	190
5	Summary and Conclusions	194
5.1	Summary and conclusions	195
5.2	Future work	198
	References	203

List of Tables

List of Figures

2.1	Dispersion relation for the hydrodynamic system	33
2.2	Eigenmode structures for the hydrodynamic system	35
2.3	Coupling coefficients for the hydrodynamic system	44
2.4	Contributions to saturation in the hydrodynamic system . .	47
2.5	Eigenmode amplitudes, truncated hydrodynamic system . .	50
2.6	Superpositions of different eigenmodes, hydrodynamic system	52
3.1	Dispersion relation for the gyrokinetic system	75
3.2	Eigenvalue spectra for the gyrokinetic system	80
3.3	Eigenmode structures for the hydrodynamic system	83
3.4	Energy timetraces, gyrokinetic simulations	85
3.5	Flow snapshots, unforced gyrokinetic simulations	87
3.6	Flow snapshots, driven gyrokinetic simulations	89
3.7	Forcing and Reynolds stress force balance, gyrokinetic simu- lations	91

3.8	Eigenmode amplitudes, gyrokinetic simulations	94
3.9	Flow approximations with truncated eigenmode expansions, gyrokinetic simulations	100
3.10	Quantifying error for truncated eigenmode expansions, gy- rokinetic simulations	101
3.11	Influence of damping on stable, unstable mode excitation, gyrokinetic simulations	103
3.12	Influence of forcing on stable, unstable mode excitations, gyrokinetic simulations	104
3.13	Comparing reduced models with and without stable modes included, gyrokinetics	107
4.1	Dispersion relation, MHD shear layer	135
4.2	MHD Eigenmodes	137
4.3	Eigenmode Reynolds and Maxwell stresses	139
4.4	Kinetic energy timetraces, hydrodynamics	142
4.5	Flow snapshots, hydrodynamics	145
4.6	Reynolds stress, mode amplitude correspondence	147
4.7	Flow and field snapshots, MHD	148
4.8	Energy timetraces, MHD	150
4.9	Dissipation timetraces, MHD	154

4.10 Mean flow kinetic energy timetrace	155
4.11 Momentum transport breakdown	157
4.12 Momentum transport, M_A scan	160
4.13 Growth rate over time with quasilinear flattening	166
4.14 Mode amplitudes, MHD	168
4.15 Mode amplitudes, M_A scan	170
4.16 Truncated mode decomposition, $M_A = 40$, $k_x = 0.2$	172
4.17 Truncated mode decomposition, $M_A = 40$, $k_x = 0.4$	174
4.18 Truncated mode decomposition, $M_A = 7.5$, $k_x = 0.2$	174
4.19 Coupling coefficients, MHD	188
4.20 Threshold parameter, MHD	191

Chapter 1

Introduction

1.1 Shear flow

When one fluid, whether a liquid, gas, or plasma, flows along another one at a different velocity, or when two layers of a single fluid flow along each other at different velocities, that flow configuration is broadly referred to as a *shear flow*. Shear flows are ubiquitous in everyday life: when wind flows over the surface of a lake, when one blows air over hot soup to cool it, or when fluids move through pipes, as the outer rings of the flow generally move slower than the inner regions due to friction. When the flow shear is mostly confined to a narrow region between two fluids that are otherwise in generally uniform motion, as in the case of wind over the surface of a lake, that region is called a *shear layer*.

Shear flows are similarly ubiquitous in space and astrophysical systems.

In accretion disks, or disk-shaped structures that rotate around a new star or black hole that slowly leaches matter from the disk, neighboring rings of the disk rotate at different rates, producing a rotational flow shear (Balbus & Hawley 1998). When the solar wind flows past the Earth's magnetosphere, a shear layer is observed between them (Faganello & Califano 2017). When relativistic jets are launched from active galactic nuclei, a shear layer is expected at the interface between the jet and the surrounding medium, and the flow within the jet is expected to be sheared as well (Rieger 2019). Shear flows are important in laboratory plasmas too, with one prominent example being the flow shear that exists in the pedestal region of tokamaks operating in H-mode regimes (Wagner 2007).

Shear flows are of significant interest to scientists in many fields not only because they are so common, but because they can play a crucial role in the systems where they are found. This often stems from their potential to be unstable, with small perturbations growing by feeding off the kinetic energy of the flow and disrupting the system. While air blowing over the surface of a lake is an equilibrium configuration (neglecting viscosity), it can be unstable. If the wind is fast enough, the slightest perturbation will disrupt the steady, horizontal layer between the two fluids and cause waves to form. This instability of a shear layer between two fluids in uniform motion

relative to one another is referred to as the *Kelvin-Helmholtz instability* (or KH instability), named after two scientists who studied it in the 19th and early 20th centuries (see Chandrasekhar 1961, and references therein for a brief historical review). This name is often used to refer generically to other sufficiently-similar instabilities as well, as will be done in this thesis.

These instabilities modify the flows where they are found by disrupting shear layers with the formation of large waves or even coherent vortices. For this reason, shear-flow instabilities have been studied in detail for several decades. Topics of interest include different flow configurations that can be unstable, the growth rate and shape of the waves that initially emerge, and how these are affected by properties of the fluid such as its density or flow speed. For the category of shear flow instabilities discussed in this thesis, these properties can all be obtained by performing *linear stability analyses* (Chandrasekhar 1961; Drazin & Reid 1981; Drazin 2002).

The instability of these flows is only half of why they are important to study, and these linear stability properties are very much the easier half. The other half lies in how the growth of these perturbations ceases, or how the instability *saturates*, and what follows. After the disturbances become sufficiently large, they often lead to a state of *turbulence* – roughly defined as chaotic fluctuations interacting with each other across a range of spatial

scales, from the large scale of the flow shear to a small scale determined by viscosity or similar effects. These fluctuations can advectively transport heat, particles, and momentum across the flow at a much higher rate than diffusion and viscosity alone would in the absence of instability. Thus, the instability and ensuing turbulent transport due to the shear layer between the Earth's magnetosphere and the solar wind, for example, might play a crucial role in determining the transport of solar wind particles into the magnetosphere (Faganello & Califano 2017).

Predictions for these transport properties are not given by linear stability analyses alone and are often challenging to obtain reliably. Turbulence is famously complex, making predictions of the enhanced transport that it brings elusive. Standard efforts generally employ potentially-severe simplifying assumptions for the nature of the turbulent state, expensive numerical simulations, or both. A common class of simplifying assumptions in this context, sometimes called a *quasilinear* model or approximation, involves approximating the turbulent state with the growing perturbations obtained from linear stability analyses (e.g. Garaud 2001). Often the overall amplitude, and hence the turbulent transport, is assumed to scale like the growth rate of the instability (e.g. Whelan et al. 2018), so that variation in transport as system parameters change can be predicted by performing simple

linear stability analyses at different parameters. This can be compared to turbulent viscosity models used in stellar evolution codes (e.g. Heger et al. 2000; Paxton et al. 2013). Many examples that contradict these scaling arguments exist, however. Of particular relevance to one of the studies in this thesis, previous work has shown that the momentum transport in KH-driven turbulence *increases* when a uniform magnetic field in the direction of the flow is added (Palotti et al. 2008; Mak et al. 2017). This contradicts expectations from quasilinear models because the growth rate of the instability *decreases* with an added magnetic field, as the tension in the field lines tends to suppress the growth of waves as they distort the shear layer (Chandrasekhar 1961). Thus, with less free energy transferring from the shear flow to the perturbations, one might expect weaker turbulence and less transport, when in fact the opposite occurs.

Generally, a combination of analytical approaches and direct numerical simulations are used to model turbulent transport. The previously-mentioned accretion disk system serves as an example where this turbulent transport is important and where models are still sought. The rate at which matter falls onto the central object is directly tied to the rate at which angular momentum is transported outward by the shear flow. However, the inferred infall rate based on observations in various systems is far greater

than what is predicted based on viscous angular momentum transport alone. Turbulence driven by shear flow instability is believed to provide the necessary enhanced transport (Balbus & Hawley 1998). But like many turbulent astrophysical systems, the range of scales over which this turbulence exists is so large, due to the system's large size and the vanishingly small viscosity, that it cannot be accurately simulated on modern supercomputers. Instead, models are often developed in simplified systems that supercomputers are able to simulate (e.g. with increased viscosity), and then extrapolated to the more realistic systems. *The first of two central motivations for this work is the need for models that can be tested in numerically tractable regimes, then extrapolated to physically relevant but numerically intractable regimes.*

In a very different context than shear flows – plasma microturbulence driven by instabilities in the cores of fusion devices – accurate, reduced transport models have been constructed by studying in greater detail how the instabilities initially saturate (for recent examples see Whelan et al. 2018; Terry et al. 2018; Hegna et al. 2018). These saturation studies leverage previously-ignored properties of the instabilities, namely the existence of *stable modes*, which are described in the following section. When the work presented in this thesis began, stable modes had not been investigated as a saturation mechanism outside of a set of instabilities mostly relevant to the

cores of fusion devices. *The second central motivation for this work is to explore whether stable modes are relevant to a broader range of instabilities than they had previously been studied in*, starting with unstable shear flows.

1.2 Stable modes

When a parent applies periodic forcing to a child on a playground swing, the amplitude of the swinging motion increases if the forcing has the right phase relative to the swinging motion, with energy transferring from the parent to the swinging child. If the relative phase between the forcing and swinging is changed, the transfer of energy reverses, and the applied forcing slows the child down. Similarly, the transfer of energy can reverse between unstable equilibria and their perturbations. In the case of an unstable shear layer, small perturbations grow in amplitude by feeding off of the kinetic energy of the flow, with linear stability analyses yielding the shapes of the growing perturbations driven by the flow, called unstable modes. Linear stability analyses also reveal the existence of stable modes, or perturbations of a particular shape such that they transfer energy *back* to the shear flow, decreasing their amplitude (Chandrasekhar 1961; Drazin & Reid 1981).¹ A generic, random perturbation can be a combination

¹Perturbations that tend to decay due to viscosity or resistivity are also called stable modes, but they are generally smaller in scale than the unstable and stable modes studied here. Also, to avoid confusion, modes whose amplitudes remain unchanged by the shear flow will be referred to as marginally stable modes

of many different modes, including stable and unstable, so that energy is simultaneously being transferred from the shear flow to the perturbation and from the perturbation to the shear flow². In incompressible hydrodynamic systems, the Reynolds-Orr energy equation (see Eq. 5.28 in Drazin 2002) relates the energy transfer between a perturbation and shear flow to the associated momentum transport across the flow by the perturbation. As a result, transfer from the shear flow to the perturbation via unstable modes directly corresponds to down-gradient momentum transport, and transfer from the perturbation to the shear flow via stable modes directly corresponds to counter-gradient momentum transport (this can be compared to the contributions of stable and unstable modes to transport in other systems, see, e.g., Terry et al. 2006, 2009). This counter-gradient momentum transport has been observed in laboratory experiments of shear layers (e.g. Ho & Huerre 1984; Hurst et al. 2020), providing evidence that stable modes are excited in unstable shear flows (see also Qian & Mauel 2020, for measurements of stable mode excitation in a different system). However, the observed counter-gradient transport in unstable shear flows had not

throughout this thesis.

²In simple systems, e.g. hydrodynamic and unstratified, energy transfer to and from the shear flow is the entirety of what these large-scale stable and unstable modes do. But if, say, magnetic fields or density stratification are considered, then energy transfer to and from the background might also take the shape of field amplification or modification of the background density gradient.

previously been connected to stable mode activity.

If stable modes had no other source of energy, they would gradually decay and eventually vanish as they transfer all their energy to the shear flow. This raises the question of how they can be observed in experiments despite this tendency to decay. As stated in the previous section, a characteristic feature of turbulence is the constant, chaotic interaction between fluctuations of different sizes – small and large eddies emerging and decaying and exchanging energy. Previous work in the context of fusion devices showed that these same interactions transfer energy from unstable modes, which are constantly gaining energy from the unstable equilibrium, to stable modes, which are constantly losing energy by their interaction with the equilibrium (Terry et al. 2006). Thus, stable modes can resist their tendency to decay in amplitude provided they gain a sufficient amount of energy from unstable modes.

If the rate of energy transfer from unstable modes to stable modes reaches the rate that energy flows into unstable modes from the equilibrium, the unstable modes must stop growing. This presents a means by which an instability can saturate. Two other important saturation mechanisms are a scenario in which the source of free energy driving the instability is

sufficiently exhausted that the transfer to unstable modes halts³, here called *quasilinear flattening*, or one in which the energy transferred into unstable modes is balanced by a transfer of energy to smaller scales where that energy is dissipated by processes like viscosity.

Previous work developed methods for calculating analytically how this unstable-to-stable energy transfer compares to the transfer to small scales, so that systems where large-scale stable modes are important can be distinguished from those where they are less important (Terry et al. 2006; Makwana et al. 2011). Additional methods were developed for analyzing numerical simulations of instability-driven turbulence, including decomposing the fluctuations into stable and unstable mode contributions (Hatch et al. 2011; Terry et al. 2014), demonstrating that in regimes where stable modes affect instability saturation, they are also found to be excited to large amplitudes in the ensuing turbulence. This has important consequences to reduced models of turbulent transport. Many models assume for simplicity that the large-scale fluctuations in the turbulence are dominated by the most-unstable modes. Where the excitation of other modes, including stable ones, has been demonstrated, it has also been shown that these models can be improved by relaxing this assumption and

³For example, in instabilities driven by a temperature gradient, if the gradient relaxes so that previously-unstable modes are no longer unstable (Böhm-Vitense 1958)

including the effects of additional modes (Pueschel et al. 2016; Whelan et al. 2018). This thesis demonstrates that the same is often true for KH-driven turbulence.

These previous studies investigated plasma turbulence driven by many different instabilities, finding stable modes to be important in a broad range of systems (e.g. Makwana et al. 2011). However, they were generally systems relevant to fusion devices, and the characteristic length scales of the unstable modes and the turbulent fluctuations were much smaller than the scales of the gradients driving the instabilities. As is explained in greater detail in Chapter 2, this allows for a quasi-homogenous – or local, as opposed to global – description that simplifies these stable mode calculations. However, this leaves unanswered whether the seemingly-universal nature of these stable mode effects are limited to quasi-homogeneous systems, or whether stable modes are relevant more generally in systems of instability-driven turbulence that are not quasi-homogeneous, including many astrophysical scenarios.

In this thesis, both analytical (Terry et al. 2006; Makwana et al. 2011) and numerical (Hatch et al. 2011; Terry et al. 2014) methods employed previously to study stable mode activity are applied to KH-unstable shear flows. Three different flow profiles and three different physical models (hydrodynamic, gyrokinetic, and magnetohydrodynamic, or MHD) are considered.

The connection between counter-gradient momentum transport and stable modes is made explicit. It is shown that stable modes are generally driven by unstable modes to a significant amplitude where they affect instability saturation and turbulent momentum transport – with some exceptions depending on system parameters – and that accounting for them can improve reduced models of momentum transport. As will be shown in Chapter 2, the KH instability is inherently non-local. To investigate stable mode physics in KH-driven turbulence therefore requires adapting existing methods to apply to more generic systems. By finding that stable modes are important, this work establishes that their importance extends beyond quasi-homogeneous, fusion-relevant systems and includes a broader range of instabilities.

An additional feature of previous systems where stable modes were investigated is that the driving gradients were held fixed. This precludes quasilinear flattening as a saturation mechanism.⁴ Thus, only saturation by transfer to large-scale stable modes or to small, dissipative scales was permitted. In Chapter 4 of this thesis, a system where quasilinear flattening is allowed to occur is studied. While relaxation of driving gradients significantly complicates the analyses, stable modes are still shown to be

⁴This also causes the energy transfer from the perturbation to the equilibrium by stable modes to be non-conservative: the energy lost via stable modes is not accounted for in a corresponding increase in energy of the equilibrium, because it is held fixed. Likewise for unstable modes. This is explained in greater detail in Chapter 4.

driven by coupling to unstable modes and to affect turbulent momentum transport as long as other effects unique to that system do not dominate.

1.3 Thesis summary

The previous sections explained why shear flows are of broad importance and what particular aspect of shear flows are investigated in this thesis, as well as how this work fits into and extends an existing body of work on stable modes. This thesis is composed of three different investigations, each described in a separate chapter, summarized here.

The first investigation, published in Fraser et al. (2017), forms Chapter 2 of this thesis. There, the role of stable modes in instability saturation for an unstable shear layer was studied analytically for a simplified, idealized, hydrodynamic system: a two-dimensional, incompressible, inviscid fluid of uniform density, with a base flow profile, corresponding to a shear layer of finite width, that was artificially held fixed. The flow was in the horizontal direction and varied in the vertical direction in a piecewise-linear way, with the flow velocity uniform above and below the layer, and the shear (derivative with respect to the vertical coordinate of the horizontal flow) constant within the layer. Because the linear modes in this system have nontrivial structures that extend on either side of the layer, the local descriptions used in quasi-homogeneous systems are not

appropriate. However, by focusing on the dynamics at the edges of the layer, equations that are mathematically similar to those in previously-studied quasi-homogeneous systems were recovered. This allowed the role of stable modes relative to other modes in instability saturation to be calculated using existing methods. The threshold parameter P_t (Terry et al. 2006; Makwana et al. 2011), which evaluates the relative contributions to saturation of the instability by energy transfer to stable modes versus other modes, was calculated in a shear flow system for the first time. Stable modes were shown to be nonlinearly coupled to unstable modes in a shear flow, with sufficient energy transfer from unstable to stable modes relative to other energy transfer channels that stable modes play an important role in saturation. It was also shown how they can be expected to reduce or even reverse the transfer of momentum relative to the transport induced by unstable modes alone, making explicit their connection to counter-gradient momentum transport.

In this first study, the coupling between unstable and stable modes was assessed at instability saturation, but the calculation did not extend to the ensuing turbulence, and did not yield the specific amplitudes of individual modes. These mode amplitudes are necessary for assessing in detail the impact on momentum transport, so while the potential for a significant

impact was demonstrated, quantitative details remained to be shown. This motivated the next investigation.

To study KH-driven turbulence in greater detail, the second study, which is published in Fraser et al. (2018) and forms Chapter 3 of this thesis, concerns direct numerical simulations of an unstable shear flow. The numerical methods for investigating stable mode excitation used in Hatch et al. (2011) and Terry et al. (2014) are applied here. The flow profile considered was a horizontal flow that varied sinusoidally in the vertical direction.⁵ The flow was maintained against quasilinear flattening by a sinusoidal body forcing resembling Hook’s law: at each time, the applied force was proportional to the difference between the initial equilibrium flow and the horizontally-averaged flow, with the constant of proportionality a free parameter. While the ensuing dynamics were essentially hydrodynamic, the simulations were carried out in the gyrokinetic framework. The KH instability is of interest as a possible tertiary instability in the cores of fusion devices (Rogers & Dorland 2005), where the gyrokinetic framework is often applied. Although the KH instability is stabilized by a sufficiently strong, flow-aligned magnetic field, and a strong magnetic field is a fundamental assumption built into the gyrokinetic framework, the instability can still

⁵Reader beware: in Chapters 2 and 4, the “horizontal” direction of flow is x and the “vertical” direction of shear is z , while in Chapter 3 the flow is in y and varies in x .

exist if the equilibrium flow and its gradient are perpendicular to this strong magnetic field, as is the case here.

While the KH instability is relevant to systems where the gyrokinetic framework is often applied (Rogers & Dorland 2005) and the instability can be studied in this framework, a more practical motivation for the use of the gyrokinetic framework here was the particular simulation code that was used: the GENE code (Jenko et al. 2000). The same code was used previously to study stable modes in instability-driven turbulence (e.g. Hatch et al. 2011; Terry et al. 2014), so many of the necessary numerical tools for this study had already been developed. Specifically, calculating the excitation of different modes in a turbulent state not only requires nonlinear initial value calculations but also eigenvalue capabilities that yield left eigenvectors (Hatch et al. 2011; Terry et al. 2014). Thus, this study could more easily be performed in the gyrokinetic framework than it could with a fluid model using a different code, where these extra capabilities would likely need to be developed first.

This second study showed that, consistent with the hydrodynamic case, stable modes are nonlinearly driven by unstable modes leading into saturation of the KH instability in gyrokinetics and remain excited in the turbulent state. Furthermore, in simulations where an added “radiative” damping

term is small, the study showed stable modes are excited to amplitudes that are almost as high as unstable mode amplitudes in the ensuing turbulence, indicating that the transfer of energy from the turbulence to the background flow is almost as large as the transfer from the background to the turbulence. Turbulent fluctuations at the relevant spatial scales were shown to be well-approximated by a linear combination of just stable and unstable modes, neglecting tens of thousands of marginally stable modes at those same scales, some of which had even higher amplitudes than the unstable modes. In effect, while the turbulent state at each of these wavenumbers can be viewed as an element of a vector space of very high dimension, it mostly remains in a two-dimensional subspace as far as the flow fluctuations are concerned. This motivated the development of a reduced model in terms of stable and unstable mode amplitudes to describe how turbulent momentum transport scales with the included forcing term in this system. In parameter regimes where stable modes were excited, their inclusion in the transport model was necessary for accurate scaling predictions. In regimes where stable modes were suppressed, their inclusion made little difference to the model's accuracy.⁶

As described in Section 1.1, when a magnetic field is aligned with an

⁶The model was not closed – mode amplitudes were inserted from the simulations. However, this still demonstrates the importance of stable modes in such models.

unstable shear flow, the ensuing turbulent transport is enhanced (Palotti et al. 2008; Mak et al. 2017) despite the KH instability’s growth rate being reduced (Chandrasekhar 1961). This is explored in Chapter 4, where simulations are performed of the KH instability of a shear layer with a flow-aligned magnetic field in MHD using the Dedalus code (Burns et al. 2020). The initial flow profile is similar to the one studied in Chapter 2 but is smooth, varying in the z direction as $\tanh(z)$. The flow is also allowed to evolve freely, with the unstable shear not held fixed and not maintained by any external forcing terms. As unstable modes are excited, they transfer energy from the background flow, transport momentum down the gradient, and broaden the shear layer, thus reducing the shear layer’s propensity to further drive instability. In this way, the saturation of the instability is governed not only by transfer to large-scale stable modes, which is directly observed in simulations using the same methods as in Chapter 3, and the standard transfer to small, dissipative scales, but also by quasilinear flattening. When stable modes are excited, they are directly shown to produce counter-gradient momentum transport that transiently reduces the shear layer’s width whenever they dominate over unstable modes. As the strength of the magnetic field increases, stable modes become less important, and the energy that would transfer back to the

equilibrium is instead transferred to small-scale magnetic fluctuations that enhance turbulent momentum transport and provide resistive dissipation that generally exceeds viscous dissipation. Applying the transport modeling efforts of Chapter 3 to this system yields some success, with the momentum transport due to flow fluctuations described well by stable and unstable modes alone. However, the contribution to momentum transport by the field fluctuations, which dominates in some regimes, is not well-described by these models.

References

- Balbus, S. A., & Hawley, J. F. 1998, *Reviews of Modern Physics*, 70, 1
- Böhm-Vitense, E. 1958, *ZAp*, 46, 108
- Burns, K. J., Vasil, G. M., Oishi, J. S., Lecoanet, D., & Brown, B. P. 2020, *Physical Review Research*, 2, 23068
- Chandrasekhar, S. 1961, *Hydrodynamic and Hydromagnetic Stability* (Oxford University Press)
- Drazin, P. G. 2002, *Introduction to Hydrodynamic Stability* (Cambridge University Press)
- Drazin, P. G., & Reid, W. 1981, *Hydrodynamic Stability* (Cambridge University Press)
- Faganello, M., & Califano, F. 2017, *Journal of Plasma Physics*, 83, 535830601
- Fraser, A. E., Pueschel, M. J., Terry, P. W., & Zweibel, E. G. 2018, *Physics of Plasmas*, 25, 122303
- Fraser, A. E., Terry, P. W., Zweibel, E. G., & Pueschel, M. J. 2017, *Physics of Plasmas*, 24, 062304
- Garaud, P. 2001, *Monthly Notices of the Royal Astronomical Society*, 324, 68
- Hatch, D. R., Terry, P. W., Jenko, F., et al. 2011, *Physics of Plasmas*, 18, 055706
- Heger, A., Langer, N., & Woosley, S. E. 2000, *The Astrophysical Journal*, 528, 368–396
- Hegna, C. C., Terry, P. W., & Faber, B. J. 2018, *Physics of Plasmas*, 25, 022511
- Ho, C., & Huerre, P. 1984, *Annual Review of Fluid Mechanics*, 16, 365
- Hurst, N. C., Danielson, J. R., Dubin, D. H. E., & Surko, C. M. 2020, *Physics of Plasmas*, 27, 042101

- Jenko, F., Dorland, W., Kotschenreuther, M., & Rogers, B. N. 2000, Physics of Plasmas, 7, 1904
- Mak, J., Griffiths, S. D., & Hughes, D. W. 2017, Physical Review Fluids, 2, 113701
- Makwana, K. D., Terry, P. W., Kim, J.-H. H., & Hatch, D. R. 2011, Physics of Plasmas, 18, 012302
- Palotti, M. L., Heitsch, F., Zweibel, E. G., & Huang, Y. 2008, The Astrophysical Journal, 678, 234–244
- Paxton, B., Cantiello, M., Arras, P., et al. 2013, The Astrophysical Journal Supplement Series, 208, 4
- Pueschel, M. J., Faber, B. J., Citrin, J., et al. 2016, Physical Review Letters, 116, 085001
- Qian, T. M., & Mauel, M. E. 2020, Physics of Plasmas, 27, 014501
- Rieger, F. 2019, Galaxies, 7, 78
- Rogers, B. N., & Dorland, W. 2005, Physics of Plasmas, 12, 1
- Terry, P. W., Baver, D. A., & Gupta, S. 2006, Physics of Plasmas, 13, 022307
- Terry, P. W., Baver, D. A., & Hatch, D. R. 2009, Physics of Plasmas, 16, 122305
- Terry, P. W., Faber, B. J., Hegna, C. C., et al. 2018, Physics of Plasmas, 25, 012308
- Terry, P. W., Makwana, K. D., Pueschel, M. J., et al. 2014, Physics of Plasmas, 21, 122303
- Wagner, F. 2007, Plasma Physics and Controlled Fusion, 49, B1
- Whelan, G. G., Pueschel, M. J., & Terry, P. W. 2018, Physical Review Letters, 120, 175002

Chapter 2

Coupling of Damped and Growing Modes in Unstable Shear Flow

*A version of this chapter has previously appeared
in Physics of Plasmas*

Fraser, et al. 2017, Phys. Plasmas, 24, 062304

Abstract

Analysis of the saturation of the Kelvin-Helmholtz (KH) instability is undertaken to determine the extent to which the conjugate linearly stable mode plays a role. For a piecewise-continuous mean flow profile with constant shear in a fixed layer, it is shown that the stable mode is nonlinearly excited, providing an injection-scale sink of the fluctuation energy similar to what has been found for gyroradius-scale drift-wave turbulence. Quantitative evaluation of the contribution of the stable mode to the energy balance at the onset of saturation shows that nonlinear energy transfer to the stable mode is as significant as energy transfer to small scales in balancing energy injected into the spectrum by the instability. The effect of the stable mode on momentum transport is quantified by expressing the Reynolds stress in terms of stable and unstable mode amplitudes at saturation, from which it is found that the stable mode can produce a sizable reduction in the momentum flux.

2.1 Introduction

Shear flows are encountered in a variety of different systems. In the atmosphere, shear-flow instabilities are observed in cloud patterns (Browning 1971). In fusion devices, turbulence generates shearing zonal flows whose potential for instability can significantly impact confinement (Dimits et al. 1996; Rogers et al. 2000). Shear-flow instabilities are especially important in astrophysics. There, differential velocities are produced by a host of processes in a variety of settings, including jets driven by accretion of mass onto compact objects such as protostars or supermassive black holes, intergalactic clouds falling into a galaxy, and galaxies plowing through the intracluster medium. In astrophysical systems, it is thought that shear-flow instabilities induce formation of a turbulent shear layer, resulting in entrainment of material through turbulent momentum transport (Churchwell 1997), thermal and chemical mixing (Kwak et al. 2015), and the possibility of acceleration of particles to high energy (Rieger & Duffy 2006).

Shear-flow instability in a plasma with a uniform magnetic field perpendicular to both the flow and shear directions has the same growth rate as hydrodynamic shear flow with the same profile, illustrating that strong connections exist between hydrodynamic and plasma shear-flow instabilities.

The number of potential applications in both systems makes quantitative models of turbulence driven by sheared flows highly desirable. Analytical models that describe spectral properties are important because both the separation between scales and Reynolds numbers found in astrophysical systems are much larger than what can typically be obtained in converged hydrodynamic and magnetohydrodynamic (MHD) simulations (Palotti et al. 2008; Lecoanet et al. 2016).

Efforts to characterize the nonlinear state of turbulent systems like those mentioned above commonly employ the growth rate and mode structure of the dominant linearly unstable eigenmode, which, after all, drives the turbulence. Examples are mixing-length estimates of transport, which for unstable systems are built on the linear growth rate and an unstable wavenumber, and the quasilinear transport approximation, which uses the cross phase of the unstable eigenmode to approximate the fluctuating correlation responsible for transport. Such approximations are straightforward to construct because they rely on well-understood linear properties of instabilities. However, as unstable systems move into the turbulent regime, there can be no saturation if fluctuations and transport are not modified from the linear state in some essential fashion. The precise nature of such modifications is not well understood. The standard assumption is that the

modifications can be treated as a cascade to smaller scales that eventually become damped, in analogy to externally forced Navier-Stokes turbulence. This type of approach overlooks stable eigenmodes at the same scales as the instability, which invariably exist as other roots of the instability dispersion relation, and may modify the dynamics at the largest scales.

In gyroradius-scale instability-driven turbulence relevant to fusion devices, it has been recognized for more than a decade that stable modes are important in turbulence and should not be neglected (Baver et al. 2002; Hatch et al. 2012). Such modes can be represented as eigenmodes of the linearized system, and occur at the same length scale as the driving instability. Both stable modes, which have a negative linear growth rate (Terry et al. 2006), and subdominant modes, which can have a growth rate that is positive but smaller than that of the most unstable mode (Pueschel et al. 2016), are difficult to detect in initial value simulations. When perturbations are small and only the linear dynamics are considered, these modes are negligible compared to the most unstable mode. However, as the most unstable mode grows in amplitude, nonlinear three-wave interactions between it and the stable modes can pump energy into the latter, causing them to grow and have a significant impact on the turbulence. In collisionless trapped electron mode turbulence, for example, stable modes radically change the dynamics

of the system, including changing the direction of particle flux (Terry et al. 2006; Terry & Gatto 2006). In recent studies of plasma microturbulence in stellarators, quasilinear calculations of energy transport cannot reproduce the results of nonlinear simulations without including every subdominant unstable mode (Pueschel et al. 2016).

While it has been demonstrated that stable modes are universally excited and can have significant impacts on turbulence in the context of gyroradius-scale instabilities in fusion plasmas, their effects have not been studied in global-scale hydrodynamic or MHD instabilities. This paper presents an analysis of a hydrodynamic system with global-scale eigenmodes, demonstrating the nonlinear excitation of stable modes and quantifying their impact on the turbulence using techniques that were successful in plasma microturbulence. An important aspect of this paper is that tools developed in previous analytic calculations for homogeneous systems are extended for analysis of nonlinear excitation in the inhomogeneous environment of unstable shear flows. In previous calculations, the PDEs that describe relevant dynamical quantities were Fourier-transformed to obtain a system of ODEs describing the time-dependence of the Fourier amplitudes. The ODEs were then linearized about an unstable equilibrium to obtain a system of equations of the form $\dot{\mathbf{f}} = \mathcal{D}\mathbf{f}$, where $\mathbf{f}(\mathbf{k}, t)$ is a vector describing the state of the

system at wavenumber \mathbf{k} , and \mathcal{D} is the matrix of linear coupling coefficients. The eigenvectors of \mathcal{D} are the eigenmodes of the system, and their eigenvalues are the frequencies and growth rates. The nonlinear excitation of linearly stable modes was then demonstrated by expanding the nonlinearities of the ODEs in the basis of the linear eigenmodes. With inhomogeneous systems, eigenmodes are not obtained by Fourier-transforming the PDEs and diagonalizing a matrix. Consequently, constructing an invertible transformation between dynamical quantities and linear eigenmodes, and expanding nonlinearities in terms of the eigenmodes, requires appropriate conditioning of the problem.

The paper is organized as follows. In Sec. 2.2 we consider an unstable shear flow and discuss its unstable and stable eigenmodes. In Sec. 2.3 we develop a mapping of the fluctuating flow onto the linear eigenmodes that allows a quantitative description of the energy transfer between the unstable and stable modes. In Sec. 2.4 we use the tools of previous calculations to assess the level to which stable modes are excited relative to unstable modes in saturation. In Sec. 2.5 we consider the impact of stable modes on turbulent momentum transport. Conclusions are presented in Sec. 2.6.

Though we start from equations that describe a two-dimensional, unmagnetized shear flow, this system is identical to a magnetized shear

flow where the equilibrium magnetic field is uniform and in the direction perpendicular to both the flow and the gradient of the flow (Chandrasekhar 1961). Future work will consider the case of a magnetic field in the direction of flow.

2.2 Linear Modes

We investigate a piecewise linear equilibrium flow in the x direction with variation in the z direction within a finite region of width $2d$, referred to as the shear layer. The equilibrium flow is $\mathbf{v}_0 = (U(z), 0, 0)$, where

$$U(z) = \begin{cases} 1 & z \geq 1 \\ z & -1 \leq z \leq 1 \\ -1 & z \leq -1. \end{cases}$$

Here, $U = U^*/U_0$ is the flow normalized to the flow speed U_0 outside the layer, $(x, z) = (x^*/d, z^*/d)$ are coordinates normalized to the layer half-width d , and time will be normalized by $t = t^*U_0/d$.

Constant shear in a shear layer provides the simplest shear-flow instability for which the nonlinear driving of stable modes can be described analytically. The vortex sheet (Chandrasekhar 1961) is an even simpler manifestation of shear-flow instability, but the discontinuous equilibrium flow leads to a discontinuous eigenmode structure. Consequently, the eigenmode

projection of the nonlinearity, which is calculated in the following section and involves a product of derivatives of the eigenmodes [see Eq. (2.10)], is not well-defined.

Here, flow is assumed to be 2D ($\partial/\partial y \equiv 0$), inviscid, and incompressible. It has been shown that for unmagnetized shear flows, 2D perturbations are the most unstable (Drazin & Reid 1981), so it suffices to restrict this analysis to the 2D system. The inviscid assumption simplifies the calculation, although in physical systems at scales much smaller than those considered here, viscosity acts to remove energy from perturbations. The assumption of incompressibility is convenient because of the stabilizing effect of compressibility on shear flow instabilities (Gerwin 1968). These assumptions allow the perturbed velocity to be written in terms of a stream function $\mathbf{v}_1 = \hat{y} \times \nabla\Phi(x, z) = (\partial\Phi/\partial z, 0, -\partial\Phi/\partial x)$. The perturbed vorticity is then entirely in the \hat{y} direction and is governed by the equation (Drazin & Reid 1981),

$$\frac{\partial}{\partial t} \nabla^2 \Phi + U \frac{\partial}{\partial x} \nabla^2 \Phi - \frac{\partial\Phi}{\partial x} \frac{d^2 U}{dz^2} + \frac{\partial\Phi}{\partial z} \frac{\partial}{\partial x} \nabla^2 \Phi - \frac{\partial\Phi}{\partial x} \frac{\partial}{\partial z} \nabla^2 \Phi = 0. \quad (2.1)$$

This equation follows either from vorticity evolution in hydrodynamics or in MHD when the mean field is perpendicular to the flow and the fluctuations are electrostatic. We drop terms nonlinear in Φ and investigate normal modes of the form $\Phi(x, z, t) = \phi(k, z) \exp[ikx + i\omega(k)t]$, where $k = k^*d$ and

$\omega = \omega^* d/U_0$. If we find that $\text{Im}(\omega(k)) < 0$ for some mode at wavenumber k , then the mode is unstable and grows exponentially in time. If $\text{Im}(\omega(k)) > 0$, the mode is stable and decays exponentially. If $\text{Im}(\omega(k)) = 0$, the mode is marginally stable. We take Fourier modes in x because Eq. (2.1) is homogeneous in x , but the dependence of U on z implies that Fourier modes in z are not solutions to the linear equation. This significantly complicates the analysis of stable mode interactions, as discussed in the following section.

The linearized equation for the normal modes is (Drazin & Howard 1962)

$$(\omega + kU) \left(\frac{d^2}{dz^2} - k^2 \right) \phi - k\phi \frac{d^2U}{dz^2} = 0. \quad (2.2)$$

Solutions of this system are well known (Chandrasekhar 1961), but usually only the growth rate of the unstable mode and its eigenfunction are considered. We reexamine the problem to keep track of both the unstable and stable modes, in order to investigate their interaction through the nonlinearities in Eq. (2.1).

Note that for the shear layer, d^2U/dz^2 is singular at $z = \pm 1$. For $|z| \neq 1$ however, $d^2U/dz^2 = 0$, so

$$(\omega + kU) \left(\frac{d^2}{dz^2} - k^2 \right) \phi = 0$$

(for $|z| \neq 1$). Solutions are given by either $\omega + kU = 0$ or $(d^2/dz^2 - k^2)\phi = 0$. While modes that satisfy the former are solutions of the system, we are

interested in stable and unstable modes, which require $\text{Im}(\omega) \neq 0$. Therefore we construct eigenmodes from $(d^2/dz^2 - k^2)\phi = 0$. It has been shown that for shear flow instabilities, the initial value calculation admits additional modes that decay algebraically (Case 1960). While these modes potentially play a role in saturation of the instability and should be considered eventually, it makes sense to focus first on the interaction between the exponentially growing and decaying modes. Both the exponentially and algebraically decaying modes are ignored in quasilinear models of turbulence, so to show that these models overlook important, driving-scale features of the system it suffices to demonstrate the importance of stable modes.

Focusing on solutions of $(d^2/dz^2 - k^2)\phi = 0$, modes are given by

$$\phi(z) = \begin{cases} ae^{-|k|z} & z > 1 \\ e^{|k|z} + be^{-|k|z} & -1 < z < 1 \\ ce^{|k|z} & z < -1, \end{cases} \quad (2.3)$$

with the constants a , b , and c to be determined.

The flow profile $U(z)$ is continuous at the boundaries of the shear layer, which we assume to be fixed at $z = \pm 1$. Therefore ϕ must be continuous (Chandrasekhar 1961), so a and c can each be written in terms of b . Although $U(z)$ and ϕ are continuous at $z = \pm 1$, the discontinuities in dU/dz lead to discontinuities in $d\phi/dz$. The jump conditions that determine

these discontinuities are obtained by integrating Eq. (2.2) from $-1 - \epsilon$ to $-1 + \epsilon$ and from $1 - \epsilon$ to $1 + \epsilon$, then taking $\epsilon \rightarrow 0$:

$$\lim_{\epsilon \rightarrow 0} (\omega \pm k) \frac{d\phi}{dz} \Big|_{\pm 1-\epsilon}^{\pm 1+\epsilon} \pm k\phi(\pm 1) = 0. \quad (2.4)$$

After inserting Eq. (2.3), these form two constraints on b in terms of $\omega(k)$, which can be solved to obtain the dispersion relation,

$$\omega = \pm \frac{e^{-2|k|}}{2} \sqrt{e^{4|k|}(1 - 2|k|)^2 - 1}. \quad (2.5)$$

Figure 2.1 shows how the growth rates and frequencies depend on wavenumber. Note that $\omega^2 < 0$ for $0 < |k| < k_c$, where $k_c \approx 0.64$. For $k > k_c$, we shall refer to the negative and positive branches of ω as ω_1 and ω_2 respectively,

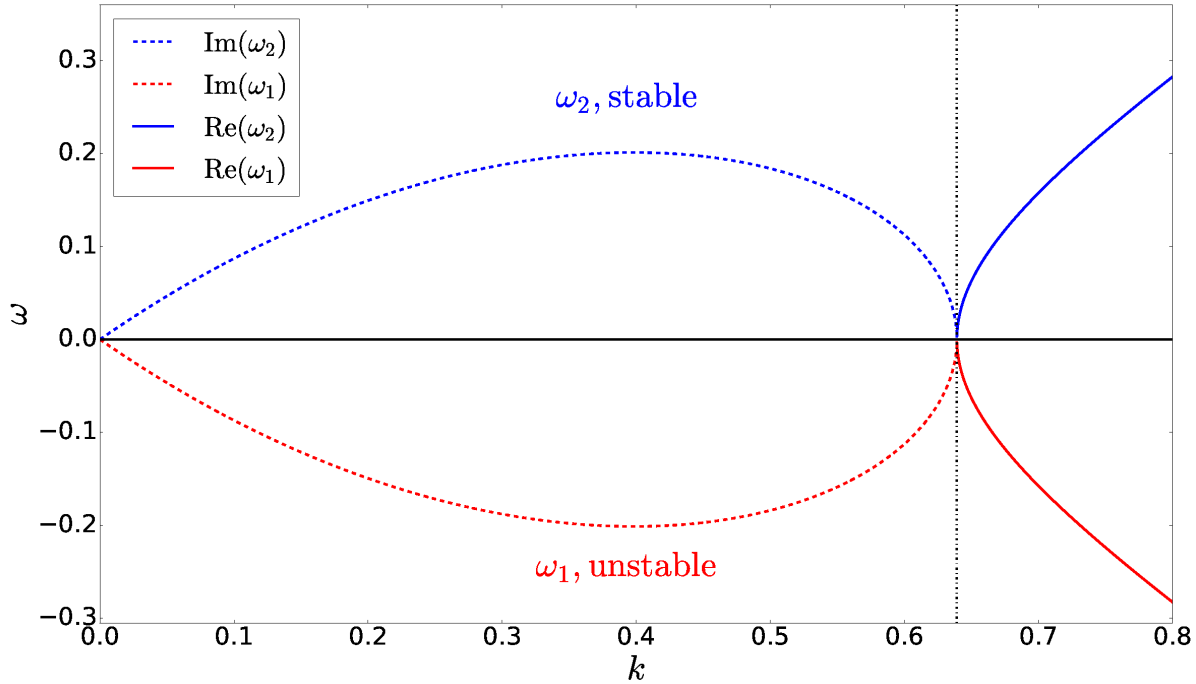


Figure 2.1 Growth rate $\text{Im}(\omega)$ and frequency $\text{Re}(\omega)$ of the two modes for the inviscid shear layer. For $|k| \lesssim 0.64$ one mode is unstable and the other is stable, while for $|k| \gtrsim 0.64$ both modes are marginally stable.

noting that the reality condition requires $\omega_j(-k) = \omega_j^*(k)$. For $|k| < k_c$, we choose ω_1 to be the unstable root and ω_2 the stable one. Because b depends on ω through Eq. (2.4) and the eigenmode structure $\phi(z)$ depends on b through Eq. (2.3), the two solutions ω_j correspond to two different eigenmodes $\phi_j(z)$. We identify b_j and ϕ_j as the b and ϕ corresponding to ω_j . The eigenmodes are then

$$\phi_j(k, z) = \begin{cases} (e^{2|k|} + b_j) e^{-|k|z} & z > 1 \\ e^{|k|z} + b_j e^{-|k|z} & -1 < z < 1 \\ (1 + b_j e^{2|k|}) e^{|k|z} & z < -1, \end{cases} \quad (2.6)$$

where

$$b_j = e^{2|k|} \frac{2|k|(\omega_j + k) - k}{k} \quad (2.7)$$

satisfies $b_1(k) = b_2(-k) = b_2^*(k)$ for $|k| < k_c$, and $b_j(k) = b_j(-k) = b_j^*(k)$ for $|k| > k_c$. For $\omega^2 < 0$, the eigenmodes are nearly identical but satisfy $\phi_1(k, z) = \phi_2^*(k, z)$. Figure 2.2 shows the flows corresponding to these eigenmodes for four wavenumbers sampling the unstable and stable ranges. Previous work has shown that the physical mechanisms for instability of ϕ_1 and stability of ϕ_2 can be understood in terms of resonant vorticity waves in both the hydrodynamic (Baines & Mitsuderaf 1994) and MHD (Heifetz et al. 2015) systems.

In standard descriptions of turbulence and quasilinear transport calculations, it is common practice to neglect stable modes given their exponential decay from a small initial value. In this paper we account for the nonlinear drive of the stable mode by the unstable mode and investigate its impact on the evolution of the system.

2.3 Eigenmode Projection

In previous calculations of stable mode excitation (Terry et al. 2006; Makwana et al. 2011), fluctuations from equilibrium were represented by

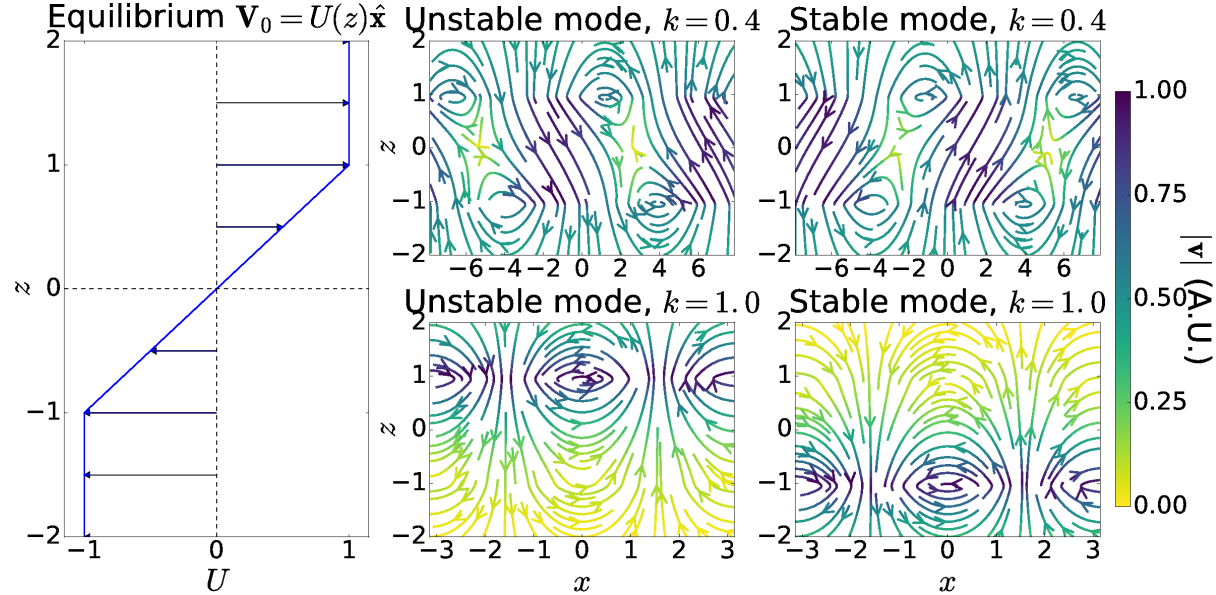


Figure 2.2 Equilibrium (left column) compared with velocity profiles of the unstable ϕ_1 (middle column) and the stable ϕ_2 (right column) at wavenumbers $k = 0.4$ (top row) and $k = 1$ (bottom row) plotted over one wavelength in x and from $z = -2$ to $z = 2$. Streamlines are plotted with color indicating flow speed. The first row is in the unstable range, where ϕ_1 grows exponentially while ϕ_2 decays exponentially. The second row is a marginally stable wavenumber, where both ϕ_1 and ϕ_2 oscillate without any growth [see Fig. 2.1].

a vector $\mathbf{f}(\mathbf{k}, t)$ whose components were the Fourier-transformed dynamical quantities. Because the systems were homogeneous, the linearized, Fourier-transformed PDEs became ODEs of the form $\dot{\mathbf{f}} = \mathcal{D}\mathbf{f}$ with the dynamics at each wavenumber \mathbf{k} linearly decoupled. Thus, the eigenmodes of the system were the eigenvectors \mathbf{f}_j of the $N \times N$ matrix \mathcal{D} , and arbitrary states could be expanded as linear combinations of the eigenvectors:

$$\mathbf{f}(\mathbf{k}, t) = \sum_{j=1}^N \beta_j(\mathbf{k}, t) \mathbf{f}_j(\mathbf{k}, t), \quad (2.8)$$

where $\beta_j(\mathbf{k}, t)$ is the component of \mathbf{f} in the eigenmode basis. Also called eigenmode amplitudes, the functions β_j are not specified by the solutions of the linearized equations except through an initial condition. Under linear evolution the stable modes subsequently decrease to insignificance. However, the full nonlinear ODEs can readily be written in terms of the eigenmodes by substituting the eigenmodes for the dynamical quantities using Eq. (2.8). From there, separate equations for each $\dot{\beta}_j$ can be derived. These equations for $\dot{\beta}_j$ are equivalent to the original PDEs, but they describe the nonlinear evolution of the system in terms of the eigenmode amplitudes. We refer to this process, both the expansion of the perturbations and the manipulation of their governing equations, as an eigenmode decomposition. The equations for $\dot{\beta}_j$ provide powerful insight into the system. The nonlinearities that couple the dynamical fields at different scales become nonlinearities that

couple eigenmodes at different wavelengths. Thus, it was shown (and borne out by many simulations, see e.g. Terry et al. 2006; Makwana et al. 2011) that despite decaying in the linear regime, the stable modes are nonlinearly driven by the unstable modes.

In these previous calculations, the homogeneous nature of the system made the set of linear eigenmodes a complete basis: at every time t and wavevector \mathbf{k} , the state vector \mathbf{f} could be expanded in a basis of the eigenmodes [i.e. Eq. (2.8)]. Due to the inhomogeneity of the present system, the linear solutions are not simply Fourier modes in z , so this system does not readily lend itself to the vector representation of Terry et al. (2006). Moreover, Eq. (2.1) admits only two eigenmodes which are expected not to span arbitrary perturbations that satisfy the boundary conditions (Case 1960). So the true state of the system cannot be written exactly in the form of Eq. (2.8) with $N = 2$. In order to properly describe the evolution of the system given an arbitrary initial condition, the system could be expanded in appropriate orthogonal polynomials or investigated as an initial value problem with additional time-dependent basis functions that are linear solutions of the problem. Previous work has demonstrated that for inviscid shear flows, the initial value calculation leads to the “discrete” eigenmodes with time-dependence $\exp[i\omega t]$ described in the previous section,

and an additional set of “continuum” modes (Case 1960). These continuum modes either oscillate with frequency k or decay algebraically. For the present calculation we only consider perturbations that can be expressed as linear combinations of the two discrete eigenmodes ϕ_1 and ϕ_2 , representing a truncation of the complete system. If we are able to demonstrate a significant impact from ϕ_2 , that suffices to demonstrate the importance of stable modes, relative to existing models that only consider the unstable mode.

By focusing on perturbations that are linear combinations of ϕ_1 and ϕ_2 (i.e. limiting ourselves to the subspace spanned by ϕ_1 and ϕ_2), the vector representation and invertible linear transformation between the state of the system and the eigenmode amplitudes of Terry et al. (2006) can be recovered. Consequently, the governing Eq. (2.1) can be manipulated to derive nonlinear equations that describe the evolution of the eigenmode amplitudes and their interactions. The method relies on the jump conditions given in Eq. (2.4). Since the jump conditions for one eigenmode differ from those for the other eigenmode, one can form an invertible map between the discontinuity of $d\phi/dz$ at each interface and the amplitude of each eigenmode. Additionally, because there are two jump conditions that will serve as our dynamical quantities, only the two eigenmodes of the previous

section are needed to construct an invertible map between eigenmodes and dynamical quantities. To derive equations describing the nonlinear interaction between the eigenmodes, we start by deriving nonlinear jump conditions.

First, let $\hat{\phi}(k, z, t) = \mathcal{F}[\Phi(x, z, t)]$ be the Fourier transformed stream function, and assume

$$\hat{\phi}(k, z, t) = \beta_1(k, t)\phi_1(k, z) + \beta_2(k, t)\phi_2(k, z). \quad (2.9)$$

The nonlinear jump conditions are obtained by performing the same steps that led to Eq. (2.4) without dropping nonlinear terms (and explicitly taking the Fourier transform rather than assuming normal modes). Taking the Fourier transform and integrating from $\pm 1 - \epsilon$ to $\pm 1 + \epsilon$ with $\epsilon \rightarrow 0$ yields

$$\frac{\partial}{\partial t} \hat{\Delta}_\pm \pm ik\hat{\Delta}_\pm \pm ik\hat{\phi}(k, \pm 1) + \lim_{\epsilon \rightarrow 0} ik \int_{-\infty}^{\infty} \frac{dk'}{2\pi} \left[\frac{d}{dz} \hat{\phi}(k', z) \frac{d}{dz} \hat{\phi}(k'', z) \right]_{\pm 1-\epsilon}^{\pm 1+\epsilon} = 0, \quad (2.10)$$

where $k'' \equiv k - k'$, while

$$\begin{aligned} \hat{\Delta}_\pm(k, t) &\equiv \lim_{\epsilon \rightarrow 0} \left[\frac{d}{dz} \hat{\phi}(k, \pm 1 + \epsilon, t) - \frac{d}{dz} \hat{\phi}(k, \pm 1 - \epsilon, t) \right] \\ &= \beta_1(k, t)\Delta_{\pm 1}(k) + \beta_2(k, t)\Delta_{\pm 2}(k) \end{aligned}$$

and

$$\Delta_{\pm j}(k) \equiv \lim_{\epsilon \rightarrow 0} \left[\frac{d}{dz} \phi_j(k, \pm 1 + \epsilon) - \frac{d}{dz} \phi_j(k, \pm 1 - \epsilon) \right]$$

are the discontinuities in $d\hat{\phi}/dz$ and $d\phi_j/dz$ at $z = \pm 1$. With $\hat{\phi}$ given by Eq. (2.9) and ϕ_j given by Eq. (2.6), one can show that

$$\phi_j(k, 1) = \frac{-\Delta_{+j}}{2|k|} - \frac{\Delta_{-j}}{2|k|e^{2|k|}},$$

and

$$\phi_j(k, -1) = \frac{-\Delta_{+j}}{2|k|e^{2|k|}} - \frac{\Delta_{-j}}{2|k|}.$$

The $\hat{\phi}(k, \pm 1)$ term in Eq. (2.10) can then be written in terms of $\hat{\Delta}_\pm$ to yield

$$\frac{\partial}{\partial t} \begin{pmatrix} \hat{\Delta}_+ \\ \hat{\Delta}_- \end{pmatrix} = \mathcal{D} \begin{pmatrix} \hat{\Delta}_+ \\ \hat{\Delta}_- \end{pmatrix} + \begin{pmatrix} N_+ \\ N_- \end{pmatrix}, \quad (2.11)$$

with

$$\mathcal{D} = ik \begin{pmatrix} \frac{1}{2|k|} - 1 & \frac{e^{-2|k|}}{2|k|} \\ \frac{-e^{-2|k|}}{2|k|} & -\frac{1}{2|k|} + 1 \end{pmatrix}, \quad (2.12)$$

and N_\pm representing the nonlinearities in Eq. (2.10). Note that taking $N_\pm \rightarrow 0$ and $\partial/\partial t \rightarrow i\omega$ reduces this to the linear system solved in the previous section.

We now have all of the necessary tools to treat this system in a manner similar to the previously-mentioned calculations (Terry et al. 2006; Makwana et al. 2011). Using our definitions for $\hat{\Delta}_\pm$ and $\Delta_{\pm j}$, the z -derivative of Eq. (2.9) evaluated between $z = \pm 1 + \epsilon$ and $z = \pm 1 - \epsilon$ with $\epsilon \rightarrow 0$ is

$$\begin{pmatrix} \hat{\Delta}_+ \\ \hat{\Delta}_- \end{pmatrix} = \mathbf{M} \begin{pmatrix} \beta_1 \\ \beta_2 \end{pmatrix}, \quad (2.13)$$

where

$$\mathbf{M} = \begin{pmatrix} \Delta_{+1} & \Delta_{+2} \\ \Delta_{-1} & \Delta_{-2} \end{pmatrix} = -2|k|e^{|k|} \begin{pmatrix} 1 & 1 \\ b_1 & b_2 \end{pmatrix}, \quad (2.14)$$

and b_j is given in Eqn. (2.7). Equation (2.13) is equivalent to Eq. (2.8): for this calculation, the dynamical quantities that we use to specify the state of the system are $\hat{\Delta}_\pm$, and their eigenmode structure is given by the columns of the matrix \mathbf{M} . The governing nonlinear PDE, Eq. (2.1) has been rewritten as a system of nonlinear ODEs, Eq. (2.11). The linearized system of ODEs (Eq. (2.11) with $N_\pm \rightarrow 0$) can be diagonalized: substituting $\hat{\Delta}_\pm$ for β_j via Eq. (2.13) and multiplying by \mathbf{M}^{-1} on the left gives

$$\begin{pmatrix} \dot{\beta}_1 \\ \dot{\beta}_2 \end{pmatrix} = \mathbf{M}^{-1}\mathcal{D}\mathbf{M} \begin{pmatrix} \beta_1 \\ \beta_2 \end{pmatrix}, \quad (2.15)$$

where the matrix $\mathbf{M}^{-1}\mathcal{D}\mathbf{M}$ is diagonal with entries $i\omega_j$.

The nonlinear interactions between the eigenmodes can now be investigated. Applying the steps that led to Eq. (2.15) to the full, nonlinear Eq. (2.11) yields

$$\begin{pmatrix} \dot{\beta}_1 \\ \dot{\beta}_2 \end{pmatrix} = \mathbf{M}^{-1}\mathcal{D}\mathbf{M} \begin{pmatrix} \beta_1 \\ \beta_2 \end{pmatrix} + \mathbf{M}^{-1} \begin{pmatrix} N_+ \\ N_- \end{pmatrix}, \quad (2.16)$$

where, again, N_\pm are the nonlinearities in Eq. (2.10). Using Eq. (2.9) and the forms for ϕ_j given by Eq. (2.6), N_\pm can be written in terms of products of the form $\beta_i\beta_j$ with i, j each taking values 1, 2. Equation (2.16) then

becomes

$$\begin{aligned}\dot{\beta}_1(k) &= i\omega_1(k)\beta_1(k) \\ &+ \int_{-\infty}^{\infty} \frac{dk'}{2\pi} \left[C_1(k, k')\beta_1(k')\beta_1(k'') + C_2(k, k')\beta_1(k')\beta_2(k'') \right. \\ &\quad \left. + C_3(k, k')\beta_1(k'')\beta_2(k') + C_4(k, k')\beta_2(k')\beta_2(k'') \right],\end{aligned}\tag{2.17}$$

$$\begin{aligned}\dot{\beta}_2(k) &= i\omega_2(k)\beta_2(k) \\ &+ \int_{-\infty}^{\infty} \frac{dk'}{2\pi} \left[D_1(k, k')\beta_1(k')\beta_1(k'') + D_2(k, k')\beta_1(k')\beta_2(k'') \right. \\ &\quad \left. + D_3(k, k')\beta_1(k'')\beta_2(k') + D_4(k, k')\beta_2(k')\beta_2(k'') \right].\end{aligned}\tag{2.18}$$

The coefficients C_j, D_j arise from writing the nonlinearities N_{\pm} in the basis of the linear eigenmodes, so their functional forms include information about both the linear properties of the system and the nonlinearities N_{\pm} . The exact expressions for C_j, D_j are given in the Appendix, where it is shown that $C_2(k, k') = C_3(k, k - k')$, so that the C_3 integral is equal to the C_2 integral. Equations (2.17) and (2.18) are equivalent to Eq. (2.11), but they directly show how β_1 and β_2 interact.

An analogy can be made here to the use of Elsässer variables in incompressible, homogeneous MHD turbulence, which are a familiar example of an eigenmode decomposition that makes explicit the nonlinear interaction of the linear eigenmodes. The linearized equations have as solutions

counterpropagating, noninteracting waves of the form $\mathbf{z}^\pm = \mathbf{v} \pm \mathbf{b}/(4\pi\rho_0)^{1/2}$. Expressing the nonlinear equations in terms of \mathbf{z}^\pm , the nonlinearity in the equation for $\partial\mathbf{z}^\pm/\partial t$ is $\mathbf{z}^\mp \cdot \nabla \mathbf{z}^\pm$, which describes the nonlinear interactions between linearly noninteracting modes. In the present calculation, the linearly noninteracting ϕ_1, ϕ_2 are comparable to \mathbf{z}^\pm , and the terms proportional to $\beta_1(k')\beta_2(k'')$ and $\beta_1(k'')\beta_2(k')$ are comparable to $\mathbf{z}^\mp \cdot \nabla \mathbf{z}^\pm$. However, unlike the \mathbf{z}^\pm equations, the $\dot{\beta}_j$ equations include other nonlinear terms that are proportional to $\beta_1(k')\beta_1(k'')$ and $\beta_2(k')\beta_2(k'')$. If all of the nonlinearities are zero except for the C_1 term, then the evolution of $\beta_1(k)$ is just a combination of its linear drive $i\omega_1(k)$ and three-wave interactions with $\beta_1(k')$ and $\beta_1(k - k')$, allowing ϕ_1 to saturate through a Kolmogorov-like cascade to smaller scales. This is effectively the assumption of standard quasilinear calculations of momentum transport, where only ϕ_1, ω_1 are considered. Figure 2.3 shows some of the nonlinear coupling coefficients plotted over a range of wavenumbers. Since D_1, C_2 , and C_3 are not identically zero, there is some interaction between the eigenmodes. Systems where such interactions have been identified are all gyroradius-scale, quasihomogeneous systems driven by drift-wave instabilities (Terry et al. 2006; Makwana et al. 2011). Equations (2.17) and (2.18) represent a demonstration that these interactions occur for larger-scale, inhomogeneous plasmas and neutral fluids.

2.4 The Threshold Parameter

By comparing the nonlinearities that transfer energy to stable modes with those that cause the Kolmogorov-like cascade of energy to small scales, one can investigate how important stable modes are in instability saturation. A quantity known as the threshold parameter P_t has been used to evaluate the relative importance of the stable eigenmodes in situations where instability saturation is described by eigenmode-projected ODEs. The threshold parameter P_t estimates the relative importance in saturation of the nonlinearities responsible for energy transfer to the stable mode versus the nonlinearity of the forward cascade (Terry et al. 2006). If P_t is small compared to unity, it indicates that the instability saturates via a Kolmogorov-like transfer of energy to smaller scales, and only the term

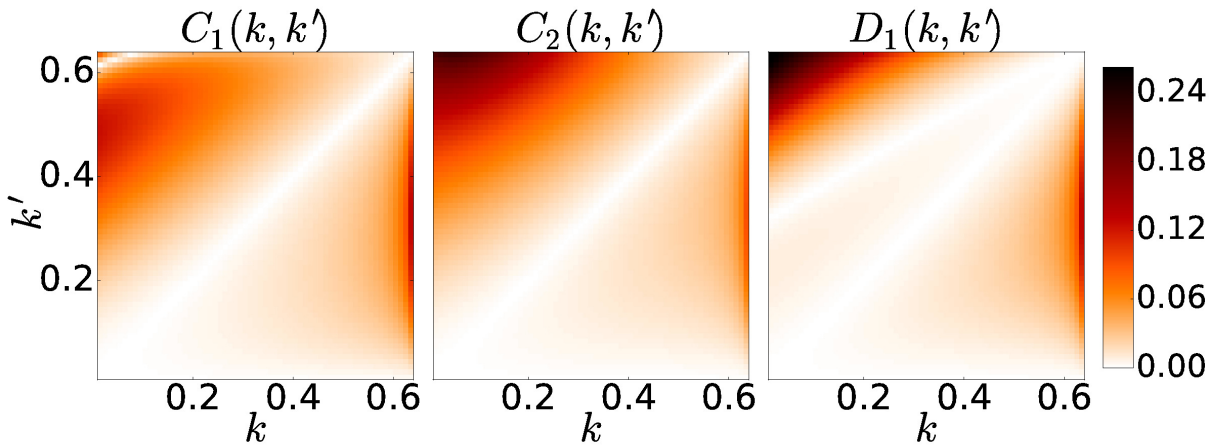


Figure 2.3 Three of the eight nonlinear coupling coefficients in Eqs. (2.17) and (2.18), C_1 , C_2 , and D_1 , evaluated over the most relevant scales. Color indicates absolute values of the coefficients. The coefficients are all roughly the same magnitude, indicating significant coupling between stable and unstable eigenmodes.

in Eq. (2.8) corresponding to the most unstable eigenmode needs to be included to accurately describe the system. If $P_t \gtrsim 0.3$, it was found that the transfer of energy from the unstable mode to other modes at similar scales is an important mechanism in saturation. In that case, additional terms in Eq. (2.8) must therefore be included (Makwana et al. 2011).

The quantity P_t is the ratio of the $C_1\beta_1\beta_2$ and $C_2\beta_1\beta_1$ terms in Eq. (2.17) and therefore includes information about both linear and nonlinear properties of the system. In previous work (Terry et al. 2006; Makwana et al. 2011), simplifying assumptions – such as treating growth rates $\gamma_j = -\text{Im}(\omega_j)$ as independent of wavenumber – allowed the threshold parameter to be written as

$$P_t = \frac{2D_1C_2}{C_1^2(2 - \gamma_2/\gamma_1)} \quad (2.19)$$

for $\gamma_2 < 0$. This form of P_t is useful because it illustrates how P_t depends on different parameters of the system: the size of P_t relative to unity is determined by the ratios D_1C_2/C_1^2 and γ_1/γ_2 . When the former is small, stable modes are only weakly coupled to unstable modes and have little impact on saturation dynamics. When the latter is small, stable modes decay too quickly to achieve significant amplitude by the time the instability saturates unless $D_1C_2/C_1^2 \gg 1$ and compensates. Previous work evaluated this form of P_t in several systems and found that whenever P_t is at least

a few tenths, energy transfer to stable modes becomes comparable to the energy injection rate of the instability (Makwana et al. 2011). Note that in the system considered here $|\gamma_1/\gamma_2| = 1$, and numerically evaluating C_j, D_j shows that D_1 and C_2 are of the same order as or even larger than C_1 [see Fig. 2.3]. These features alone yield $P_t \approx 0.7$, which implies stable modes are important for KH saturation.

Here we extend previous analyses of P_t by including the full wavenumber dependence of γ_j, C_j , and D_j . Consider the evolution of the system from a small initial amplitude β_i . When amplitudes are small every nonlinear term is negligible, so the dynamics are linear with β_2 decaying and β_1 growing exponentially at every wavenumber. Eventually couplings in $\int(dk'/2\pi)D_1(k, k')\beta_1(k')\beta_1(k - k')$ dominate in Eq. (2.18). This occurs in the linear phase, before saturation, because nonlinearities dominate the decaying linear response of β_2 long before matching the growing linear response of β_1 . Thus, Eq. (2.18) can be approximated as

$$\dot{\beta}_2(k) = i\omega_2(k)\beta_2(k) + \int_{-\infty}^{\infty} \frac{dk'}{2\pi} D_1(k, k')\beta_1(k')\beta_1(k''). \quad (2.20)$$

Note that for these times $\beta_2 \ll \beta_1$ therefore the D_1 terms are the largest of the D_j terms. Since the C_j nonlinearities have not reached the amplitudes of the growing linear terms, β_1 can be approximated as $\beta_i \exp[i\omega_1 t]$. These approximations are referred to as the parametric instability approximations

(Terry et al. 2006). Then Eq. (2.20) is solved by

$$\begin{aligned} \beta_2(k, t) = & \\ & \int_{-\infty}^{\infty} \frac{dk'}{2\pi} \frac{D_1(k, k') \beta_i^2}{i(-\omega_2(k) + \omega_1(k') + \omega_1(k - k'))} \left[e^{i(\omega_1(k') + \omega_1(k - k'))t} - e^{i\omega_2(k)t} \right] \\ & + \beta_i e^{i\omega_2(k)t}. \quad (2.21) \end{aligned}$$

In assessing P_t the above integral is only taken over unstable wavenumbers, as they drive β_2 more strongly than marginally stable modes.

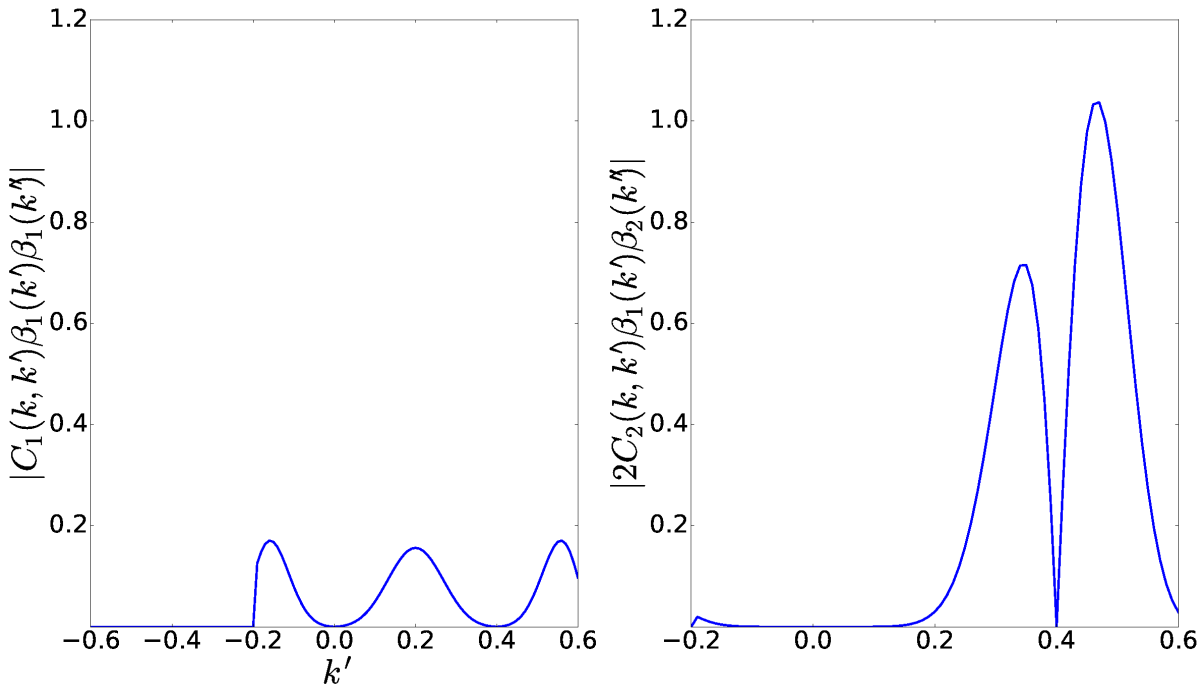


Figure 2.4 Nonlinear terms in Eq. (2.17) at saturation for $k = 0.4$ and $\beta_i = 0.01$, with k' and $k - k'$ ranging from -0.6 to 0.6 . The C_1 term is responsible for the Kolmogorov-like saturation of the instability by energy transfer to unstable modes at smaller wavelengths. The C_2 term represents the previously-neglected coupling between unstable modes at k and k' with stable modes at k'' . The threshold parameter is evaluated by dividing the peak value of the C_2 term by the peak value of the C_1 term. Here we find $P_t \approx 6$, indicating that stable modes are important in KH saturation.

To evaluate P_t , the ratio of the largest $\beta_1\beta_2$ term and the largest $\beta_1\beta_1$ term in Eq. (2.17) is taken at the time of saturation t_s :

$$P_t = \left[\frac{\max |2C_2\beta_1(k')\beta_2(k'')|}{\max |C_1\beta_1(k')\beta_1(k'')|} \right]_{t=t_s}, \quad (2.22)$$

where t_s is defined as the time at which one of the nonlinearities in Eq. (2.17) reaches the same amplitude as the linear term. Figure 2.4 shows the size of these terms at saturation for $k = 0.4$ with an initial amplitude of $\beta_i = 0.01$. We choose $k = 0.4$ because it is the most unstable wavenumber and is therefore the wavenumber of the most dominant unstable mode leading into saturation. From Fig. 2.4, it is inferred that $P_t \approx 6$, indicating that even before the nominal saturation time energy transfer to stable modes has become as important to the saturation of the unstable mode at $k = 0.4$ as the Kolmogorov-like transfer to unstable modes at other scales.

In previous calculations of P_t , the parameter was independent of the initial amplitude β_i (which is assumed to be the same for each k). However, in the above evaluation of P_t , we do find that it depends on β_i ; for instance, reducing β_i to 0.001 yields $P_t \approx 15$. In previous calculations, the lack of dependence of P_t on β_i is an artifact of treating growth rates as independent of wavenumber (Terry et al. 2006). In considering Eq. (2.17) for the most unstable wavenumber, both $\beta_1(k')$ and $\beta_1(k'')$ were assumed to grow at the same rate as the most unstable mode, when in fact three-wave interactions

require $k \neq k'$. When including wavenumber dependence, these nonlinear terms will necessarily grow at less than twice the peak growth rate. On the other hand, stable modes near $k = 0$ can be driven by $D_1\beta_1\beta_1$ terms where one of the driving modes is near $k = 0.4$ and the other is near $k = -0.4$. Thus, our inclusion of the wavenumber dependence of ω_j causes β_2 to grow large enough that Eq. (2.20) becomes invalid before saturation time. This makes the precise value of P_t less meaningful, as the stable modes have grown so large that the approximations made in obtaining P_t are invalid. However, the size of β_2 relative to β_1 and the comparable amplitudes of C_2 and C_1 imply $P_t \gtrsim 1$, and therefore $P_t \gtrsim 0.3$ is still well satisfied.

The above nonlinear analysis demonstrates that energy transfer to stable modes is significant relative to energy transfer to smaller scales, modifying the usual understanding of instability saturation by a cascade to small scales. The analysis employs approximations, hence it is instructive to consider a second, complementary form of approximate nonlinear analysis based on a three-wavenumber truncation of Eqs. (2.17) and (2.18). Such a calculation complements the P_t analysis because it makes different assumptions. The P_t analysis makes parametric instability approximations when considering the evolution of β_2 (c.f. Eq. (2.21)), but samples a broad continuum of wavenumbers. On the other hand, a three-wavenumber truncation makes

no assumptions about the evolution of the modes, and instead limits the system to only three wavenumbers that are evolved according to Eqs. (2.17) and (2.18).

The result of a three-wavenumber truncation is plotted in Fig. 2.5, showing the time evolution of $\beta_j(k, t)$ obtained by solving Eqs. (2.17) and (2.18) numerically with only interactions between $k = 0.3$, $k' = 0.9$, and $k - k' = -0.6$ considered. The linear growth phase of β_1 is clearly seen, as is the linear decay and nonlinear driving of β_2 . The linear growth phase for β_1 ends with both eigenmodes reaching comparable amplitudes,

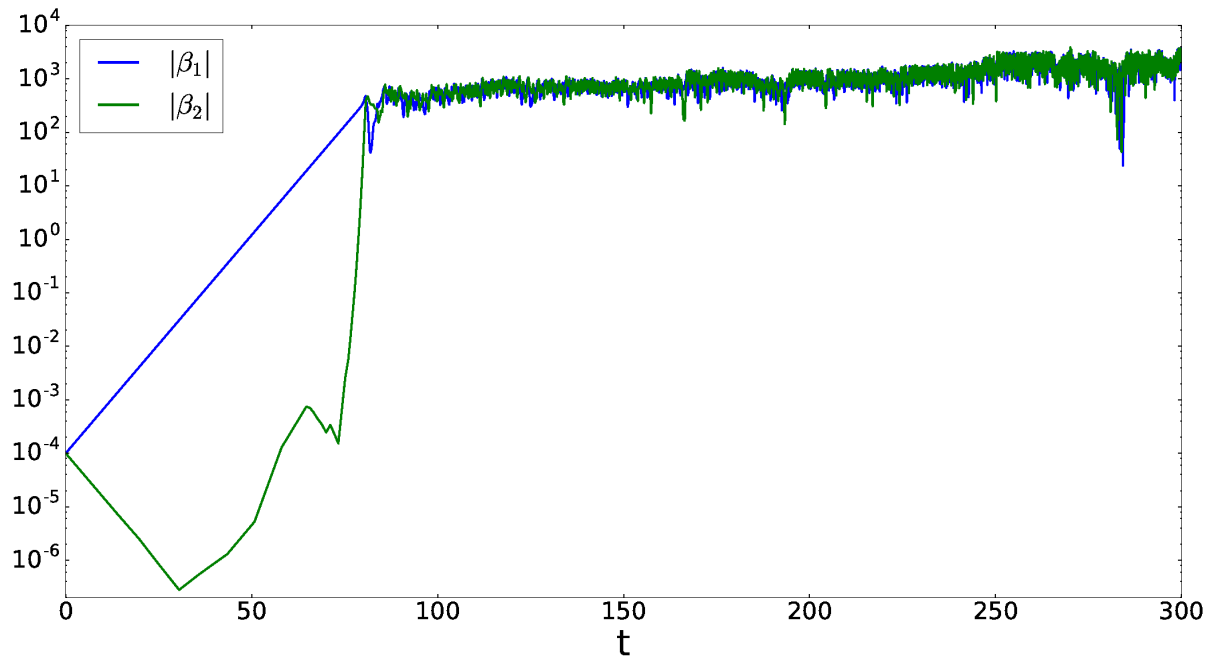


Figure 2.5 Time evolution of $|\beta_j(k, t)|$ for a three-wavenumber truncation with $k = 0.3$, $k' = 0.9$, and $k - k' = -0.6$. As expected from the P_t analysis, the stable mode decays linearly, then is nonlinearly pumped to an amplitude that is comparable to the unstable mode.

consistent with the P_t analysis. Once the stable mode reaches a value that is comparable to the unstable mode there is continuous exchange of energy between the two modes. The saturation levels slowly grow as $t \rightarrow \infty$. That can be understood as a consequence of the inviscid dynamics in a three-mode system, in that previous work has demonstrated that a necessary condition for bounded solutions to three-mode truncations is that the sum of the growth rates is negative (Terry & Horton 1982). Without viscosity, the present system does not meet the necessary condition. Note that the time scale for nonlinear energy exchange is very short compared to the time scale of the saturation level increase, strongly suggesting that the nonlinearities of Eqs. (2.17) and (2.18) conserve energy. This calculation demonstrates that the system can saturate by energy transfer to stable modes, and shows that the assumptions made regarding the growth of β_1 and β_2 in the P_t analysis are reasonable.

As an illustration of the effect of finite β_2 on the fluctuating flow, Fig. 2.6 shows the flows arising from linear combinations of β_1 and β_2 with the weight of β_2 varied. The flow arising purely from the unstable mode is strikingly different from the flow that combines β_1 and β_2 with equal weights. Regions of hyperbolic flow appear to be less likely for the equally weighted combination, suggesting that secondary structure generation and

cascading may be weakened when the stable mode is excited. This will be the subject of future research.

2.5 Momentum Transport

Reynolds stresses and the associated momentum transport due to unstable modes tend to broaden the original flow profile. Here we show that stable modes have the potential to reduce the broadening of the profile. The transport of momentum in the x direction across the interface at $z = 1$ is found by integrating the x -component of the divergence of the stress tensor

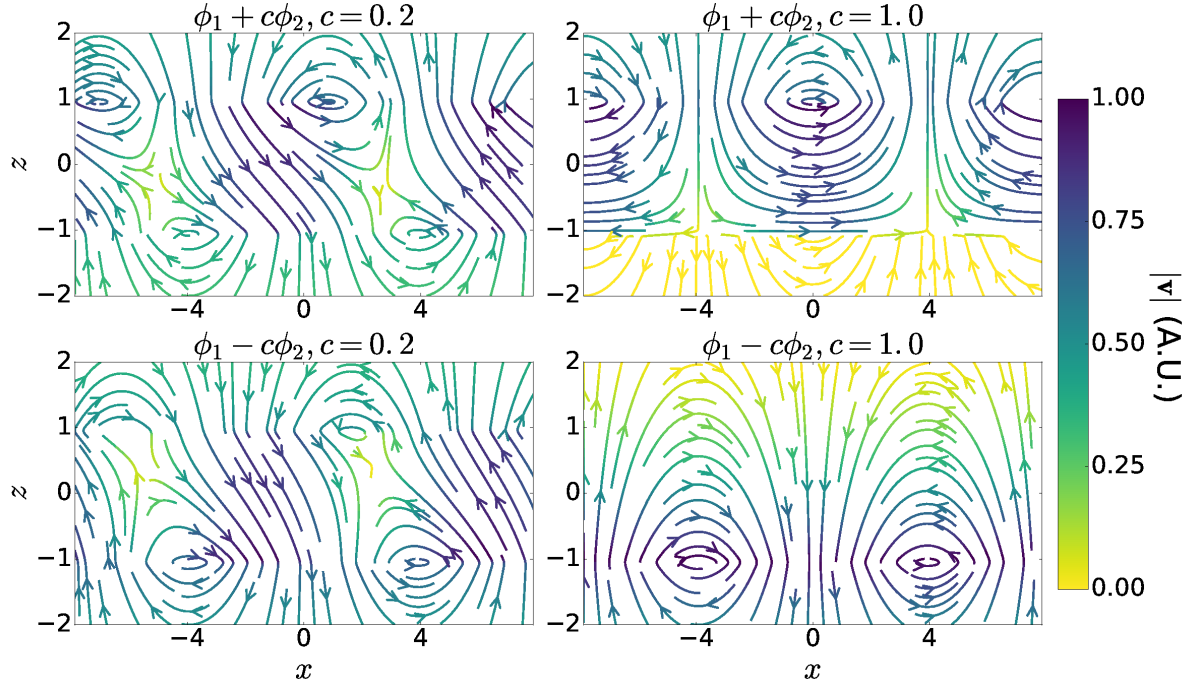


Figure 2.6 Examples of superpositions of stable and unstable modes at $k = 0.4$ plotted over one wavelength in x and from $z = -2$ to $z = 2$ (cf. Fig. 2.2). In the right column, the unstable and stable modes have an equal contribution to the overall flow. In the top and bottom rows, the relative phase between the two modes is $+\pi$ and $-\pi$, respectively.

$\tau_{ij} = \langle v_{1i}v_{1j} \rangle$ across the interface. Integrating $d\tau_{xz}/dz$ across the interface gives

$$S = -\lim_{\epsilon \rightarrow 0} \int_{1-\epsilon}^{1+\epsilon} dz \langle v_{1x}v_{1z} \rangle = -\lim_{\epsilon \rightarrow 0} \int_{1-\epsilon}^{1+\epsilon} dz \frac{d}{dz} \left\langle \frac{d\Phi}{dz} \frac{\partial\Phi}{\partial x} \right\rangle$$

where $\langle \rangle$ denotes averaging in x , while \mathbf{v}_1 is the perturbed velocity. Taking

$\Phi = \mathcal{F}^{-1}[\hat{\phi}]$ with $\hat{\phi} = \beta_1\phi_1 + \beta_2\phi_2$ gives

$$\begin{aligned} S = \int_{-\infty}^{\infty} \frac{dk}{2\pi} 4k^2 e^{2|k|} & \left[\text{Im}(\omega_1^*) |\beta_1|^2 + \text{Im}(\omega_2^*) |\beta_2|^2 \right. \\ & \left. + \text{Im}[(\omega_2^* + k)\beta_1\beta_2^*] + \text{Im}[(\omega_1^* + k)\beta_2\beta_1^*] \right]. \end{aligned} \quad (2.23)$$

When the stable modes are ignored, only the first term contributes to S .

The coefficient $4k^2 e^{2|k|}$ is positive, and Eq. (2.5) shows that $\text{Im}(\omega_1^*) \leq 0$ and $\text{Im}(\omega_2^*) = -\text{Im}(\omega_1^*)$, indicating that the transport due to unstable modes alone is negative, and the second term acts against the first to reduce $|S|$.

Clearly the amplitude of $\beta_2(k)$ relative to $\beta_1(k)$ has a significant impact on the momentum transport in this system. The relative phase between $\beta_2(k)$ and $\beta_1(k)$ determines the contribution of the last two terms. If $|\beta_2(k)| = |\beta_1(k)|$, then the first two terms cancel and the transport is entirely determined by the last two terms. Analysis of other systems shows there are situations where eigenmode cross correlations significantly affect transport (Baver et al. 2002; Terry et al. 2009).

To determine the actual properties of S , it is necessary to solve

Eqs. (2.17) and (2.18) for $\beta_j(k)$ and integrate Eq. (2.23), either analytically or numerically. This is beyond the scope of the present paper, but will be considered in the future. In lieu of such solutions, we construct an estimate of the ratio $|\beta_2(k)|/|\beta_1(k)|$ using the threshold parameter.

In the previous section the threshold parameter was defined as the ratio of the maximum amplitudes of the C_2 terms and the C_1 terms in Eq. (2.17) at the onset of saturation. An estimate of $|\beta_2(k)|/|\beta_1(k)|$ in terms of P_t is obtained by taking

$$P_t \sim \frac{|2C_2\beta_1(k')\beta_2(k'')|}{|C_1\beta_1(k')\beta_1(k'')|} = 2 \left| \frac{C_2}{C_1} \right| \frac{|\beta_2(k'')|}{|\beta_1(k'')|} \sim 2 \left| \frac{\beta_2(k)}{\beta_1(k)} \right|.$$

While the threshold parameter estimates the relative amplitudes of the modes, it does not capture information about their cross-phase. Taking $\beta_2 = \beta_1 \exp[i\theta_{12}]P_t/2$ allows S to be rewritten as

$$S = \int_{-\infty}^{\infty} \frac{dk}{2\pi} 4k^2 e^{2|k|} |\beta_1|^2 \left\{ \text{Im}(\omega_1^*) \left(1 - \frac{P_t^2}{4} \right) + \frac{P_t}{2} \text{Im} [\omega_1^*(2i \sin(\theta_{12}))] \right\}. \quad (2.24)$$

Due to the form of ω_1 [see Fig. 2.1], the first term is only nonzero for $|k| \lesssim 0.64$, and the second term is only nonzero for $|k| \gtrsim 0.64$. It is clear that $P_t \sim 1$ reduces the magnitude of the first term, while the contribution of the second term to S depends significantly on the cross-phase θ_{12} between the eigenmodes.

Having shown that momentum transport can be affected by stable mode activity, we next summarize the main findings of this paper.

2.6 Conclusion

Shear-flow instabilities are widely studied due to their potential to drive turbulence in systems where the turbulent transport of momentum, particles, and heat are of interest. While the linear regime of these instabilities are generally well-understood, saturation and the resulting nonlinear flows are difficult to model. We have presented a nonlinear analysis of an unstable shear layer with piecewise-linear shear flow, showing that the complex conjugate stable linear eigenmode is excited nonlinearly and strongly affects saturation. This result is significant because it represents the first demonstration that nonlinear excitation of linearly stable modes is an important aspect of saturation in global-scale unstable plasma and hydrodynamic systems. Previous studies were limited to quasihomogeneous systems on gyroradius scales (Terry et al. 2006; Makwana et al. 2011). A critical aspect of this work is the development of a mapping technique that allows analytical saturation analyses derived for spatially homogeneous systems to be applied to the strongly inhomogeneous situation of shear flow instability.

Assuming the flow is a linear combination of the linear eigenmodes

allows the global state of the system to be described in terms of its behavior at the edges of the shear layer (as is also done to determine the dispersion relation). The nonlinearity, originally written in terms of flow components and their spatial derivatives, is then written in terms of the eigenmodes to demonstrate that unstable modes nonlinearly pump stable modes. This allows the eigenfunctions of this system to be treated similarly to the eigenvectors of previous systems. Using a parameter that quantifies the threshold for a stable mode to impact saturation, we have estimated the impact of stable modes on instability saturation and found it to be significant.

Analysis of the flow associated with stable modes indicates that, at the predicted saturation levels, the fluctuating flow undergoes significant topological changes relative to flows characterized by the unstable mode alone. Such changes may affect the propensity for the turbulent flow structure to generate secondary structures through transient amplification and other processes. Because the system described here is inviscid, this work indicates that stable modes have the potential to modify the evolution of instabilities even when they are not subject to dissipation.

Finally, we consider the contribution of stable modes to momentum transport and give an estimate in terms of the threshold parameter, demon-

strating that stable modes can significantly reduce the broadening of the shear layer, thereby counteracting the effect of the unstable modes. One may similarly expect that stable modes can affect other transport channels such as matter entrainment and heat transport. This line of inquiry will be left for future investigations.

The authors would like to thank F. Waleffe for valuable discussions and insights. Partial support for this work was provided by the Wisconsin Alumni Research Foundation and the U S Department of Energy, Office of Science, Fusion Energy Sciences, under award No. DE-FG02-89ER53291.

A Coupling Coefficients

In Eqs. (2.17) and (2.18), the nonlinear coupling coefficients C_j, D_j , which are obtained by expressing the nonlinearities of Eq. (2.16) in terms

of the eigenmode amplitudes β_j , are as follows:

$$\begin{aligned}
C_1 &= \alpha \left[(b_2 b'_1 + b''_1) e^{2|k''|} + (b_2 b''_1 + b'_1) e^{2|k'|} \right] \\
C_2 &= \alpha \left[(b_2 b'_1 + b''_2) e^{2|k''|} + (b_2 b''_2 + b'_1) e^{2|k'|} \right] \\
C_3 &= \alpha \left[(b_2 b'_2 + b''_1) e^{2|k''|} + (b_2 b''_1 + b'_2) e^{2|k'|} \right] \\
C_4 &= \alpha \left[(b_2 b'_2 + b''_2) e^{2|k''|} + (b_2 b''_2 + b'_2) e^{2|k'|} \right] \\
D_1 &= -\alpha \left[(b_1 b'_1 + b''_1) e^{2|k''|} + (b_1 b''_1 + b'_1) e^{2|k'|} \right] \\
D_2 &= -\alpha \left[(b_1 b'_1 + b''_2) e^{2|k''|} + (b_1 b''_2 + b'_1) e^{2|k'|} \right] \\
D_3 &= -\alpha \left[(b_1 b'_2 + b''_1) e^{2|k''|} + (b_1 b''_1 + b'_2) e^{2|k'|} \right] \\
D_4 &= -\alpha \left[(b_1 b'_2 + b''_2) e^{2|k''|} + (b_1 b''_2 + b'_2) e^{2|k'|} \right], \tag{A1}
\end{aligned}$$

where

$$\alpha = \frac{i k |k'| |k''| e^{-|k|-|k'-|k''|}}{2|k|(b_1 - b_2)},$$

with $b'_j \equiv b_j(k')$ and $b''_j \equiv b_j(k'')$. For convenience, the definition of $b_j(k)$ is repeated here:

$$b_j = e^{2|k|} \frac{2|k|(\omega_j + k) - k}{k}.$$

Notice that $\alpha(k, k') = \alpha(k, k - k')$ and $C_3(k, k') = C_2(k, k - k')$. Thus,

changing the integration variable to $k'' = k - k'$ in the C_3 integral yields

$$\begin{aligned}
\int_{-\infty}^{\infty} \frac{dk'}{2\pi} C_3(k, k') \beta_1(k'') \beta_2(k') &= \int_{-\infty}^{\infty} \frac{dk'}{2\pi} C_2(k, k'') \beta_1(k'') \beta_2(k') \\
&= \int_{-\infty}^{\infty} \frac{dk''}{2\pi} C_2(k, k'') \beta_1(k'') \beta_2(k - k'') \\
&= \int_{-\infty}^{\infty} \frac{dk'}{2\pi} C_2(k, k') \beta_1(k') \beta_2(k - k'),
\end{aligned}$$

so the C_3 and C_2 integrals in Eq. (2.17) are identical.

References

- Baines, P. G., & Mitsuderaf, H. 1994, Journal of Fluid Mechanics, 276, 327
- Baver, D. A., Terry, P. W., Gatto, R., & Fernandez, E. 2002, Physics of Plasmas, 9, 3318
- Browning, K. A. 1971, Quarterly Journal of the Royal Meteorological Society, 97, 283
- Case, K. M. 1960, Physics of Fluids, 3, 143
- Chandrasekhar, S. 1961, Hydrodynamic and Hydromagnetic Stability (Oxford University Press)
- Churchwell, E. 1997, The Astrophysical Journal, 479, L59
- Dimits, A. M., Williams, T. J., Byers, J. A., & Cohen, B. I. 1996, Physical Review Letters, 77, 71
- Drazin, P. G., & Howard, L. N. 1962, Journal of Fluid Mechanics, 14, 257–283
- Drazin, P. G., & Reid, W. 1981, Hydrodynamic Stability (Cambridge University Press)
- Gerwin, R. A. 1968, Rev. Mod. Phys., 40, 652
- Hatch, D. R., Pueschel, M. J., Jenko, F., et al. 2012, Physical Review Letters, 108, 235002
- Heifetz, E., Mak, J., Nycander, J., & Umurhan, O. M. 2015, Journal of Fluid Mechanics, 767, 199
- Kwak, K., Shelton, R. L., & Henley, D. B. 2015, The Astrophysical Journal, 812, 111
- Lecoanet, D., McCourt, M., Quataert, E., et al. 2016, Monthly Notices of the Royal Astronomical Society, 455, 4274
- Makwana, K. D., Terry, P. W., Kim, J.-H. H., & Hatch, D. R. 2011, Physics of Plasmas, 18, 012302

- Palotti, M. L., Heitsch, F., Zweibel, E. G., & Huang, Y. 2008, The Astrophysical Journal, 678, 234–244
- Pueschel, M. J., Faber, B. J., Citrin, J., et al. 2016, Physical Review Letters, 116, 085001
- Rieger, F. M., & Duffy, P. 2006, The Astrophysical Journal, 652, 1044
- Rogers, B. N., Dorland, W., & Kotschenreuther, M. 2000, Physical Review Letters, 85, 5336
- Terry, P., & Horton, W. 1982, Physics of Fluids, 25, 491
- Terry, P. W., Baver, D. A., & Gupta, S. 2006, Physics of Plasmas, 13, 022307
- Terry, P. W., Baver, D. A., & Hatch, D. R. 2009, Physics of Plasmas, 16, 122305
- Terry, P. W., & Gatto, R. 2006, Physics of Plasmas, 13, 062309

Chapter 3

Role of stable modes in driven shear-flow turbulence

*A version of this chapter has previously appeared
in Physics of Plasmas*

Fraser, et al. 2018, Phys. Plasmas, 25, 122303

Abstract

A linearly unstable, sinusoidal $E \times B$ shear flow is examined in the gyrokinetic framework in both the linear and nonlinear regimes. In the linear regime, it is shown that the eigenmode spectrum is nearly identical to hydrodynamic shear flows, with a conjugate stable mode found at every unstable wavenumber. In the nonlinear regime, turbulent saturation of the instability is examined with and without the inclusion of a driving term that prevents nonlinear flattening of the mean flow, and a scale-independent radiative damping term that suppresses the excitation of conjugate stable modes. From a variety of analyses, the nonlinear state is found to have a significant component associated with stable modes. The role of these modes is investigated through a simple fluid model that tracks how momentum transport and partial flattening of the mean flow scale with the driving term. From this model it is shown that, except at high radiative damping, stable modes play an important role in the turbulent state and yield significantly improved quantitative predictions when compared with corresponding models neglecting stable modes.

3.1 Introduction

The prevalence of sheared flows in diverse systems has motivated their study for over a century. Their potential to drive instabilities and turbulence in fluids and plasmas is central to angular momentum transport in astrophysical disks (Balbus & Hawley 1998; Vanon & Ogilvie 2016), to transport in the Earth’s magnetosphere (Faganello & Califano 2017), and possibly to the generation and saturation of confinement-modifying zonal flows in fusion devices (Rogers et al. 2000). The linear stability of simple shear flow configurations has been thoroughly investigated from linear equations (Chandrasekhar 1961; Drazin & Reid 1981) and provides a rough understanding of the nature of more complex flow profiles early in their development, before unstable perturbations grow too large (Gaster et al. 1985; Palotti et al. 2008). However, as these flows develop beyond the regime of validity of linearized models, and nonlinear interactions between different components of the fluctuation become important, capturing or understanding their behavior with any set of constructs based on linear analysis becomes problematic (Liou & Morris 1992; Nikitopoulos & Liu 2001; Horton et al. 1987).

Instead, studies generally rely on direct numerical simulations to in-

vestigate relevant physical effects (Faganello & Califano 2017; Palotti et al. 2008; Henri et al. 2013). In many cases of interest, these methods cannot produce solutions for physically relevant parameters, such as the high Reynolds numbers found in astrophysical systems. This motivates the development of scaling models that can inform how the system extrapolates to parameter regimes inaccessible to simulations. Valid scaling models require an understanding of the physics of all relevant phenomena, including turbulent responses that modify the unstable flow, like nonlinear fluctuation structures, cascades, and momentum transport.

Regarding nonlinear processes that become relevant as the linear growth phase ends, recent analytical work on shear-flow instability saturation has demonstrated the importance of fluctuation dissipation that arises at large scales due to excitation of stable modes (Fraser et al. 2017). When an unstable shear flow is perturbed from equilibrium, these linear modes are generally a part of the initial perturbation, decaying from their small initial amplitude. Given this initial decay, stable modes are typically ignored in constructing reduced nonlinear models that draw from linear physics (Liou & Morris 1992; Nikitopoulos & Liu 2001; Horton et al. 1987). However, nonlinear interactions with unstable modes can drive stable modes to large amplitude. Because they are linearly stable, they provide a route for energy

to be removed from fluctuations at large scales, before it is able to cascade to small scales, thereby modifying the flow, its spectrum, and its transport (Fraser et al. 2017). This represents a significant departure from the usual picture of instability-driven turbulence, where energy injection by unstable modes is assumed to be balanced by conservative nonlinear energy transfer to small, dissipative scales.

While it has been shown that nonlinear interactions with large-scale stable modes can be important in saturating shear-flow instabilities, their amplitude and contribution to the fluctuating flow and momentum transport in fully-developed turbulence remains an open question, which we pursue in this paper. Additionally, we explore whether reduced models of shear-flow-driven turbulence that are based solely on the linear instability might be improved by including the effects of large-scale stable modes. This is a natural expectation given their importance in saturating the instability, their introduction of a large-scale linear energy sink, and their potential to modify momentum transport. This is also motivated by recent work in the context of instability-driven turbulence in fusion devices, where reduced turbulence models that include details of stable modes and instability saturation physics have been shown to be effective (Terry et al. 2018; Hegna et al. 2018; Whelan et al. 2018).

We address these questions by performing direct numerical simulations of an unstable shear flow that develops into turbulence, and comparing the contribution of different linear modes to the turbulent flow and the Reynolds stress. Our simulations are performed using the gyrokinetic turbulence code GENE¹ (Jenko et al. 2000), which has previously been used to examine stable modes in other turbulent systems (Hatch et al. 2011; Terry et al. 2014), and includes both initial value and eigenvalue solvers. This allows us to benchmark our calculated growth rates against previous gyrokinetic studies of the same system (Rogers & Dorland 2005), as well as investigate differences between shear flow instabilities in hydrodynamics and gyrokinetics with regards to both the linear mode spectrum and instability saturation. In particular, while it is understood that all unstable, inviscid, incompressible, two-dimensional (2D) hydrodynamic flows include one stable mode for every unstable mode (Drazin & Reid 1981), and previous work has shown that these stable mode are nonlinearly driven in the fluid system (Fraser et al. 2017), whether these results apply to the gyrokinetic case as well has not been explored. To allow for more direct comparisons with previous work, all simulations presented in this paper are effectively 2D, with no variations in the direction of the strong guide field ($k_z = 0$).

¹See <http://www.genecode.org> for code details and access.

The flow we examine is a sinusoidally-varying $E \times B$ parallel shear flow with periodic boundary conditions. The hydrodynamic counterpart to this flow is often referred to as Kolmogorov flow when it is maintained by a constant forcing term (Platt et al. 1991; Musacchio & Boffetta 2014; Lucas & Kerswell 2014). This flow profile is particularly relevant to astrophysical disks, where its Kelvin-Helmholtz (KH) instability is studied as a saturation mechanism for the magnetorotational instability (Goodman & Xu 1994; Pessah & Goodman 2009; Pessah 2010; Latter et al. 2009, 2010; Longaretti & Lesur 2010) or its collisionless counterpart (Squire et al. 2017), and in fusion devices, where it is studied as a potential secondary and tertiary instability to streamers and zonal flows (Rogers et al. 2000; Kim & Terry 2010). In order to admit a quasi-stationary state of driven turbulence where energy dissipation is balanced by energy injection, we continually reinforce the mean flow using a Krook operator previously employed similarly to reinforce current gradients in tearing mode studies (Pueschel et al. 2014), and referred to as a linear relaxation term in studies of barotropic jets (Marston et al. 2008). With this forcing term, the system bears a strong resemblance to Kolmogorov flow (Platt et al. 1991; Musacchio & Boffetta 2014; Lucas & Kerswell 2014), with the exception that it is not a constant forcing. From a numerical perspective, Kolmogorov flow presents a convenient choice of

unstable shear flow to study due to its simple description in a Fourier basis and the lack of no-slip boundary conditions that could otherwise generate boundary layers. This also allows us to address whether the saturation physics active in the free shear layer (Fraser et al. 2017) is applicable to a driven periodic shear flow.

Our simulations also include damping terms in the form of hyperdissipation and scale-independent radiative damping. The form of the radiative damping term is such that it damps every mode equally. In systems with pairs of stable and unstable modes, this disproportionately affects the stable mode amplitude relative to the unstable one in the nonlinear state (Terry et al. 2009). Thus, varying the degree of radiative damping in our system allows us to assess whether different shear-driven turbulence regimes exist with significantly different stable mode effects, and how these regimes might differ.

The remainder of this paper is organized as follows. Section 3.2 starts with a brief review of hydrodynamic parallel shear flows for comparison with our gyrokinetic results, as well as some unique aspects of the particular flow profile studied here, followed by a discussion of the numerical implementation used in our work, including the specific forms of forcing and dissipation. In Sec. 3.3 we show the full eigenmode spectrum for the gyrokinetic KH in-

stability. A description of the nonlinear evolution of the flow is presented in Sec. 3.4, where we discuss saturation and decaying turbulence when forcing is absent, driven turbulence with external forcing, and turbulent momentum transport in this system. Section 3.5 examines the turbulence in terms of the role played by the linear eigenmodes, and compares reduced descriptions and scaling models of the turbulence with and without stable modes. Conclusions are presented in Sec. 3.6.

Throughout this paper, we adopt the notation that $\hat{A}(x, k_y)$ denotes the Fourier transform in y of $A(x, y)$, and $\tilde{A}(k_x, k_y)$ denotes the Fourier transform in x and y .

3.2 Shear Flow Instability

3.2.1 Rayleigh's Stability Equation

The stability of parallel shear flows is generally investigated by examining infinitesimal perturbations about equilibrium solutions to the Navier-Stokes equation. When considering a 2D, inviscid, incompressible flow that is perturbed from an equilibrium, the vorticity equation becomes

$$\frac{\partial}{\partial t} \nabla^2 \phi + V \frac{\partial}{\partial y} \nabla^2 \phi - \frac{d^2 V}{dx^2} \frac{\partial \phi}{\partial y} + \frac{\partial \phi}{\partial x} \frac{\partial}{\partial y} \nabla^2 \phi - \frac{\partial \phi}{\partial y} \frac{\partial}{\partial x} \nabla^2 \phi = 0, \quad (3.1)$$

where $V(x)$ is the y -directed equilibrium shear flow, and $\phi(x, y, t)$ is the streamfunction of the perturbation $\mathbf{v} = \nabla \phi \times \hat{\mathbf{z}}$. The linear dynamics can

then be explored by dropping the nonlinearities and using the normal mode ansatz

$$\phi(x, y, t) = \sum_{k_y} \sum_j \hat{\phi}_j(x, k_y) e^{i(k_y y + \omega_j t)}, \quad (3.2)$$

yielding

$$(\omega_j + k_y V) \left(\frac{\partial^2}{\partial x^2} - k_y^2 \right) \hat{\phi}_j - k_y \hat{\phi}_j \frac{d^2 V}{dx^2} = 0. \quad (3.3)$$

Equation (3.3) is known as Rayleigh's stability equation, or as the Orr-Sommerfeld equation when the effect of viscosity on ϕ is included. It can be solved as an eigenvalue problem, yielding a set of eigenvalues ω_j and eigenmodes $\hat{\phi}_j$, with j enumerating the eigenmodes at a given k_y . The eigenvalue ω_j is complex, with real frequency $\text{Re}(\omega_j)$ and growth rate $\gamma_j = -\text{Im}(\omega_j)$. If any eigenmode has a positive growth rate, the flow is unstable. Furthermore, taking the complex conjugate of Eq. (3.3) shows that for each unstable solution there exists a stable solution with equal and opposite growth rate (Drazin & Reid 1981). Previous work (Fraser et al. 2017) demonstrated that nonlinear interactions with these stable modes play an important role in saturating the growth of unstable modes. In the present work we perform nonlinear simulations of an unstable shear flow and examine the role played by stable modes beyond the onset of saturation.

3.2.2 Kolmogorov Flow

One unstable flow profile of relevance in fusion and astrophysical systems is a sinusoidal equilibrium flow with periodic boundary conditions (Goodman & Xu 1994; Pessah & Goodman 2009; Pessah 2010; Latter et al. 2009, 2010; Longaretti & Lesur 2010; Squire et al. 2017; Vanon & Ogilvie 2016; Rogers et al. 2000; Rogers & Dorland 2005). For a sinusoidal flow profile $V(x) = V_0 \cos(k_x^{\text{eq}}x)$ in a periodic domain, Eq. (3.3) lends itself well to being solved using spectral methods. Defining $\tilde{\phi}_j(k_x, k_y)$ as the Fourier series expansion of $\hat{\phi}_j(x, k_y)$, the Fourier representation of Eq. (3.3) is

$$\omega_j(k_x^2 + k_y^2)\tilde{\phi}_j + \frac{k_y V_0}{2} \left[(k_x^2 - 2k_x k_x^{\text{eq}} + k_y^2)\tilde{\phi}_j^- + (k_x^2 + 2k_x k_x^{\text{eq}} + k_y^2)\tilde{\phi}_j^+ \right] = 0, \quad (3.4)$$

where $\tilde{\phi}_j^\pm \equiv \tilde{\phi}_j(k_x \pm k_x^{\text{eq}}, k_y)$. Equation (3.4) immediately demonstrates that each eigenmode exhibits a discrete, comb-like structure when viewed through a Fourier transform: for a given eigenmode $\hat{\phi}_j(x, k_y)$, if its Fourier transform $\tilde{\phi}_j(k_x, k_y)$ is nonzero at some k_x , then it is also nonzero at $k_x + nk_x^{\text{eq}}$ for every integer n (though $\tilde{\phi}_j$ is still expected to fall off at large $|k_x|$, so that calculations with a finite number of k_x can be expected to capture the structure well). This property of the system will have important consequences in later sections when we compare simulations with different box sizes, and when we explore the possibility of approximating

the turbulent state by truncating the summation over j in Eq. (3.2) to a reduced number of modes.

3.2.3 Numerical implementation and benchmarking

We perform simulations of a KH-unstable sinusoidal $E \times B$ flow using the gyrokinetic framework (Brizard & Hahm 2007) as implemented in the GENE code (Jenko et al. 2000). The gyrokinetic framework applies to systems with a strong guide field, where the parallel length scale of fluctuations is much larger than the perpendicular length scale, and the relevant frequencies are much smaller than the ion cyclotron frequency. The use of gyrokinetics for this work is motivated by GENE’s unique tools for performing eigenmode decompositions (Hatch et al. 2011; Terry et al. 2014). We simulate a system with two spatial dimensions, with a y -directed flow that varies sinusoidally in x , a strong guide field in the z direction, and no variations in z . Our simulation domain is a periodic box of dimensions $L_x \times L_y$ with no curvature or magnetic shear. The flow arises from the $E \times B$ drift of the particles, allowing the electrostatic potential ϕ to serve as the streamfunction for the flow. We model the plasma with gyrokinetic ions and electrons with hydrogen mass ratio, ion and electron background temperatures $T_i = T_e$, no collisions, and no electromagnetic fluctuations (plasma $\beta = 0$).

We drive instability with a potential and corresponding distribution function that vary sinusoidally in x . GENE uses a δf formalism, where the full distribution function is separated into equilibrium F_0 and fluctuation f , with the code solving for the evolution of the fluctuation. We let $f(x, y, v_{\parallel}, \mu, s, t)$ and $\tilde{f}(k_x, k_y, v_{\parallel}, \mu, s, t)$ denote the (guiding-center) distribution function for species s in real and Fourier space. For the remainder of this paper, we will generally use notation that suppresses the species and velocity dependence of f , and instead focus on its dependence on the spatial coordinates and time.

For benchmarking against previous work (Rogers & Dorland 2005), the instability is first examined by implementing the sinusoidal flow with low-amplitude white noise as an initial condition in the fluctuation, formally evolving the system nonlinearly, with a homogeneous Maxwellian equilibrium F_0 . This corresponds to solving the equation

$$\frac{\partial f}{\partial t} = \{f, \bar{\phi}\} \quad (3.5)$$

with a sinusoidal initial condition $f(t=0), \phi(t=0) \sim \sin(k_x^{\text{eq}}x)$ and low-amplitude noise to seed instability. The only term on the right-hand side of Eq. (3.5),

$$\{f, \bar{\phi}\} \equiv \frac{\partial f}{\partial x} \frac{\partial \bar{\phi}}{\partial y} - \frac{\partial \bar{\phi}}{\partial x} \frac{\partial f}{\partial y}, \quad (3.6)$$

is the $E \times B$ nonlinearity, whose Fourier transform becomes

$\sum_{k'_x, k'_y} (k'_x k_y - k_x k'_y) \tilde{\bar{\phi}}(k'_x, k'_y) \tilde{f}(k_x - k'_x, k_y - k'_y)$. Here, $\bar{\phi}$ is the gyro-averaged ϕ , whose Fourier transform is given by

$$\tilde{\bar{\phi}}(k_x, k_y, \mu, s) = J_0(\sqrt{k_x^2 + k_y^2} \rho) \tilde{\phi}(k_x, k_y),$$

where J_0 is a Bessel function and ρ is the gyroradius of species s with magnetic moment μ . The code evolves f according to Eq. (3.5) and calculates ϕ using Gauss's law as described in Merz (2009) and Pueschel et al. (2011). The normalizations used by GENE are described in Merz (2009); however, in this paper we will follow the standard convention used in the fluids community and normalize quantities with respect to the equilibrium flow velocity V_0 and its wavelength k_x^{eq} , which are normalized in the code by $V_{\text{phys}} = V \rho_s c_s / L_{\text{ref}}$ and $k_{x\text{phys}} = k_x / \rho_s$, where c_s is the ion sound speed and ρ_s is the ion sound Larmor radius.

Consistent with fluid theory, our system is unstable to perturbations of the same form as Eq. (3.2) for a range of perturbation wavenumbers k_y , with the growth rate scaling with the base flow amplitude V_0 . Growth rates from this formally nonlinear setup are indicated by crosses in Fig. 3.1. For direct comparison with previous work (Rogers & Dorland 2005), the wavenumber of the equilibrium k_x^{eq} was varied at fixed k_y , where perturbations are unstable for $0 < k_y/k_x^{\text{eq}} < 1$. For this reason, in the remainder of this paper we focus our discussion on modes that lie in this range.

As demonstrated in Fig. 3.1, nonlinear simulations with appropriate initial conditions can be used to investigate some of the linear dynamics of this system, such as the growth rate and mode structure of the most unstable mode at each k_y . However, to solve for other linear modes, which are known to exist in fluid models (Drazin & Reid 1981), terms corresponding to interaction with the driving flow need to be implemented as a linear operator, so that Eq. (3.5) can be linearized similarly to Eq. (3.3), in the

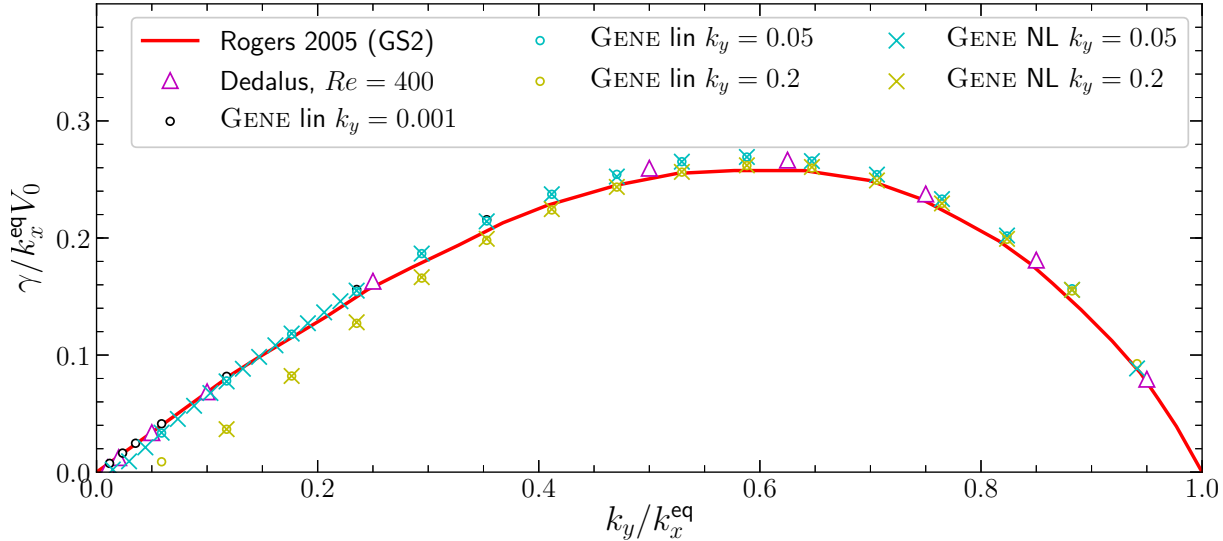


Figure 3.1 Dispersion relation for the KH instability of a sinusoidal flow $\mathbf{V} = V_0 \cos(k_x^{\text{eq}}x)\hat{y}$. Growth rate γ is plotted against the wavenumber k_y of the perturbation, with γ normalized to the equilibrium shear $k_x^{\text{eq}}V_0$ and k_y to the equilibrium wavenumber k_x^{eq} . Crosses are obtained from nonlinearly evolving a perturbed sinusoidal flow in GENE according to Eq. (3.5), while dots are from solving the linear Eq. (3.7). Results compare well with both previous gyrokinetic simulations (red curve, see Rogers & Dorland 2005) and hydrodynamic simulations of an equivalent system (magenta triangles). The stabilization of the $k_y = 0.2$ points at low k_y/k_x^{eq} (i.e. high k_x^{eq}) can be attributed to finite Larmor radius effects. All modes have zero real frequency.

form

$$\frac{\partial f}{\partial t} = \mathcal{L}_{\text{KH}}[f] \quad (3.7)$$

for a linear differential operator \mathcal{L}_{KH} . To that end, we have implemented the linear operator \mathcal{L}_{KH} in the GENE code. This allows computations to be performed with $\mathcal{L}_{\text{KH}}[f]$ on the right-hand side of the equation for $\partial_t f$ for

$$\mathcal{L}_{\text{KH}}[f] \equiv \{f_0, \bar{\phi}\} + \{f, \bar{\phi}_0\}, \quad (3.8)$$

where ϕ_0 is the electrostatic potential (streamfunction) for the sinusoidal base flow, and f_0 is the self-consistent distribution function corresponding to ϕ_0 . Specifically, we use

$$f_0(s) = \frac{V_0}{k_x^{\text{eq}}} \frac{\delta_{k_x, k_x^{\text{eq}}} - \delta_{k_x, -k_x^{\text{eq}}}}{2i} F_0(s) \frac{q_s}{T_s} J_0 \frac{1 - \Gamma_0}{\Gamma_0}, \quad (3.9)$$

where δ_{k_x, k'_x} is the Kronecker delta, and $F_0(s)$, q_s , and T_s are the equilibrium Maxwellian, charge, and temperature of species s . Here, $J_0(k_\perp \rho)$, a Bessel function, and $\Gamma_0(b) = e^{-b} \hat{I}_0(b)$ (where \hat{I}_0 is a modified Bessel function, $b(s) = v_{Ts}^2 k_\perp^2 \Omega_s^{-2}/2$, and v_{Ts} and Ω_s are the thermal velocity and Larmor frequency of species s) relate to finite Larmor radius (FLR) effects as detailed in Merz (2009) and Pueschel et al. (2011). This form of f_0 is used for secondary instability tests in tokamak-relevant systems (Pueschel et al. 2013), and yields a sinusoidal $\phi_0(x)$ corresponding to a sinusoidal equilibrium flow in the y direction with amplitude V_0 and wavenumber k_x^{eq} .

Note that \mathcal{L}_{KH} has x dependence but no y dependence, so its eigenmodes will have Fourier dependence in y and more complex structure in x , similar to the hydrodynamic case discussed in Sec. 3.2.1. The dots in Fig. 3.1 are obtained by solving Eq. (3.7), and their agreement with the corresponding crosses demonstrates successful implementation of the linear drive. For both setups, convergence checks were performed in spatial and velocity coordinates. Well-converged growth rates generally require 33 grid points in x , though far fewer points were required for $k_y/k_x^{\text{eq}} \lesssim 0.5$. For the remainder of this paper, results are presented with $V_0 = 10$ and $k_x^{\text{eq}} = 0.1$ using the linearized \mathcal{L}_{KH} . A convenient consequence of these parameters is that times and frequencies have the same value when expressed in standard GENE normalizations as they do in typical normalizations used in calculations of unstable shear flow in the fluids community, where t is often measured in units of $(k_x^{\text{eq}} V_0)^{-1}$.

Magenta triangles in Fig. 3.1 are obtained from solving the Orr-Sommerfeld equation with the Dedalus code² (Burns et al. 2020) (where k_x^{eq} is the only length scale in the system) with a Reynolds number $Re = 400$. Their agreement with the other curves supports the notion that kinetic effects do not play a significant role in determining the growth rate of this

²See <http://dedalus-project.org> for details.

mode. Crosses and dots in Fig. 3.1 corresponding to lower values of k_y show especially good agreement with the fluid results. As each curve represents a fixed k_y with varying k_x^{eq} , finite Larmor radius (FLR) effects become more important as k_x^{eq} increases (i.e. as k_y/k_x^{eq} decreases), suggesting that the reduced growth rates in the $k_y = 0.2$ simulations relative to the fluid results are due to FLR effects. In non-periodic shear layers, such as $V \sim \tanh(x)$, it is observed that FLR effects can be stabilizing or destabilizing depending on the alignment of the equilibrium vorticity and magnetic field (Faganello & Califano 2017; Henri et al. 2013). Due to the sinusoidal nature of the flow studied here, the simulation domain includes regions where vorticity and magnetic field are aligned and where they are anti-aligned, suggesting that the FLR stabilization observed in our system is qualitatively different from what is found in shear layers. We speculate that the FLR stabilization is due to a reduction in the gyro-averaged potential $\bar{\phi}$, as $\bar{\phi}/\phi$ generally decreases with increasing k .

3.2.4 Forcing and dissipation terms

In this paper, nonlinear calculations often include additional terms corresponding to forcing and dissipation, which we introduce here. Hyperdissipation $-D_{\perp}(k_x^4 + k_y^4)\tilde{f}$ (Pueschel et al. 2010) is employed to provide small-scale dissipation in place of collisions, which are not expected to suf-

ficiently dissipate small-scale fluctuations at achievable resolutions within valid limits of collision models. We note that our hyperdissipation term differs from what is more standard in the fluids community, where $k_x^4 + k_y^4$ is replaced by $(k_x^2 + k_y^2)^2$. A second dissipative term $-D_{\text{rad}}\tilde{f}$ is spatially uniform and sometimes referred to as radiative damping or friction (Tobias et al. 2011). It absorbs energy transferred to large scales (Tobias et al. 2011; Reynolds-Barredo et al. 2016), while also serving as a “symmetry-breaking” parameter that adjusts the relative growth rates of linear modes without modifying their structure.

Finally, we introduce a Krook operator $-D_{\text{Krook}}\delta_{k_x,\pm k_x^{\text{eq}}}\delta_{k_y,0}\tilde{f}$, where $\delta_{i,j}$ is the Kronecker delta, to represent forcing of the unstable equilibrium and prevent it from decaying due to turbulent fluctuations (Pueschel et al. 2014). Aside from being linear in f and therefore not constant in time, this is identical to the inhomogeneous body forcing used in studies of Kolmogorov flow (Platt et al. 1991; Musacchio & Boffetta 2014; Lucas & Kerswell 2014). While the sign of the Krook operator seems to suggest that it removes energy from the system, that is merely a consequence of our separation between equilibrium and perturbation. As explained in Waleffe (1995), the kinetic energy of the full flow is $E = \int |\mathbf{V} + \mathbf{v}|^2 dx dy$, so that if the $(k_x, k_y) = (k_x^{\text{eq}}, 0)$ component of \mathbf{v} opposes that of \mathbf{V} and is not larger in

magnitude, as we will see to be the case in Sec. 3.4, terms that appear to dissipate the “perturbation energy” $\int |\mathbf{v}|^2 dx dy$ at that wavenumber will actually increase the true energy E .

Having constructed a linear operator that yields consistent results for the most unstable eigenmode’s growth rate, we now address the rest of the spectrum of eigenvalues.

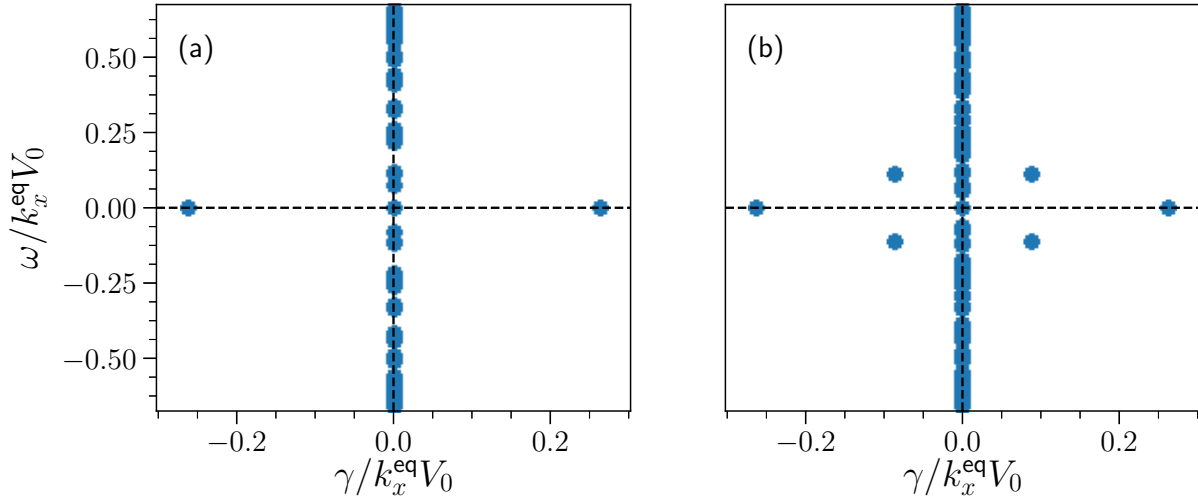


Figure 3.2 Eigenvalue spectra for $k_y/k_x^{\text{eq}} = 2/3$ with $L_x = \lambda^{\text{eq}}$ (a) and $L_x = 2\lambda^{\text{eq}}$ (b). With $L_x = \lambda^{\text{eq}}$, at each unstable k_y , the spectrum includes one unstable and one stable mode with equal and opposite growth rate γ , as well as a continuous spectrum of marginal modes corresponding to resonances between the phase velocity ω/k_y and equilibrium flow (Case 1960). As the box size is increased to fit multiple wavelengths of the equilibrium, additional stable and unstable modes are introduced (Goodman & Xu 1994; Pessah & Goodman 2009), and additional marginal eigenvalues appear due to an increase in number of values of $V_0 \cos(k_x^{\text{eq}}x)$ sampled by the extended grid (thus additional resonances with ω/k_y).

3.3 Eigenspectrum

3.3.1 Subdominant modes

At each k_y there exists a spectrum of eigenmodes \hat{f}_j and eigenvalues ω_j , with corresponding potential structures $\hat{\phi}_j$. For $0 < k_y/k_x^{\text{eq}} < 1$, we let $j = 1$ denote the fastest-growing mode. The KH instability has been investigated in gyrokinetics before, but previous calculations did not address linear modes other than \hat{f}_1 or their role in saturation. With the linear operator \mathcal{L}_{KH} now implemented in GENE, its full spectrum of eigenmodes and eigenvalues can be obtained (Kammerer et al. 2008; Hatch et al. 2011; Terry et al. 2014). Like the inviscid fluid analog, for each k_y in the unstable range there exist one unstable mode, one stable (damped) mode with equal and opposite growth rate (Drazin & Reid 1981), and a continuum of marginally stable modes (Case 1960), shown in Fig. 3.2 (a) for $k_y/k_x^{\text{eq}} = 2/3$. The additional degrees of freedom gained in gyrokinetics relative to a fluid calculation, by taking into account the velocity-space structure of multiple species, increases the rank of the discretized linear operator considerably, and leads to many more marginally stable modes. A single point on the marginally stable continuum in Fig. 3.2 corresponds to hundreds of eigenmodes (depending on velocity-space resolution), each with similar electrostatic potentials but significantly different velocity-space structure.

Despite the added degrees of freedom in gyrokinetics, there are still only one stable and one unstable eigenmode per k_y for $0 < k_y/k_x^{\text{eq}} < 1$ when the box size L_x equals the wavelength of the equilibrium flow, denoted by $\lambda^{\text{eq}} \equiv 2\pi/k_x^{\text{eq}}$. Consistent with magnetohydrodynamic (MHD) studies of a similar system (Goodman & Xu 1994; Pessah & Goodman 2009), we find that flows where multiple wavelengths of the equilibrium are present (i.e. setting $L_x = n\lambda^{\text{eq}}$ where $n \geq 2$ is an integer) exhibit pairs of subdominant unstable ($0 < \gamma_j < \gamma_1$) and stable ($\gamma_2 < \gamma_j < 0$) modes, shown in Fig. 3.2 (b). This means that simulations with larger boxes but with an equilibrium flow of the same wavelength are expected to have different dynamics than simulations with $L_x = \lambda^{\text{eq}}$, as they include additional modes through which \mathcal{L}_{KH} can inject or remove energy. In Sec. 3.4 we will demonstrate that including D_{Krook} and D_{rad} admits a system where, for sufficiently large L_x , observables are converged with respect to a further increase in L_x .

As stated above, for each k_y in $0 < k_y/k_x^{\text{eq}} < 1$, we let $j = 1$ refer to the dominant unstable mode. We will further let $j = 2$ refer to the corresponding stable mode, and $j > 2$ to all other modes. Figure 3.3 shows the x -dependence of $\hat{\phi}_1$ at $k_y/k_x^{\text{eq}} = 1/2$ alongside the streamfunction for the equilibrium flow. Consistent with the fluid case (Fraser et al. 2017; Drazin & Reid 1981), we find $\gamma_2 = -\gamma_1$ (such that both $|\gamma_{1,2}|$ are reduced by FLR

effects), and $\hat{\phi}_2(x, k_y) = \hat{\phi}_1^*(x, k_y)$. Accordingly, we refer to f_2 as a conjugate stable mode.

Consistent with the fluid case discussed in Sec. 3.2.2, the sinusoidal nature of the equilibrium gives eigenmodes a discrete, comb-like structure in k_x , where \tilde{f}_j is zero at every k_x except for a countably infinite number of k_x that are each separated by k_x^{eq} . All of the modes whose eigenvalues are plotted in Fig. 3.2 (a), including \tilde{f}_1 and \tilde{f}_2 , have nonzero amplitudes at

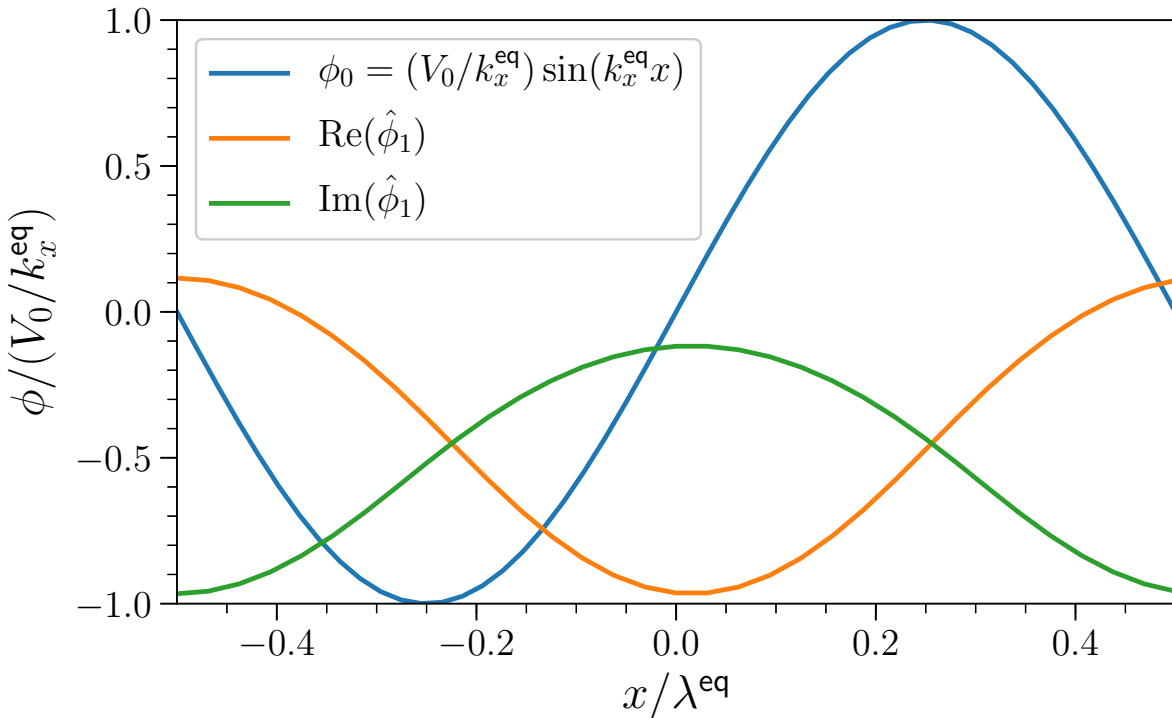


Figure 3.3 The equilibrium potential ϕ_0 considered throughout this paper, which generates an $E \times B$ flow along the y -axis that varies sinusoidally in the x direction with wavenumber k_x^{eq} , alongside the real and imaginary parts of the potential corresponding to the unstable eigenmode $\hat{\phi}_1(x, k_y)$ plotted with respect to x at $k_y/k_x^{\text{eq}} = 1/2$. The stable eigenmode's potential is the complex conjugate of the unstable eigenmode's potential, $\hat{\phi}_2 = \hat{\phi}_1^*$.

integer multiples of k_x^{eq} . Many of the additional modes gained in Fig. 3.2 (b) by extending L_x to $2\lambda^{\text{eq}}$, such as the modes with finite growth rate and real frequency, are nonzero at half-integer multiples of k_x^{eq} . This implies that arbitrary linear combinations of the modes in Fig. 3.2 (a) are only nonzero at integer multiples of k_x^{eq} .

3.3.2 Forcing and dissipation effects

The additional physics effects introduced in Sec. 3.2.4 each modify the eigenmodes to varying degrees. The Krook operator enters the Vlasov equation only at $k_y = 0$, so it has no impact on the $k_y > 0$ eigenmode spectra. The radiative damping term reduces the growth rate of every eigenmode by D_{rad} without changing the mode structure. The hyperdissipation term has a more significant impact on the spectrum. It reduces the growth rate of the unstable mode with minor modifications to its structure, and replaces both the stable mode and marginal continuum with a set of damped modes that does not include any mode resembling the conjugate stable mode.

We now turn our attention the nonlinear saturation of this system.

3.4 Instability saturation

3.4.1 Saturation and decaying turbulence

To investigate the saturation of this instability, we include in Eq. (3.7) the full $E \times B$ nonlinearity, yielding

$$\frac{\partial f}{\partial t} = \mathcal{L}_{\text{KH}}[f] + \{f, \bar{\phi}\}. \quad (3.10)$$

Owing to the way in which the linear drive terms were derived and implemented, the evolution of Eq. (3.10) with some initial condition f_{init} is identical to the evolution of Eq. (3.5) with the initial condition $f_0 + f_{\text{init}}$,

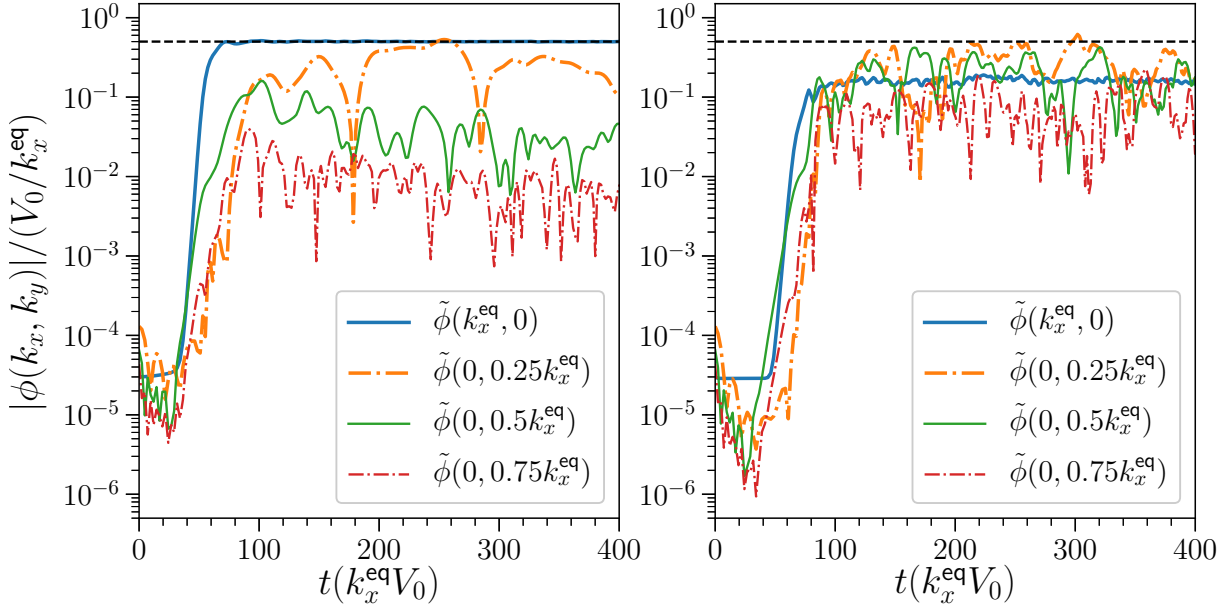


Figure 3.4 Left: Nonlinear simulations with dissipation quasilinearly flatten, then decay. Quasilinear flattening is measured by investigating $\tilde{\phi}$ at $(k_x, k_y) = (\pm k_x^{\text{eq}}, 0)$. The perturbation cancels the drive once $\tilde{\phi}(k_x^{\text{eq}}, 0)$ (blue) reaches a magnitude of $0.5V_0/k_x^{\text{eq}}$ (black dashed line). Linearly unstable Fourier modes then turbulently decay over time. Right: Introducing a Krook operator ($D_{\text{Krook}}/(k_x^{\text{eq}}V_0) = 1$ here) partially suppresses the Fourier mode responsible for quasilinear flattening, driving the system and leading to a quasi-stationary state of driven turbulence.

presuming no dissipation or drive is included. When dissipation terms are added to Eq. (3.10), they do not act on f_0 , unlike those in Eq. (3.5).

As the system evolves according to Eq. (3.10), the nonlinearity transfers energy across a range of scales, but with zero energy injection and nonzero dissipation, the initial energy eventually decays away. In terms of saturation of a linear instability, this can be understood as quasilinear flattening, where the fluctuations reduce mean gradients until the system is linearly stable. This is observed in simulations of Eq. (3.10) with added hyperdissipation, as shown in Figs. 3.4 and 3.5. Once unstable wavenumbers reach a sufficient amplitude, fluctuations at the wavenumbers of the equilibrium flow, i.e. $(k_x, k_y) = (\pm k_x^{\text{eq}}, 0)$, quickly grow to offset the unstable profile of the mean flow. From this point the system exhibits features of decaying turbulence: the dynamics are highly intermittent, with long periods of coherent behavior punctuated by the merging of vortices. This is consistent with previous 2D KH simulations (Faganello & Califano 2017), and can be expected given the lack of external forcing; the linear drive in Eq. (3.10) appears similar to an external forcing term, but as argued in the preceding paragraph, that is merely a consequence of the formal separation between the equilibrium and fluctuations.

3.4.2 Driven turbulence

In many physical systems where shear-flow instability saturation and turbulence are of interest, the unstable shear flow is not some ideal initial condition but is brought about by a separate process. Examples include shear flows driven by boundary conditions (Brandst  ter et al. 1983), drift-wave instabilities (Rogers et al. 2000; Rogers & Dorland 2005) in laboratory experiments, and jets, gravity, or another instability (Goodman & Xu 1994) in astrophysical systems. We include a Krook operator, introduced in Sec. 3.2, with the intent of capturing some of the effects of such continual forcing but without modeling the subtleties of any particular system where forcing produces a shear flow.

The result of including the Krook operator is readily seen in Figs. 3.4

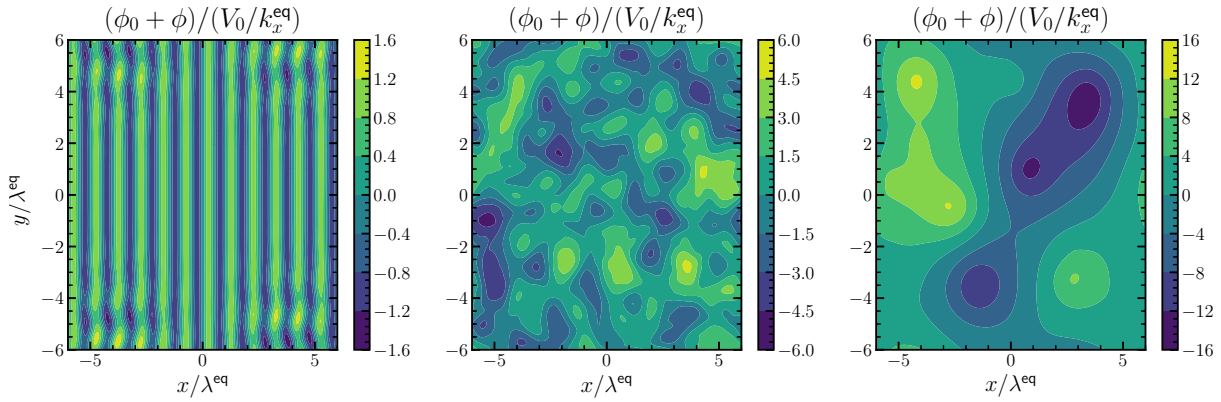


Figure 3.5 Contours of the full (equilibrium and fluctuation) electrostatic potential for a nonlinear simulation with $D_{\text{Krook}} = 0$. From left to right, plots correspond to $t(k_x^{\text{eq}} V_0) \approx 46, 101$, and 502 . Center and right plots show the tendency for small-scale fluctuations to dissipate, leaving coherent vortices that merge to progressively larger scales.

and 3.6. When the Krook operator is added to Eq. (3.10), it suppresses the tendency for the $(k_x, k_y) = (\pm k_x^{\text{eq}}, 0)$ component of the fluctuation to cancel out f_0 , thereby injecting energy into the system by reinforcing the unstable equilibrium. This in turn drives other Fourier modes via the KH instability, as is seen in the time trace of $\tilde{\phi}(k_x^{\text{eq}}, 0)$, shown in Fig. 3.4: the $(k_x, k_y) = (\pm k_x^{\text{eq}}, 0)$ component no longer reaches the amplitude necessary to cancel out the driving shear flow, and other Fourier modes no longer decay over time, leading to a quasi-stationary state of driven turbulence where the energy injected by the Krook drive is balanced by energy dissipation. As D_{Krook} increases, the saturated amplitude of $\tilde{\phi}(\pm k_x^{\text{eq}}, 0)$ decreases, corresponding to an overall increase in $\tilde{\phi}_0 + \tilde{\phi}(\pm k_x^{\text{eq}}, 0)$. The dominant balance that determines the amplitude of $\tilde{\phi}(\pm k_x^{\text{eq}}, 0)$ in saturation is between the Krook drive and the Reynolds stress, which we explore further in Sec. 3.4.3.

Also observed in Fig. 3.5 is the tendency for the system to form coherent vortices that gradually merge to the largest scale allowed by the simulation domain. This behavior is also observed in 2D shear layer simulations (Faganello & Califano 2017), and is consistent with the inverse energy cascade to large scales in 2D hydrodynamics. The inverse cascade leads to a system with saturation properties that change as the box size is increased. The radiative damping term D_{rad} introduced in Sec. 3.2 damps

low- k fluctuations, preventing energy from continuously building up at the largest scales, and thereby allowing fluctuation spectra to reach a stationary condition at low k . For this reason, and for the sake of presenting simulations where observables are converged with respect to the box size, the majority of our simulations were run with $L_x = 12\lambda^{\text{eq}}$ and $D_{\text{rad}} = 0.05$, a rate that is roughly 20% of the maximum linear growth rate in the dissipationless case. Figure 3.6 shows the results of a simulation with these parameters and $D_{\text{Krook}} = 1$. In contrast with Fig. 3.5, the system exhibits multiple excited scales in a quasi-stationary saturated state, providing the type of turbulence desired for studying momentum transport and eigenmode excitation.

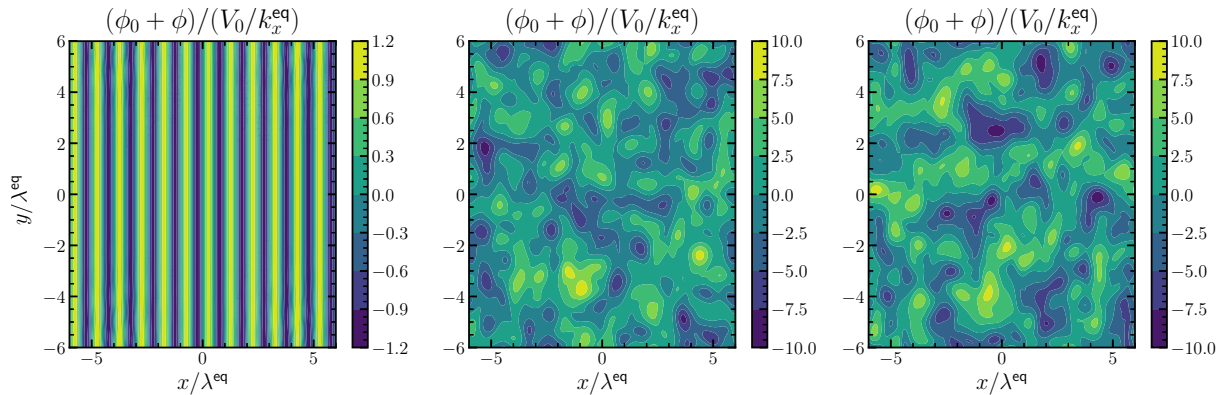


Figure 3.6 Contours of the full (equilibrium and fluctuation) electrostatic potential for a nonlinear simulation with $D_{\text{Krook}}/(k_x^{\text{eq}} V_0) = 1$ and $D_{\text{rad}}/(k_x^{\text{eq}} V_0) = 0.05$. From left to right, plots correspond to $t(k_x^{\text{eq}} V_0) \approx 46, 102$, and 501 . Comparing with Fig. 3.5 shows the system no longer tends towards large-scale coherent vortices with gradual decay of energy. Instead, multiple scales are excited and form a quasi-stationary state.

3.4.3 Momentum transport

We investigate the momentum transport driven by turbulent fluctuations in this system, examining the xy component of the Reynolds stress tensor, denoted as τ . From the average of the product of the x and y components of the fluctuating $E \times B$ flow in the homogeneous y direction,

$$\tau \equiv \left\langle -\frac{\partial \phi}{\partial x} \frac{\partial \phi}{\partial y} \right\rangle_y, \quad (3.11)$$

where $\langle A \rangle_q$ denotes an average of some quantity A over a domain in the variable q . Due to the sinusoidal variation in x of the equilibrium, τ changes sign along the x axis as the sign of the equilibrium flow changes, an expected feature of Kolmogorov flow (Musacchio & Boffetta 2014).

In nonlinear gyrokinetic simulations, numerical convergence is typically tested by measuring changes of some scalar, time-averaged transport quantity with numerical parameters such as resolution and domain size. Due to the changes in sign of τ , the average of τ in the x direction and time, $\langle \tau \rangle_{x,t}$, is not appropriate for testing numerical convergence because it is typically 0. Instead, we calculate the root-mean-square (RMS) of τ , i.e., $\sqrt{\langle \tau^2 \rangle_x}$, and compare the time-average in the quasi-stationary state as resolution changes. For the simulation shown in Fig. 3.6, the time-averaged τ_{RMS} in saturation changes by at most 2% when any spatial or velocity coordinate's domain size or resolution is doubled except L_x (expected due to the sub-

dominant unstable modes and inverse cascade), where it changes by 9%. Therefore, despite creating additional unstable and stable eigenmodes as box size is increased, this simulation is numerically converged in L_x with regards to τ_{RMS} .

Consistent with studies of Kolmogorov flow (where a constant force is typically used, while our forcing is proportional to $\tilde{f}(k_x^{\text{eq}}, 0)$) (Musacchio & Boffetta 2014), we find that as the forcing increases, both the mean flow velocity and the Reynolds stress increase, such that at saturation the two are in balance. This is shown in Fig. 3.7, where the force on the mean flow applied by D_{Krook} is seen to balance the force due to τ . This can also be seen by considering the effect of a similar Krook operator on Eq. (3.1). When

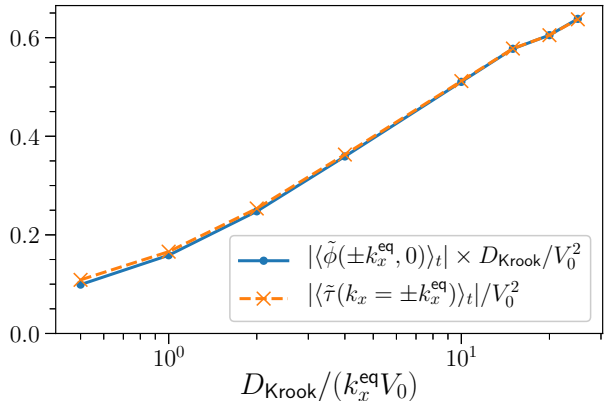


Figure 3.7 Comparison between average Krook drive amplitude $|\langle \tilde{\phi}(\pm k_x^{\text{eq}}, 0) \rangle_t| D_{\text{Krook}}$ and the average amplitude of the corresponding Fourier component of the Reynolds stress τ in saturation across a range of driving frequencies D_{Krook} . Other simulation parameters are the same as in Fig. 3.6. In the saturated state, the mean flow is governed by a competition between the external forcing and the turbulent Reynolds stress. A small contribution is made by the influence of dissipation on $\tilde{\phi}(\pm k_x^{\text{eq}}, 0)$, evidenced by the minor mismatch between the two curves at the lowest values of D_{Krook} .

Eq. (3.1) is Fourier transformed in both x and y , our forcing term appears as $D_{\text{Krook}}\delta_{k_x,\pm k_x^{\text{eq}}}\delta_{k_y,0}(k_x^2 + k_y^2)\tilde{\phi}$. The $(k_x, k_y) = (k_x^{\text{eq}}, 0)$ component of the equation then becomes

$$\begin{aligned} \frac{\partial}{\partial t}\tilde{\phi}(k_x^{\text{eq}}, 0) + \sum_{\mathbf{k}'} \frac{k'_y}{k_x^{\text{eq}}} [(k_x^{\text{eq}} - k'_x)^2 + k'^2] \tilde{\phi}(k'_x, k'_y) \tilde{\phi}(k_x^{\text{eq}} - k'_x, -k'_y) \\ = -D_{\text{Krook}}\tilde{\phi}(k_x^{\text{eq}}, 0), \quad (3.12) \end{aligned}$$

where the nonlinear term is the $k_x = k_x^{\text{eq}}$ component of the Fourier-transformed Reynolds stress $\tilde{\tau}$. For a quasi-stationary, saturated state, the time-average of Eq. (3.12) yields a balance between the Reynolds stress and the D_{Krook} term. Figure 3.7 compares these terms for a range of simulations with different values of D_{Krook} , demonstrating good agreement with expectations. A small mismatch occurs because the effect of dissipation on the flow makes a small contribution to the force balance, but the other forces are clearly dominant. Because we only include dissipation on the fluctuation, not the equilibrium ϕ_0 which is independent of D_{Krook} , this contribution decreases as D_{Krook} increases.

3.5 Eigenmode analysis

3.5.1 Eigenmode Expansion

We investigate the role of stable modes in this system by expanding the turbulent state in a basis of the eigenmodes of the dissipationless operator \mathcal{L}_{KH} . We expand in eigenmodes of the dissipationless operator to focus on the role played by f_2 , which, although it vanishes from the eigenmode spectrum in the dissipative system, may still characterize a component of the nonlinear state. This also allows for comparison with previous work (Fraser et al. 2017), where the dissipationless modes were considered.

As discussed in Sec. 3.3, the operator \mathcal{L}_{KH} has a distinct set of N_{ev} eigenmodes $\{\hat{f}_j\}$ for each value of k_y . Therefore, an expansion of an arbitrary state $f(s, x, y, v_{\parallel}, \mu)$ in a basis of eigenmodes \hat{f}_j may be written as

$$f(s, x, y, v_{\parallel}, \mu) = \sum_{k_y} \sum_{j=1}^{N_{\text{ev}}} \beta_j(k_y) \hat{f}_j(s, x, k_y, v_{\parallel}, \mu) e^{ik_y y}. \quad (3.13)$$

As in Sec. 3.3, the index j is a positive integer that enumerates the eigenmodes at a given k_y , and for $0 < k_y/k_x^{\text{eq}} < 1$, $j = 1$ and $j = 2$ label the most unstable mode and its stable conjugate, respectively. The number of eigenmodes N_{ev} obtained by the eigenmode solver is equal to the number of degrees of freedom in the discrete numerical representation, i.e., the product of the number of grid points and the number of species, and the modes were

verified to be linearly independent, so expansions of this form exist and are unique assuming the numerical resolutions of both sides of Eq. (3.13) are identical. Figure 3.8 shows time traces of $|\beta_1|$ in blue and $|\beta_2|$ in orange, as well as the time-averaged $|\beta_j|$ in saturation for every j at $k_y/k_x^{\text{eq}} = 0.25$ for the same simulation shown in Fig. 3.6.

The values β_j , which we refer to as the amplitudes of each eigenmode,

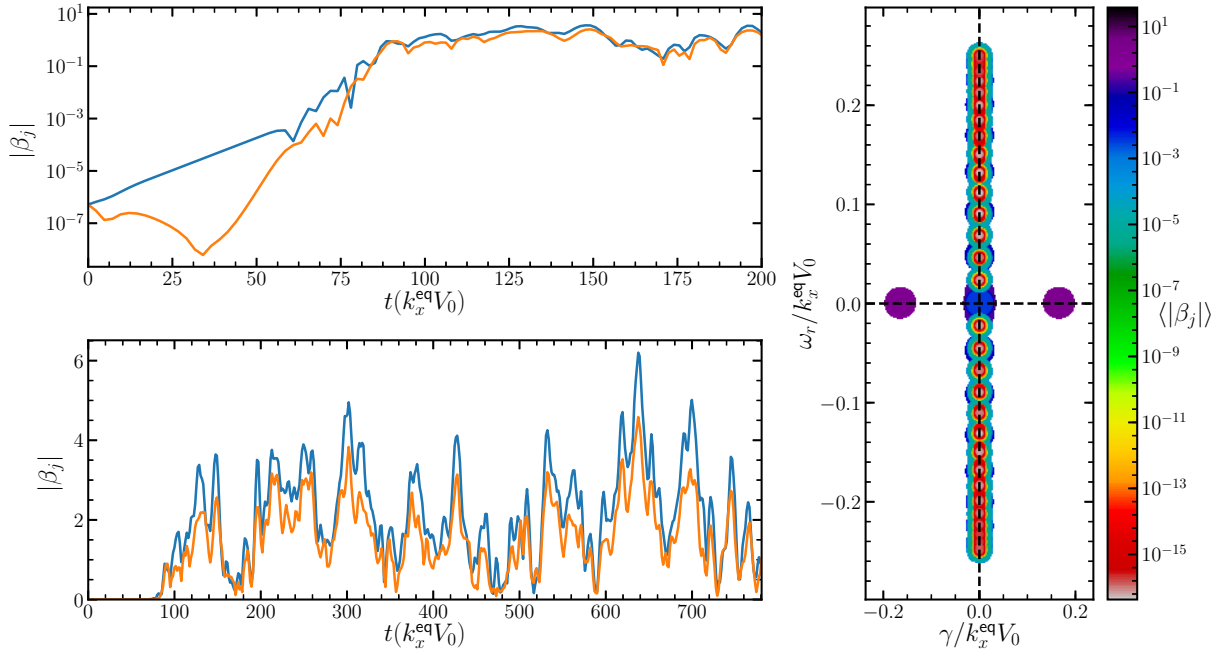


Figure 3.8 Left: Amplitudes of the unstable and stable eigenmodes, $|\beta_1|$ (blue) and $|\beta_2|$ (orange), respectively, as functions of time on a logarithmic scale (top, horizontal axis reduced to highlight the parametric growth of $|\beta_2|$) and a linear scale (bottom) at horizontal wavenumber $k_y/k_x^{\text{eq}} = 0.25$ for the simulation with $D_{\text{Krook}} = 1$, $D_{\text{rad}} = 0.05$, and $D_{\perp} = 1.6$. Right: Full spectrum of eigenvalues ω_j (real part ω_r on y -axis, growth rate γ on x -axis), with color indicating time-averaged (starting from $t = 300$) amplitudes $\langle |\beta_j| \rangle$, and dot size scaled proportionally to allow multiple $|\beta_j|$ with the same ω_j to be shown. The decay of β_2 is followed by nonlinear growth much faster than β_1 , while β_1 continues its linear growth, consistent with Fraser et al. (2017). The remarkable similarity of the values of $|\beta_1|$ and $|\beta_2|$ in the saturated state was predicted in Fraser et al. (2017). Results are qualitatively similar for other unstable k_y .

can be understood as coordinates or components of f in the basis $\{f_j\}$. When such an expansion is performed at multiple time steps of a given simulation so that f is a function of time, each β_j becomes a function of time that indicates the relative contribution of eigenmode f_j to the state of the system over time. In linear simulations, $\beta_j(k_y, t) = \beta_j(k_y, 0)e^{i\omega_j t}$ for each j and k_y . Previous work showed how β_1 and β_2 interact nonlinearly in a fluid system, derived equations for $\partial\beta_j/\partial t$ by inserting expansions of the form Eq. (3.13) into the governing equations of the system, and compared the relative sizes of different terms leading into instability saturation (Terry et al. 2006; Makwana et al. 2011; Fraser et al. 2017). Here we directly calculate the evolution of each β_j over time in nonlinear simulations, extending analysis beyond the onset of saturation. Our procedure for calculating each β_j relies on the left eigenmodes of \mathcal{L}_{KH} and is described in Terry et al. (2014); Hatch et al. (2011).

Similar analyses have been performed for gyroradius-scale instabilities in reduced fluid models (Makwana et al. 2011), and gyrokinetic models (Hatch et al. 2011; Pueschel et al. 2016). These eigenmode expansions are related to the “projections” calculated in related work (Whelan et al. 2018;

Pueschel et al. 2016; Faber et al. 2018), defined as

$$p_j = \left| \int d\mathbf{x}d\mathbf{v} \sum_s f_j^* f_{\text{NL}} \right| \left(\int d\mathbf{x}d\mathbf{v} \sum_s |f_j|^2 \int d\mathbf{x}d\mathbf{v} \sum_s |f_{\text{NL}}|^2 \right)^{-1/2} \quad (3.14)$$

(where f_{NL} is the nonlinearly-evolved distribution function, and the summations are over each species), but the two are generally quite different. Identifying $\langle g, h \rangle \equiv \int d\mathbf{x}d\mathbf{v} g^* h$ as an inner product on the space of distribution functions f , projections p_j are inner products normalized by the lengths of f_j and f so that $p_j = 0$ if they are orthogonal (under this inner product) and $p_j = 1$ if they are parallel. The eigenvectors of an arbitrary linear operator are not guaranteed to be mutually orthogonal under a given inner product (we have verified that the eigenmodes of our system are not mutually orthogonal under the above inner product), which leads to the possibility that the projection onto one eigenvector depends on the amplitudes of every eigenvector. For example, one could find that the projection p_j onto a stable mode counterintuitively grows over time in a linear simulation due to nonorthogonality, even though the amplitude β_j of the stable mode decays. Likewise, if the projection onto a stable mode is large in the saturated state, it is not immediately clear whether this is due to a large stable mode amplitude, significant nonorthogonality with the dominant unstable mode, or even due to nonorthogonality with an entirely different mode that has a large amplitude. This situation is avoided if the linear operator has mutually

orthogonal eigenvectors (e.g. if it is Hermitian), if the set of modes f_j are replaced by an orthogonal set, such as from a proper orthogonal decomposition (Hatch et al. 2011), or by applying an orthogonalization procedure like Gram-Schmidt (Pueschel et al. 2016). However, the relationship between the eigenmode amplitudes and the orthogonalized mode amplitudes is not immediately clear. We focus our attention on the eigenmode amplitudes β_j rather than projections p because linear energy transfer due to \mathcal{L}_{KH} is directly related to β_j , not p (Terry et al. 2006), and to facilitate comparison with Fraser et al. (2017).

For the simulation shown in Fig. 3.6, we use the parameters $L_x = 12\lambda^{\text{eq}}$, $D_{\text{Krook}} = 1$, $D_{\text{rad}} = 0.05$, and $D_{\perp} = 1.6$, with 512 grid points in the x direction. Calculating every eigenmode of the system at that resolution is prohibitively expensive. Instead, to generate Fig. 3.8 we perform eigenvalue computations with $L_x = \lambda^{\text{eq}}$. Due to the discrete, comb-like eigenmode structure in k_x discussed in Secs. 3.2.2 and 3.3.2, this reduced set of modes does not describe the full state of Eq. (3.13) because it lacks modes obtained when $L_x > \lambda^{\text{eq}}$ [see Fig. 3.2]. But this does allow for a full expansion of the components of $\tilde{f}(k_x, k_y)$ given by $k_x = nk_x^{\text{eq}}$ for integer n , and this does not affect the obtained values of β_1 and β_2 .

Consistent with analytical calculations and reduced models (Terry et al.

2006; Makwana et al. 2011; Fraser et al. 2017), Fig. 3.8 shows that $|\beta_2|$ decays before being nonlinearly driven at a rate faster than the unstable mode's concurrent exponential growth. We stress that the evolution of $|\beta_2|$ is remarkably consistent with the inviscid fluid problem (Fraser et al. 2017) despite the influence of nonzero D_\perp in the nonlinear simulation, which modifies the structure of f_1 and eliminates the conjugate stable mode f_2 from the eigenmode spectrum of the dissipative operator. A similar observation was made in studies of ITG pseudospectra, where a similar conjugate stable mode vanished in the dissipative case, but was nonetheless a part of the pseudospectrum and was significantly excited in saturation when dissipation was included (Hatch et al. 2016). Figure 3.8 only shows amplitudes for the $k_y/k_x^{\text{eq}} = 0.25$ eigenmodes, but every other k_y in $0 < k_y/k_x^{\text{eq}} < 1$ exhibits similar results. The amplitude of f_2 in saturation nearly matches that of f_1 both at saturation onset and for the rest of the simulation. Since the two modes are nearly conjugate symmetric, this suggests that the linear energy dissipation due to f_2 is a significant fraction of the linear energy injection due to f_1 at the onset of saturation and throughout the quasi-stationary state. This suggests that the predictive capabilities of the threshold parameter P_t analysis studied in Terry et al. (2006); Makwana et al. (2011) carry over to systems more general than plasma microturbulence, and that a significant

amount of the energy transferred to $k_y > 0$ fluctuations via \mathcal{L}_{KH} makes its way back into the mean flow rather than smaller scales.

3.5.2 Truncated eigenmode expansions

In turbulence models, it is common practice to separate the flow into mean and fluctuating parts. If there is further separation between large and small scale structures, the former are often approximated by the most unstable eigenmode (Gaster et al. 1985; Liou & Morris 1992; Nikitopoulos & Liu 2001). Here we demonstrate the potential for improving such models by including the stable mode in the approximation for the large scales.

Figure 3.9 compares part of the flow structure at $t \approx 501(V_0 k_x^{\text{eq}})^{-1}$ to three different expansions. The top-left contours show the electrostatic potential ϕ for the simulation described in Fig. 3.8. To focus on the components of ϕ where the eigenmodes discussed in Figs. 3.1 and 3.2 can be used to approximate the flow, a filtering procedure has been applied in Fig. 3.9 to remove all but a subset of Fourier components (k_x, k_y) . Only k_y in $0 < k_y/k_x^{\text{eq}} < 1$ are included, and only $k_x = nk_x^{\text{eq}}$ for integer n are included. This allows the eigenmodes in Fig. 3.8, and the equivalent eigenmodes at other unstable k_y , to be used as a basis in the sense of Eq. (3.13). The top-right contours show the ϕ structure obtained from summing over these eigenmodes at each unstable k_y , verifying that they indeed serve as a basis.

The excellent agreement helps demonstrate that the wavenumber filtering only affects the amplitudes β_j of eigenmodes that arise from having $L_x > \lambda^{\text{eq}}$, and fully captures the structure and amplitudes of the $L_x = \lambda^{\text{eq}}$ eigenmodes. Extremely minor differences between the top-left and top-right contours arise due to the higher x resolution in the nonlinear simulation than in

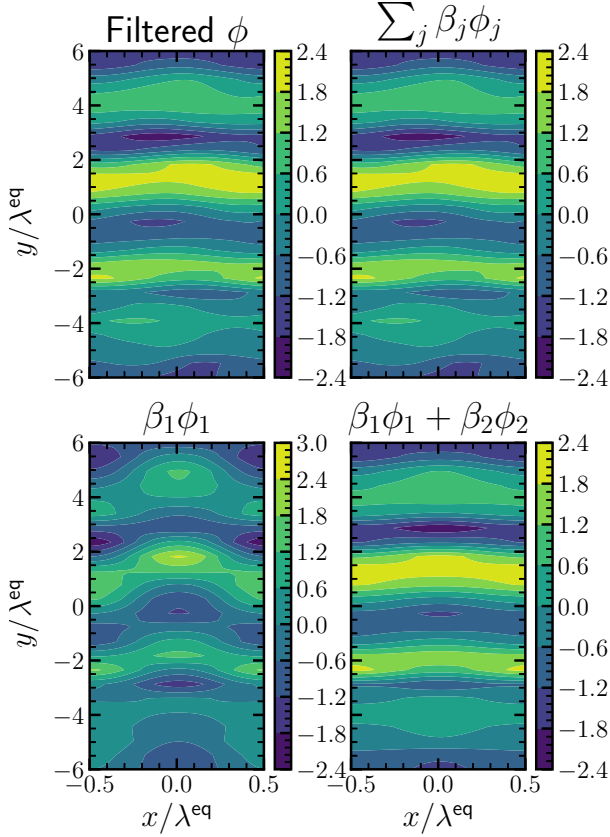


Figure 3.9 Comparison between the components of ϕ that are spanned by the eigenmodes in Fig. 3.8 (top left), a summation over all of the eigenmodes in Fig. 3.8 at every unstable k_y (top right), summation over just the most unstable mode at every unstable k_y (bottom left), and summation over the most unstable and conjugate stable mode at every unstable k_y (bottom right) at $t \approx 501(V_0 k_x^{\text{eq}})^{-1}$ for the same simulation as Fig. 3.6. Due to only integer multiples of k_x^{eq} contributing to these eigenmodes, they are unable to effectively reproduce the full flow profile, plotted in Fig. 3.6. However, those components of ϕ that can be expressed as a linear combination of the eigenmodes in Fig. 3.8 are very well-described even by just the unstable ϕ_1 and stable ϕ_2 .

the linear eigenmode calculations. To investigate the differences between these large-scale flows and the results of approximating them using just the unstable mode, the bottom-left contours show the result of excluding every eigenmode in Eq. (3.13) except the most unstable at each k_y , as is often done in reduced models. The bottom-right contours are obtained similarly, but both the most unstable mode ϕ_1 and the conjugate stable mode ϕ_2 at each k_y are included. Including ϕ_2 produces a flow structure that is remarkably similar to the top-left and top-right flow structures, unlike what one obtains when only ϕ_1 is included. Unsurprisingly, the more accurate flow structure leads to a more accurate Reynolds stress (not shown).

To compare the efficacy of these three eigenmode expansions over time,

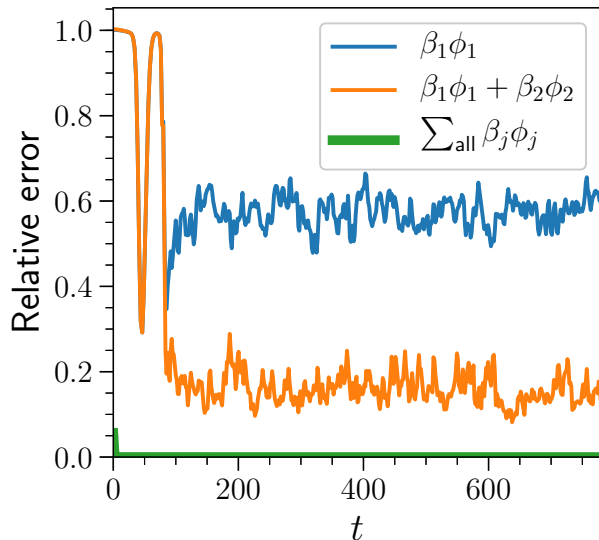


Figure 3.10 Error in ϕ of each of the eigenmode expansions of Fig. 3.9 relative to the filtered nonlinear data. Including ϕ_2 significantly improves fluctuation estimates in the quasi-stationary state.

rather than the one timestep shown in Fig. 3.9, we calculate the error, given by $\|\phi - \sum_j \beta_j \phi_j\| / \|\phi\|$, of each relative to the filtered nonlinear data (the top-left plot in Fig. 3.9). Here ϕ refers to the filtered nonlinear ϕ , and $\|\cdot\|$ is the standard L_2 norm. Due to differences in x resolution, the full expansion (in green) has minor errors that decay away as the simulation progresses. Errors in both the unstable-only expansion (blue) and the combined unstable-stable expansion (orange) start large due to choice of initial condition, gradually decay as the most unstable mode grows in the linear phase, and peak at the onset of saturation before fluctuating about an average value in the quasi-stationary state, with the inclusion of the stable mode reducing the average error in the saturated state by a factor of three.

3.5.3 Influence of forcing and dissipation

Figure 3.8 shows significant excitation of the stable mode in the saturated state for a simulation with $D_{\text{Krook}} = 1$, $D_{\text{rad}} = 0.05$, and $D_{\perp} = 1.6$, with Figs. 3.9 and 3.10 demonstrating its importance in describing the large-scale fluctuations in ϕ . To investigate the role of these parameters in determining the influence of stable modes in saturation, we vary them between different simulations. In particular, we pay close attention to the relative amplitudes of β_1 and β_2 as D_{rad} and D_{Krook} are varied. Because D_{rad} is a symmetry-breaking term in the sense that it decreases the growth rate of

f_1 and increases the damping of f_2 without changing their mode structures, it reduces the parametric driving of f_2 by f_1 . (The parametric driving of f_2 by f_1 depends on their mode structures, the form of the nonlinearity, and γ_2/γ_1 (Terry et al. 2006, 2009; Makwana et al. 2011; Fraser et al. 2017). Of those, only γ_2/γ_1 is affected by D_{rad} , making its influence on $|\beta_1/\beta_2|$ more transparent.) Figure 3.11 shows that this leads to significantly smaller $|\beta_2|$ relative to $|\beta_1|$ in the saturated state. This also suggests that for unstable shear flow in systems without radiative damping $|\beta_2| \approx |\beta_1|$ is expected, consistent with Fraser et al. (2017). The k_y dependence of the ratio $|\beta_1/\beta_2|$ roughly follows that of γ_1 , except that it approaches 1, rather than 0, at

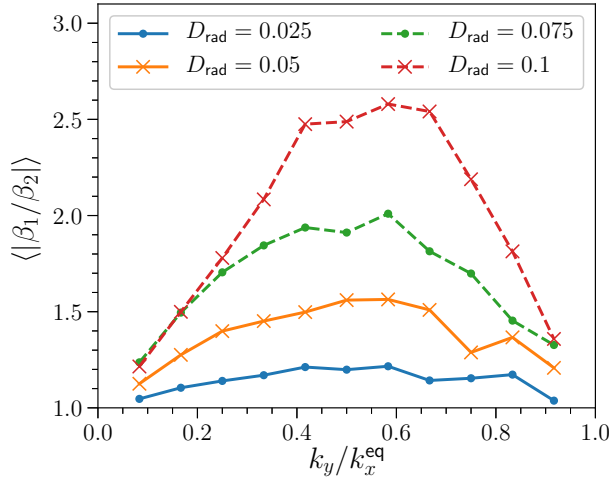


Figure 3.11 Time-averaged ratio of unstable mode amplitude to stable mode amplitude in saturation at each k_y for a range of D_{rad} with $D_{\text{Krook}} = 1$. The growth rate dependence of the P_t analysis (Terry et al. 2006, 2009; Makwana et al. 2011) suggests that higher D_{rad} causes β_2 to be driven less leading into saturation. Here we see that this is reflected in the eigenmode amplitudes in the saturated state. The k_y dependence of the ratio $|\beta_1/\beta_2|$ roughly follows that of γ_1 .

$k_y = 0$ and $k_y = k_x^{\text{eq}}$.

Figure 3.12 shows how the time-averaged large-scale values of $|\beta_2/\beta_2|$ in saturation vary with D_{Krook} . The shape of the curves remains fairly consistent as D_{Krook} changes. Two regimes are apparent: below $D_{\text{Krook}} = 4$, increasing D_{Krook} drives the ratio $|\beta_1/\beta_2|$ closer to unity, while above $D_{\text{Krook}} = 4$ the ratio is significantly less affected. This behavior is consistent with the notion that reinforcement of the unstable profile by larger D_{Krook} allows β_2 to be nonlinearly pumped to its maximal level, whereas for smaller D_{Krook} the quasilinear depletion of the profile cuts off the pumping of β_2 before it reaches its maximal level. Note that f_2 tends to reduce the Reynolds stress τ , suggesting that the increase in τ with D_{Krook} must be due

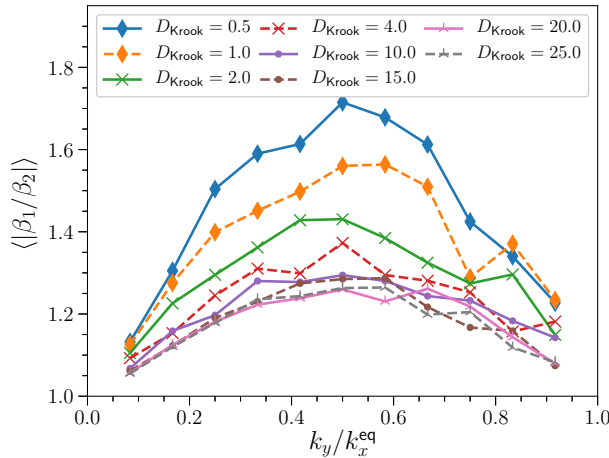


Figure 3.12 Time-averaged ratio of unstable to stable mode amplitude in saturation at each k_y for a range of D_{Krook} . Between $D_{\text{Krook}} = 0.5$ and 4, increasing D_{Krook} generally pushes the ratio of amplitudes closer to unity. Above $D_{\text{Krook}} = 4$, increasing D_{Krook} has a less pronounced impact on the ratio. We stress that, in both regimes, the mean flow amplitude and Reynolds stress increase with D_{Krook} .

to an increase in overall fluctuation level, rather than a change in $|\beta_1/\beta_2|$.

3.5.4 Influence of stable modes in analytical models

To better understand how the unstable and stable modes affect the mean flow in saturation, we develop a reduced model that expresses the mean flow amplitude in terms of β_1 and β_2 . The model considers a 2D inviscid, incompressible fluid, assumes $\phi \approx \beta_1\phi_1 + \beta_2\phi_2$ for $0 < k_y/k_x^{\text{eq}} < 1$, and assumes that the force applied by the Krook operator balances the turbulent Reynolds stress in saturation. These assumptions are consistent with the findings presented in Figs. 3.7 and 3.9.

For perturbations about a sinusoidal equilibrium flow, the linearized system becomes Eq. (3.4), which was derived in Sec. 3.2 but is repeated here:

$$\omega_j(k_x^2 + k_y^2)\tilde{\phi}_j + \frac{k_y V_0}{2} \left[(k_x^2 - 2k_x k_x^{\text{eq}} + k_y^2)\tilde{\phi}_j^- + (k_x^2 + 2k_x k_x^{\text{eq}} + k_y^2)\tilde{\phi}_j^+ \right] = 0.$$

Equation (3.4) can be expressed as a matrix equation $\omega_j \vec{\phi}_j + \mathbf{M} \vec{\phi}_j = 0$ where the components of $\vec{\phi}_j$ are $\tilde{\phi}_j$ at different k_x and the dimension of $\vec{\phi}_j$ and \mathbf{M} is infinite. Reasonable approximations of the eigenmodes and eigenvalues can be obtained by solving the matrix equation with $\tilde{\phi}_j \neq 0$ for some finite number of k_x values, and $\tilde{\phi}_j = 0$ for all other k_x . This has previously been found useful in similar KH and tearing mode calculations (Pessah 2010).

For example, solving the system with $k_x = 0, \pm k_x^{\text{eq}}$ yields

$$\begin{aligned}\omega_1 &= -\frac{ik_y V_0}{\kappa} & \vec{\phi}_1 &= (1, -i\kappa, 1)^T \\ \omega_2 &= \frac{ik_y V_0}{\kappa} & \vec{\phi}_2 &= (1, i\kappa, 1)^T \\ \omega_3 &= 0 & \vec{\phi}_3 &= (-1, 0, 1)^T,\end{aligned}$$

where the vectors are written in the form $(\tilde{\phi}(-k_x^{\text{eq}}), \tilde{\phi}(0), \tilde{\phi}(k_x^{\text{eq}}))^T$ and

$$\kappa(k_y) \equiv \sqrt{2((k_x^{\text{eq}})^2 + k_y^2)/((k_x^{\text{eq}})^2 - k_y^2)}.$$

To arrive at an expression of force balance between the Reynolds stress and Krook drive, we return to Eq. (3.12), which we repeat here:

$$\begin{aligned}\frac{\partial}{\partial t} \tilde{\phi}(k_x^{\text{eq}}, 0) + \sum_{\mathbf{k}'} \frac{k'_y}{k_x^{\text{eq}}} ((k_x^{\text{eq}} - k'_x)^2 + k'^2_y) \tilde{\phi}(k'_x, k'_y) \tilde{\phi}(k_x^{\text{eq}} - k'_x, -k'_y) \\ = -D_{\text{Krook}} \tilde{\phi}(k_x^{\text{eq}}, 0).\end{aligned}$$

Considering a steady state where $\partial \tilde{\phi}(k_x^{\text{eq}}, 0) / \partial t = 0$, and assuming $\tilde{\phi} = \beta_1 \tilde{\phi}_1 + \beta_2 \tilde{\phi}_2$ with just the $k_x = 0, \pm k_x^{\text{eq}}$ Fourier modes considered, Eq. (3.12) can be manipulated to yield

$$\tilde{\phi}(k_x^{\text{eq}}, 0) = \frac{2ik_x^{\text{eq}}}{D_{\text{Krook}}} \sum_{k'_y > 0} k'_y \kappa(k'_y) (|\beta_1|^2 - |\beta_2|^2). \quad (3.15)$$

From here, values for $|\beta_1|$ and $|\beta_2|$ can be inserted to arrive at values for the mean flow amplitude. In other systems, $|\beta_j|$ have been calculated using statistical closures (Baver et al. 2002; Terry & Gatto 2006; Hegna et al. 2018). Extending the above approach with such a calculation would

yield a complete model, but is outside the scope of this paper. Instead, we insert values of $|\beta_1|$ and $|\beta_2|$ from nonlinear simulations into Eq. (3.15). Our interest is in the scaling of $\tilde{\phi}(k_x^{\text{eq}}, 0)$ with D_{Krook} , and what role β_2 plays in that scaling. Thus, we perform simulations with a range of D_{Krook} and compare three quantities: the time-averaged value of $\tilde{\phi}(k_x^{\text{eq}}, 0)$ in saturation, the result of Eq. (3.15) using both β_1 and β_2 , and the result obtained when $\beta_2 = 0$ is assumed. In Fig. 3.13, this comparison is made for three values of D_{rad} , corresponding to three systems with varying degrees of stable mode excitation (recall stable modes are more excited at lower values of D_{rad} , see

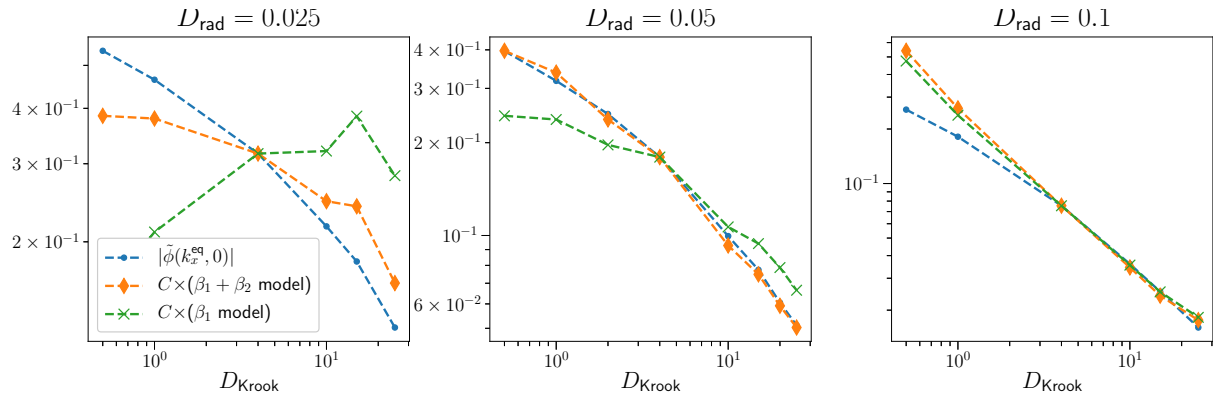


Figure 3.13 A comparison between the true value of $|\phi(k_x^{\text{eq}}, 0)|$ (blue dots) and values predicted by Eq. (3.15) with (orange diamonds) and without (green crosses) the stable mode contribution β_2 included over multiple values of D_{Krook} and D_{rad} . In each frame, the models are scaled by a constant coefficient to match the true value at $D_{\text{Krook}} = 4$ so that the scaling with D_{Krook} can be investigated, rather than the absolute agreement. For the base case $D_{\text{rad}} = 0.05$ (center frame), the scaling of $|\phi(k_x^{\text{eq}}, 0)|$ with D_{Krook} is qualitatively captured by the model with β_2 neglected, however the scaling is significantly improved when stable modes are included. For the larger value of D_{rad} (right frame), where stable modes are largely suppressed in saturation (c.f. Fig. 3.11), including β_2 in the model produces little change, and decent quantitative agreement is observed by the model both with and without β_2 included. For the smaller value of D_{rad} (left frame), where stable modes are more important, the model fails to even qualitatively agree with simulations unless β_2 is included, in which case the overall trend is captured.

Fig. 3.11). For $D_{\text{rad}} = 0.05$, where stable modes were shown in Fig. 3.8 to be significant, the $\beta_2 = 0$ model captures general trends, but is significantly improved when β_2 is properly included. For $D_{\text{rad}} = 0.025$, where stable modes are even more important, the $\beta_2 = 0$ model fails to even capture the decrease in $|\tilde{\phi}(k_x^{\text{eq}}, 0)|$ with D_{Krook} , while the model that includes β_2 does capture the correct qualitative and often even quantitative behavior. At $D_{\text{rad}} = 0.1$, where stable modes are significantly weakened, their inclusion does not have a significant impact on the model. For each value of D_{rad} , the two models are scaled by a constant so that they agree with the simulation results at $D_{\text{Krook}} = 4$, which is where the change in scaling with respect to D_{Krook} was noted in Fig. 3.12. (It is the scaling properties of the models that we are assessing, not the absolute values.) Note that this model neglects all eigenmodes except ϕ_1 and ϕ_2 , including the modes with nonzero k_x at noninteger multiples of k_x^{eq} .

Comparing the two models at different values of D_{rad} demonstrates that when stable modes are excited in this system as in Fig. 3.8, they not only modify the shape of the flow, as shown in Fig. 3.9, but have an important impact on how the system responds to forcing. By nonlinearly transferring energy into large-scale stable modes, the fluctuating flow adjusts in a way that changes the feedback onto the large-scale mean flow, thus affecting how

the system is forced. We also note that Eq. (3.15) was derived assuming an inviscid fluid, while the inserted values for $|\beta_1|$ and $|\beta_2|$ were obtained from gyrokinetic simulations with finite D_\perp , suggesting gyrokinetic effects may not play a significant role in the eigenmode excitations and force balance in this system.

3.6 Conclusions

We have studied an unstable gyrokinetic shear flow, finding that a conjugate stable eigenmode is nonlinearly driven to a large amplitude leading into saturation, and continues to make important contributions to the Reynolds stress in the quasi-stationary turbulent state, except at high values of radiative damping. This demonstrates that previous findings on the role of stable eigenmodes in shear-flow instability saturation of a fluid shear layer are consistent with the quasi-stationary turbulent state of a gyrokinetic periodic shear flow. Furthermore, our results point to the potential for significantly improving reduced models of shear-driven turbulence by including stable-mode physics.

We have investigated the saturation of a linearly unstable $E \times B$ shear flow in gyrokinetics as it relates to the full eigenmode spectrum. We find that the gyrokinetic system compares well with its hydrodynamic counterpart with regards to the unstable mode, as well as the rest of the spectrum.

Specifically, the dissipationless linear operator includes a single conjugate stable eigenmode for every unstable eigenmode, along with a continuum of marginally stable modes. Nonlinear simulations characterize the behavior of the flow in saturation, and we examine cases both with and without an external driving term. The drive is implemented in the form of a Krook operator, and reinforces the unstable mean flow in a manner similar to Kolmogorov flow.

In simulations without the drive term, the system lacks any energy injection to maintain the unstable equilibrium. This causes fluctuations to quickly relax the unstable flow shear once nonlinear interactions become significant, and the turbulence subsequently decays. In simulations with forcing, we include a scale-independent radiative damping term that prevents accumulation of energy at the largest scales, and allows a quasi-stationary state of driven turbulence. In driven simulations, a partial relaxation of the mean flow is still observed, with the final state mostly determined by a force balance between the Krook drive and the turbulent Reynolds stress.

With a well-resolved system of quasi-stationary, driven turbulence, we investigate the role of different linear eigenmodes by performing an eigenvalue decomposition, where the turbulent state is expressed as a linear combination of the eigenmodes of the dissipationless linear operator. The

evolution of the dominant pair of stable and unstable modes leading into saturation compares well with previous analytic calculations of an inviscid fluid shear layer (Fraser et al. 2017), and the ensuing excitation of the stable mode in the turbulent state is consistent with previous findings in plasma microturbulence (Makwana et al. 2011). By demonstrating that the role of stable modes in shear-flow instability saturation is consistent with their role in the fully-developed turbulent system, we have extended the set of systems in which instability saturation analyses has proven to be predictive of the turbulent state to include fully global fluid instabilities, further motivating these sorts of analyses in other global instabilities where stable modes exist, such as the magnetorotational instability (Clark 2017).

The significant excitation of linearly stable modes in the saturated state indicates that an important aspect of shear-driven turbulence is this previously-neglected tendency for large-scale fluctuations to lose energy back into the mean flow via the linear operator. This idea is in contrast with the standard picture of instability-driven turbulence, where it is assumed that the largest scales are dominated by a balance between linear energy injection and nonlinearly energy transfer to smaller scales. While many other modes are also excited in the saturated state, we have shown that the stable/unstable pair of modes is sufficient to capture many aspects

of the flow. This also presents a significant modification to the existing understanding of shear-driven turbulence, where reduced models generally assume that large-scale fluctuations are dominated by unstable modes alone (Gaster et al. 1985; Liou & Morris 1992; Nikitopoulos & Liu 2001; Horton et al. 1987).

Consistent with previous work where the conjugate symmetry between unstable/stable pairs of modes was broken with dissipative terms (Terry et al. 2009), we find that the added radiative damping term, which increases the damping rate of the stable mode and reduces the growth rate of the unstable mode, suppresses the importance of the stable mode relative to the unstable one. This is observed by comparing the amplitudes of the two modes for a range of radiative damping values. Making use of the observations that the gyrokinetic and fluid systems behave similarly, that the mean flow amplitude at saturation is determined by force balance between driving and Reynolds stress, and that the stable and unstable modes alone describe large-scale fluctuations well despite the conjugate stable mode vanishing from the eigenmode spectrum when dissipation is included, we construct a reduced model that allows us to examine the role of stable modes in determining the mean flow in saturation. The model results in an equation where the contributions from stable modes can be isolated from

unstable modes. We find that lower values of radiative damping, where stable modes exhibit higher amplitudes, require the inclusion of stable modes in the model in order for it to be even qualitatively correct. At higher radiative damping, where stable modes are suppressed, their inclusion in the model has no significant impact on its performance. Thus, in shear-flow systems where stable modes play an important role in instability saturation, they may also be expected to play an important role in understanding how fluctuations affect the mean flow, and thus how the system responds to external forcing. We further conclude that when effects observed to change turbulence characteristics also break the conjugate symmetry of an unstable/stable eigenmode pair (Palotti et al. 2008), the change in turbulence may be related to differences in stable mode excitation.

The authors would like to thank B.N. Rogers, W. Dorland, M.E. Pesah, and F. Waleffe for valuable discussions and insights. Partial support for this work was provided by the National Science Foundation under Award PHY-1707236, the Wisconsin Alumni Research Foundation, the Vilas Trust, and the U S Department of Energy, Office of Science, Fusion Energy Sciences, under Award No. DE-FG02-89ER53291. Computing resources were provided by the National Science Foundation through XSEDE computing

resources, allocation No. TG-PHY130027.

References

- Balbus, S. A., & Hawley, J. F. 1998, *Reviews of Modern Physics*, 70, 1
- Bauer, D. A., Terry, P. W., Gatto, R., & Fernandez, E. 2002, *Physics of Plasmas*, 9, 3318
- Brandst  ter, A., Swift, J., Swinney, H. L., et al. 1983, *Phys. Rev. Lett.*, 51, 1814
- Brizard, A. J., & Hahm, T. S. 2007, *Reviews of Modern Physics*, 79, 421
- Burns, K. J., Vasil, G. M., Oishi, J. S., Lecoanet, D., & Brown, B. P. 2020, *Physical Review Research*, 2, 23068
- Case, K. M. 1960, *Physics of Fluids*, 3, 143
- Chandrasekhar, S. 1961, *Hydrodynamic and Hydromagnetic Stability* (Oxford University Press)
- Clark, S. E. 2017, PhD thesis, Columbia University
- Drazin, P. G., & Reid, W. 1981, *Hydrodynamic Stability* (Cambridge University Press)
- Faber, B. J., Pueschel, M. J., Terry, P. W., Hegna, C. C., & Roman, J. E. 2018, *Journal of Plasma Physics*, 84, 905840503
- Faganello, M., & Califano, F. 2017, *Journal of Plasma Physics*, 83, 535830601
- Fraser, A. E., Terry, P. W., Zweibel, E. G., & Pueschel, M. J. 2017, *Physics of Plasmas*, 24, 062304
- Gaster, M., Kit, E., & Wygnanski, I. 1985, *Journal of Fluid Mechanics*, 150, 23–39
- Goodman, J., & Xu, G. 1994, *The Astrophysical Journal*, 432, 213
- Hatch, D. R., Jenko, F., Navarro, A. B., et al. 2016, *New Journal of Physics*, 18, 075018

- Hatch, D. R., Terry, P. W., Jenko, F., et al. 2011, Physics of Plasmas, 18, 055706
- Hegna, C. C., Terry, P. W., & Faber, B. J. 2018, Physics of Plasmas, 25, 022511
- Henri, P., Cerri, S. S., Califano, F., et al. 2013, Physics of Plasmas, 20, 102118
- Horton, W., Tajima, T., & Kamimura, T. 1987, Physics of Fluids, 30, 3485
- Jenko, F., Dorland, W., Kotschenreuther, M., & Rogers, B. N. 2000, Physics of Plasmas, 7, 1904
- Kammerer, M., Merz, F., & Jenko, F. 2008, Physics of Plasmas, 15, 052102
- Kim, J. H., & Terry, P. W. 2010, Physics of Plasmas, 17, 112306
- Latter, H. N., Fromang, S., & Gressel, O. 2010, Monthly Notices of the Royal Astronomical Society, 406, 848
- Latter, H. N., Lesaffre, P., & Balbus, S. A. 2009, Monthly Notices of the Royal Astronomical Society, 394, 715
- Liou, W. W., & Morris, P. J. 1992, Physics of Fluids A, 4, 2798
- Longaretti, P. Y., & Lesur, G. 2010, Astronomy and Astrophysics, 516, 51
- Lucas, D., & Kerswell, R. 2014, Journal of Fluid Mechanics, 750, 518
- Makwana, K. D., Terry, P. W., Kim, J.-H. H., & Hatch, D. R. 2011, Physics of Plasmas, 18, 012302
- Marston, J. B., Conover, E., & Schneider, T. 2008, Journal of the Atmospheric Sciences, 65, 1955
- Merz, F. 2009, PhD thesis, University of Münster
- Musacchio, S., & Boffetta, G. 2014, Physical Review E, 89, 023004
- Nikitopoulos, D. E., & Liu, J. T. 2001, Physics of Fluids, 13, 966
- Palotti, M. L., Heitsch, F., Zweibel, E. G., & Huang, Y. 2008, The Astrophysical Journal, 678, 234–244
- Pessah, M. E. 2010, The Astrophysical Journal, 716, 1012

- Pessah, M. E., & Goodman, J. 2009, *The Astrophysical Journal*, 698, L72
- Platt, N., Sirovich, L., & Fitzmaurice, N. 1991, *Physics of Fluids A*, 3, 681
- Pueschel, M. J., Dannert, T., & Jenko, F. 2010, *Computer Physics Communications*, 181, 1428
- Pueschel, M. J., Faber, B. J., Citrin, J., et al. 2016, *Physical Review Letters*, 116, 085001
- Pueschel, M. J., Hatch, D. R., Görler, T., et al. 2013, *Physics of Plasmas*, 20, 102301
- Pueschel, M. J., Jenko, F., Told, D., & Büchner, J. 2011, in *Physics of Plasmas*, Vol. 18, 112102
- Pueschel, M. J., Told, D., Terry, P. W., et al. 2014, *The Astrophysical Journal Supplement Series*, 213, 30
- Reynolds-Barredo, J. M., Newman, D. E., Terry, P. W., & Sanchez, R. 2016, *Europhysics Letters*, 115, 34002
- Rogers, B. N., & Dorland, W. 2005, *Physics of Plasmas*, 12, 062511
- Rogers, B. N., Dorland, W., & Kotschenreuther, M. 2000, *Phys. Rev. Lett.*, 85, 5336
- Squire, J., Quataert, E., & Kunz, M. W. 2017, *Journal of Plasma Physics*, 83, 905830613
- Terry, P. W., Baver, D. A., & Gupta, S. 2006, *Physics of Plasmas*, 13, 022307
- Terry, P. W., Baver, D. A., & Hatch, D. R. 2009, *Physics of Plasmas*, 16, 122305
- Terry, P. W., Faber, B. J., Hegna, C. C., et al. 2018, *Physics of Plasmas*, 25, 012308
- Terry, P. W., & Gatto, R. 2006, *Physics of Plasmas*, 13, 062309
- Terry, P. W., Makwana, K. D., Pueschel, M. J., et al. 2014, *Physics of Plasmas*, 21, 122303
- Tobias, S. M., Dagon, K., & Marston, J. B. 2011, *The Astrophysical Journal*, 727, 127

Vanon, R., & Ogilvie, G. I. 2016, Monthly Notices of the Royal Astronomical Society, 463, 3725

Waleffe, F. 1995, Physics of Fluids, 7, 3060

Whelan, G. G., Pueschel, M. J., & Terry, P. W. 2018, Phys. Rev. Lett., 120, 175002

Chapter 4

Suppression of stable mode effects by magnetic fields in free shear layers in MHD

*This chapter is under preparation for
eventual submission to Physics of Plasmas*

Abstract

An unstable shear layer with an initially-uniform, flow-aligned magnetic field is studied in the regime of 2D incompressible magnetohydrodynamics with finite resistivity and viscosity using direct numerical simulations. The layer evolves freely without external forcing, broadening in time as turbulent stresses transport momentum across it. As with the system studied in Chapter 3, here a conjugate stable mode exists for every unstable mode in the absence of dissipation. Stable modes are shown to transport momentum up its gradient and shrink the layer when dominant. When the magnetic field is weak, the linear instability is minimally affected by it, but enhanced small-scale fluctuations relative to the hydrodynamic case are observed. These fluctuations coincide with increased dissipation and faster layer broadening, and are more pronounced with stronger fields. Here, these effects are understood as consequences of a reduction in stable mode excitation with stronger fields. As field strength increases, stable modes become less excited and transport less momentum against its gradient. Additionally, the energy these modes would otherwise transfer to the driving shear instead cascades to small scales where it is lost to dissipation. Reduced models akin to Chapter 3 are explored. While the Reynolds stress is well-described using just two modes per wavenumber, the Maxwell stress is not.

4.1 Introduction

Chapters 2 and 3 established that – in basic systems of shear flow instability – large-scale, dissipationless stable modes are nonlinearly coupled to unstable modes. While unstable modes tend to transport momentum down its gradient, stable modes tend to transport momentum against its gradient. Coupling to stable modes was shown to play a significant role in instability saturation relative to other energy transfer channels. Due to this coupling, stable modes reach significant amplitudes relative to unstable modes in the ensuing turbulence, except when an added dissipation that preferentially affects large scales is strong. When stable modes reach such large amplitudes, large-scale flow fluctuations are well-approximated by a combination of stable and unstable modes alone (one pair per horizontal wavenumber), and accounting for stable modes significantly improves reduced models of momentum transport.

In this chapter, stable modes are investigated for an unstable shear layer that is more complex than the shear flows in previous chapters in two key regards. First, the fluid is electrically conducting (e.g. a plasma) and modeled in the framework of magnetohydrodynamics (MHD), with an initially uniform magnetic field along the direction of flow in the equilibrium.

Second, the base flow is not held fixed as in Chapter 2, nor reinforced as in Chapter 3; thus, the flow gradient gradually flattens as turbulent stresses broaden the layer. This introduces a third instability saturation mechanism in addition to the two considered in Chapter 2, and complicates the methods that were employed in Chapter 3 to analyze the effects of stable modes.

Previous studies of this system (e.g. Palotti et al. 2008; Mak et al. 2017) have shown that the addition of an equilibrium magnetic field enhances the turbulent momentum transport and broadening rate of the layer. Because the magnetic field is known to reduce the growth rate of the driving instability (Chandrasekhar 1961; Palotti et al. 2008), reduced transport models primarily informed by the growth rate of the instability are unlikely to capture this scaling. Here, the effect of this field on stable mode excitation is investigated to identify whether the enhanced transport is attributable to a suppression of stable modes and the counter-gradient transport that they provide. If so, the effect of the magnetic field might be compared to the added damping in Chapter 3.

The system is studied by analyzing 2D, incompressible MHD simulations with finite resistivity and viscosity computed with the Dedalus code (Burns et al. 2020), previously used to study a similar hydrodynamic system (Lecoanet et al. 2016). Some hydrodynamic simulations are also performed

for comparison. In the MHD case, the field strength and resistivity are varied to explore different regimes of magnetic activity, focusing more on the weak-field regime than the strong-field regime for its closer correspondence to the familiar hydrodynamic case. The initially-uniform field is wound up by large-scale vortices formed by the instability in a manner consistent with Mak et al. (2017). With this winding of the field, small-scale magnetic fluctuations are observed along with potential reconnection events. The Maxwell stress associated with these fluctuations enhances transport and layer broadening by an amount that increases with field strength (within the weak-field regime explored here). Additionally, the magnetic fluctuations greatly enhance the overall energy dissipation rate due to resistive dissipation, which exceeds viscous dissipation for all but the weakest magnetic fields considered. These fluctuations are also accompanied by some enhanced small-scale flow fluctuations that increase viscous dissipation relative to the hydrodynamic case unless the field is sufficiently weak, with the threshold determined by both initial field strength and resistivity.

Previously observed phases where the layer's width briefly shrinks (Ho & Huerre 1984) due to counter-gradient momentum transport are observed in simulations with a weak or no magnetic field, but not with a sufficiently strong magnetic field. Consistent with hydrodynamic experiments reviewed

by Ho & Huerre (1984), this counter-gradient transport is driven by reversals of the Reynolds stress induced by large-scale flow fluctuations. The reduction in counter-gradient transport with stronger fields is shown to have two causes. First, the Maxwell stress due to small-scale field fluctuations becomes stronger. The Maxwell stress always transports momentum down the gradient and thus opposes any Reynolds-stress-induced counter-gradient transport. Second, the Reynolds stress is reduced at stronger fields, with a greater reduction during counter-gradient transport phases than at other times.

Reversals in the Reynolds stress have previously been shown to be an indication of stable mode activity in hydrodynamic systems (Fraser et al. 2017). This is shown to be the case in this system as well. This allows the Reynolds stress to serve as a convenient proxy for relative amplitudes between stable and unstable modes, so that trends in stable mode activity as field strength varies can be identified with simple Reynolds stress analyses. Using this proxy, the enhanced generation of small-scale fluctuations and corresponding dissipation as field strength increases is attributed to a partial suppression of stable modes. This connection between more energy transfer to small scales and reduced stable mode activity is consistent with other systems, where stable modes are known to remove energy from large-

scale fluctuations that would otherwise cascade to small scales (Makwana et al. 2014). Thus, reduction in counter-gradient momentum transport by Reynolds stresses is shown to be directly caused by less stable mode activity with stronger fields, which indirectly enhances small-scale fluctuations, dissipation, and down-gradient momentum transport via Maxwell stresses.

After applying this proxy and investigating these consequences of reduced stable mode activity, detailed analyses are presented to validate the proxy and identify its shortcomings. In detailing the connection between Reynolds stress and stable modes, their use in possible reduced models of momentum transport are investigated. Following the methods of Chapter 3, stable and unstable modes alone are shown to describe the Reynolds stress well in the regimes considered here. The Maxwell stress, however, is not well described, both because the large-scale field fluctuations bear little resemblance to the fields of the stable and unstable modes, and because the dominant contributions are from scales much smaller than the scales where these modes lie.

Finally, efforts to more directly identify the increased magnetic field strength as the root cause for the reduction in stable mode activity are presented. Semi-analytic calculations are performed of the tendency for stable and unstable modes to nonlinearly interact leading into saturation at

different magnetic field strengths. This tendency is assessed by calculating the threshold parameter P_t (Terry et al. 2006; Makwana et al. 2011; Fraser et al. 2017), which evaluates the role in instability saturation played by nonlinear coupling between stable and unstable modes relative to nonlinear coupling between unstable modes alone. For the same regimes of magnetic field strength as the nonlinear simulations, a preliminary analysis suggests that coupling to stable modes plays less of a role in instability saturation as field strength increases. This work represents the first time P_t has been calculated in a system where the exact structure of the eigenmodes cannot be calculated in closed form. These calculations were performed by Jack Schroeder (Fraser et al. 2020) in what began as an undergraduate research project under my supervision, and many figures relevant to this project are provided courtesy of him.

This chapter is organized as follows. The system is described in Sec. 4.2, with the equilibrium and governing equations given in Sec. 4.2.1, the linearized equations in Sec. 4.2.2, and the numerical implementation described in Sec. 4.2.3. Results are then shown, starting with an overview of the linear modes in Sec. 4.3 and of the hydrodynamic system in Sec. 4.4. A detailed comparison between the hydrodynamic system and MHD simulations with different field strengths and resistivities is presented in Sec. 4.5, where

counter-gradient momentum transport is used as a proxy for stable mode activity. This proxy is validated in Sec. 4.5.4 by directly calculating the excitation of stable and unstable modes in the nonlinear simulations, and in Sec. 4.5.5 by comparing truncated eigenmode expansions using the same methods as Fraser et al. (2018). Additional details regarding these eigenmode expansions, including how they are calculated in generic systems of the same form as the one studied here, and why the expansions are well-defined and unique in this system, are given in Appendix A, with details specific to this system and the use of Dedalus given in Appendix B. The threshold parameter, and an explanation for how it can generally be calculated even in systems where eigenmode structures cannot be calculated analytically, is presented in Appendix C. Conclusions are presented in Sec. 4.6.

4.2 System setup

4.2.1 Equilibrium, governing equations

We study the evolution of a two-dimensional free shear layer in an incompressible fluid in MHD with finite viscosity and resistivity, with an initially-uniform magnetic field in the direction of the flow. Specifically, we consider an initial flow in the horizontal direction $\hat{\mathbf{x}}$ that varies in the

vertical direction $\hat{\mathbf{z}}$, i.e., $\bar{\mathbf{V}}_0 = \bar{U}(\bar{z})\hat{\mathbf{x}}$,¹ where $\bar{U}(\bar{z}) = \bar{U}_0 \tanh(\bar{z}/\bar{d})$ is the initial flow profile, \bar{U}_0 is the flow speed away from the layer, and \bar{d} is the layer half-width, with an initial, uniform magnetic field $\bar{\mathbf{B}}_0 = \bar{B}_0\hat{\mathbf{x}}$. Here, an overbar denotes a dimensional quantity. Henceforth, we normalize all speeds, distances, and fields according to $U = \bar{U}/\bar{U}_0$, $(x, z) = (\bar{x}/\bar{d}, \bar{z}/\bar{d})$, and $B = \bar{B}/\bar{B}_0$, such that $\mathbf{V}_0 = \tanh(z)\hat{\mathbf{x}}$ and $\mathbf{B}_0 = \hat{\mathbf{x}}$. For the remainder of the chapter, all quantities will be nondimensionalized in terms of \bar{U}_0 , \bar{d} , \bar{B}_0 , and combinations thereof.

We describe the flow velocity and magnetic field in terms of a stream function ϕ and flux function ψ , so that $\mathbf{v} = \hat{\mathbf{y}} \times \nabla\phi$ and $\mathbf{B} = \hat{\mathbf{y}} \times \nabla\psi$. Under our chosen normalizations, we may write the governing equations as (Biskamp 2003)

$$\frac{\partial}{\partial t} \nabla^2 \phi + \{\nabla^2 \phi, \phi\} = \frac{1}{M_A^2} \{\nabla^2 \psi, \psi\} + \frac{1}{\text{Re}} \nabla^4 \phi, \quad (4.1)$$

and

$$\frac{\partial}{\partial t} \psi = \{\phi, \psi\} + \frac{1}{\text{Rm}} \nabla^2 \psi. \quad (4.2)$$

Here, M_A is the Alfvén Mach number, or the ratio of the equilibrium flow speed to the Alfvén speed, and scales like $M_A \propto \bar{U}_0/\bar{B}_0$; Re and Rm are the Reynolds and magnetic Reynolds numbers, respectively, defined as $\text{Re} = \bar{U}_0 \bar{d}/\bar{\nu}$ and $\text{Rm} = \bar{U}_0 \bar{d}/\bar{\mu}$ where $\bar{\nu}$ and $\bar{\mu}$ are kinematic viscosity and

¹Note that the directions of flow and shear here are the same as in Chapter 2 but not Chapter 3.

resistivity; and $\{f, g\} \equiv \partial_x f \partial_z g - \partial_x g \partial_z f$. Equation (4.1) describes the evolution of the vorticity $\nabla \times \mathbf{v} = \nabla^2 \phi \hat{\mathbf{y}}$. The second term on the left-hand side is the vorticity advection term, the first term on the right-hand side is the curl of the Lorentz force, and the second term on the right-hand side is standard viscous dissipation. The terms on the right-hand side of Eq. (4.2) correspond to flux advection and resistive diffusion. This system, with the above equilibrium, is known to be linearly unstable for M_A above a critical threshold that lies between 1 and 2 (Palotti et al. 2008).

4.2.2 Perturbation equations

As will be described in Sec. 4.2.3, we solve Eqs. (4.1) and (4.2) numerically using the code Dedalus (Burns et al. 2020), specifically its initial value problem solvers. Additionally, we use Dedalus' eigenvalue problem solvers to calculate the complex frequencies (eigenvalues) and eigenmodes of these equations linearized about an unstable equilibrium. While initial value calculations can be used to obtain the mode structure and complex frequency of the fastest-growing eigenmode at each k_x , solving the linearized system as an eigenvalue problem allows other modes at the same k_x to be calculated as well, namely stable modes. This is necessary to track the amplitudes of these modes in the ensuing turbulence in the initial value calculations, which then informs how much energy they remove from

fluctuations (Makwana et al. 2014). As with previous studies of stable modes in shear-flow turbulence (Fraser et al. 2017, 2018), we are specifically interested in the dissipationless modes of this system, so eigenmodes are calculated with viscosity and resistivity neglected.

To derive linearized equations, we separate the system into an arbitrary, horizontal, uniform (in x) background flow $U(z)$ and field $B_x(z)$, and perturbations $\tilde{\phi}$ and $\tilde{\psi}$. This allows Eqs. (4.1) and (4.2) to be similarly separated into equations describing the background, and the following equations for the perturbations:

$$\begin{aligned} \frac{\partial}{\partial t} \nabla^2 \tilde{\phi} = & -U \frac{\partial}{\partial x} \nabla^2 \tilde{\phi} + U'' \frac{\partial}{\partial x} \tilde{\phi} + \frac{1}{M_A^2} \left(B_x \frac{\partial}{\partial x} \nabla^2 \tilde{\psi} - B_x'' \frac{\partial}{\partial x} \tilde{\psi} \right) \\ & - \left\{ \nabla^2 \tilde{\phi}, \tilde{\phi} \right\} + \frac{1}{M_A^2} \left\{ \nabla^2 \tilde{\psi}, \tilde{\psi} \right\}, \end{aligned} \quad (4.3)$$

and

$$\frac{\partial}{\partial t} \tilde{\psi} = -U \frac{\partial}{\partial x} \tilde{\psi} + B_x \frac{\partial}{\partial x} \tilde{\phi} + \left\{ \tilde{\phi}, \tilde{\psi} \right\}, \quad (4.4)$$

where primes denote derivatives with respect to z , and we have neglected viscosity and resistivity. Equations (4.3) and (4.4) are the MHD equivalent of Eq. (1) in Fraser et al. (2017), and describe how fluctuations interact linearly with the background flow and field, and nonlinearly with one another. When the fluctuations are small enough that the nonlinearities can be neglected, Fourier transforming Eqs. (4.3) and (4.4) in x and assuming

solutions vary in time as $e^{i\omega(k_x)t}$ yields

$$\begin{aligned} \omega \left(\frac{d^2}{dz^2} - k_x^2 \right) \hat{\phi} = & -k_x U \left(\frac{d^2}{dz^2} - k_x^2 \right) \hat{\phi} + k_x U'' \hat{\phi} \\ & + \frac{1}{M_A^2} \left[k_x B_x \left(\frac{d^2}{dz^2} - k_x^2 \right) \hat{\psi} - k_x B_x'' \hat{\psi} \right] \end{aligned} \quad (4.5)$$

and

$$\omega \hat{\psi} = -k_x U \hat{\psi} + k_x B_x \hat{\phi}, \quad (4.6)$$

where $\hat{\phi}$ and $\hat{\psi}$ are the Fourier transforms (from x to k_x) of $\tilde{\phi}$ and $\tilde{\psi}$.

Thus, at every k_x , we have a separate system of linear, ordinary differential equations in z . For a given k_x and M_A , arbitrary $U(z)$ and $B_x(z)$, and appropriate choice of boundary conditions, this system forms a generalized eigenvalue problem that can be solved to obtain a spectrum of eigenvalues ω_j and eigenmodes $(\phi_j(z), \psi_j(z))$, where $j = 1, 2, \dots$ enumerates the different solutions at each k_x . Each eigenmode is specified by both a ϕ component and a ψ component. For the remainder of this chapter, the notation $\vec{f}_j \equiv (\phi_j(z), \psi_j(z))$ is occasionally used to refer to the entirety of an eigenmode.

4.2.3 Numerical implementation

Dedalus is a pseudo-spectral code with a variety of spectral bases available. We employ Fourier modes $e^{ik_x x}$ in the x direction and Chebyshev polynomials $T_n(z)$ in z . Our simulation domain size is $L_x \times L_z = 10\pi \times 10\pi$,

thus the minimum horizontal wavenumber is $k_x = 0.2$, with periodic boundaries at $x = \pm L_x/2$ and perfectly conducting, no-slip, co-moving (with the equilibrium flow \mathbf{V}_0) walls at $z = \pm L_z/2$. The simulations presented here use a resolution of $N_x \times N_z = 512 \times 2048$, with convergence tests performed at the highest values of Rm by checking that changes in spectral energy density and dissipation with resolution are minimal. This z -resolution is higher than what others have observed to be necessary for well-resolved simulations. However, many of our eigenmode-based post-processing analyses benefit from increased N_z , as it allows continuum modes (Case 1960) to be better-resolved.

Previous work has shown that the nonlinear development of KH-unstable flows depends sensitively on the choice of the initial perturbations that seed the instability (Dong et al. 2019). In studying free shear layers, a common choice of initial condition is a perturbation in one or more velocity fields that is sinusoidal in x , with a wavelength that matches the box size or the fastest-growing linear mode, and Gaussian in z centered about the shear layer (Lecoanet et al. 2016; Palotti et al. 2008), with lower-amplitude noise sometimes added to other horizontal wavenumbers (Mak et al. 2017). Here, we perturb both ϕ and ψ at every nonzero k_x with Gaussians in z that have randomly-assigned, k_x -dependent complex phases and amplitudes

that decrease with k_x as a power law. Thus, at $t = 0$ the streamfunction and flux functions are

$$\phi(x, z) = \sum_{k_x} \hat{\phi}(k_x, z) = \hat{\phi}(0, z) + A_\phi \sum_{k_x > 0} k_x^a e^{i\Delta_\phi(k_x) - z^2/\sigma^2}, \quad (4.7)$$

and

$$\psi(x, z) = \sum_{k_x} \hat{\psi}(k_x, z) = \hat{\psi}(0, z) + A_\psi \sum_{k_x > 0} k_x^a e^{i\Delta_\psi(k_x) - z^2/\sigma^2}, \quad (4.8)$$

where the $k_x = 0$ components are the unperturbed equilibrium profiles, A_ϕ and A_ψ set overall amplitudes for the perturbations, a sets the steepness of the energy spectra of the perturbations, σ sets the width of the Gaussian in z , and at every nonzero k_x , $\Delta_\phi(k_x)$ and $\Delta_\psi(k_x)$ are uniformly-distributed pseudo-random numbers in $[0, 2\pi]$. For the results presented here, we use $\sigma = 2$, $a = -1$, and $A_\phi = A_\psi = 5 \times 10^{-4}$, which allows for a clearly-defined linear growth phase before nonlinear interactions become important. For $M_A = 5$, setting $A_\psi = 0$ did not noticeably change how the instability saturated. This is likely a result of the flow-dominated nature of the instability and the well-defined linear growth phase permitted by our small value of A_ϕ .

Previous work (Dong et al. 2019) has shown that even when only two wavenumbers are perturbed, the details of the nonlinear stage after the instability saturates are sensitive to the complex phase differences

and relative amplitudes between different k_x , the overall amplitude of the perturbation, and the structure in z of the perturbations. In this work, we are interested in studying details of the saturated state as M_A and Rm are varied. In an effort to ensure that our observed trends are not a unique feature of a particular choice of initial conditions, we perform multiple simulations at each M_A and Rm , with different ensembles of Δ_ϕ and Δ_ψ . In practice, this is done by selecting different seeds for our pseudo-random number generator, and using the same seeds for different M_A and Rm so that M_A and Rm can be varied independently with Δ_ϕ and Δ_ψ held fixed. For each value of M_A and Rm presented here, at least five different sets of initial conditions were simulated. While the majority of this chapter presents results from only one set of initial conditions, we focus on results we found to be robust and broadly representative of the range of initial conditions we sampled.

4.3 Eigenmodes, eigenvalues for the $U = \tanh(z)$, $B_x = 1$ equilibrium

The initial perturbations in our nonlinear simulations are small enough to allow a phase of linear growth before nonlinear interactions become relevant. Thus we first describe the linear modes obtained from eigenvalue calculations before describing the ensuing nonlinear stages of the simula-

tions.

Equations (4.5) and (4.6) describe linear fluctuations about an arbitrary background flow U and field B_x so long as it is uniform in x . The background flow and field about which our nonlinear simulations are perturbed is $U = \tanh(z)$ and $B_x = 1$. For this U and B_x , unstable modes, with positive growth rates $\gamma_j = -\text{Im}[\omega_j]$, are observed as expected for wavenumbers in the range $0 < k_x < 1$ as long as M_A is above a critical threshold between 1 and 2. The growth rate of the fastest-growing mode for this system is plotted against k_x for a variety of M_A in Fig. 4.1. While the magnetic field stabilizes the instability if it is strong enough to bring M_A below the critical

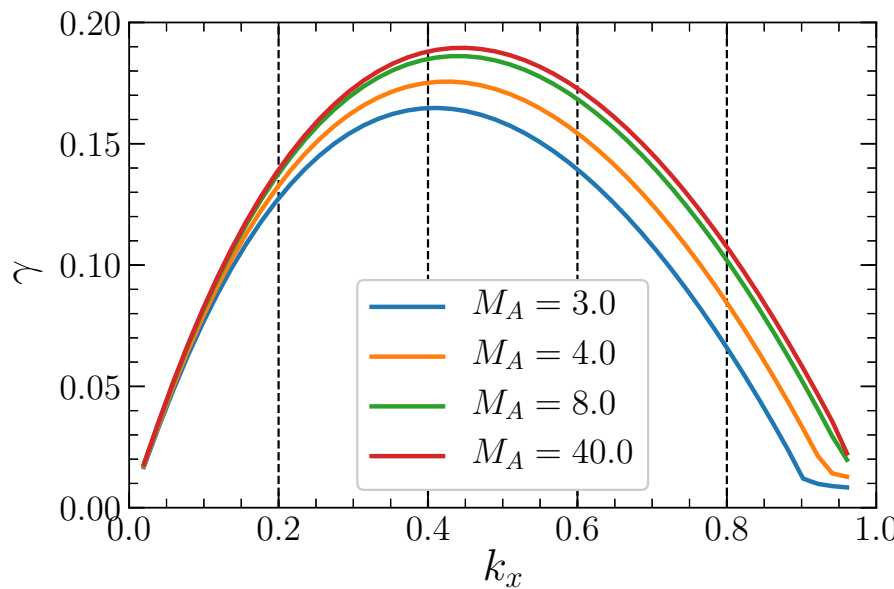


Figure 4.1 Growth rate γ for the fastest-growing mode at each k_x . Each curve corresponds to a different Alfvén Mach number M_A . While stronger magnetic fields (lower M_A) provide a stabilizing influence, γ varies little except when $M_A \lesssim 4$. Horizontal dashed lines indicate the k_x present in our nonlinear simulations. Data provided courtesy of J.M. Schroeder.

threshold, and it noticeably reduces the growth rate for M_A slightly above the threshold, its stabilizing influence appears to be almost negligible for $M_A \gtrsim 8$.

Taking the complex conjugate of Eqs. (4.5) and (4.6) shows that, as in the hydrodynamic case (Drazin & Reid 1981) and the gyrokinetic case (Fraser et al. 2018), for every eigenvalue ω_j and eigenmode (ϕ_j, ψ_j) that is a solution to Eqs. (4.5) and (4.6), the complex conjugate ω_j^* and (ϕ_j^*, ψ_j^*) is a solution as well. Following Chapters 2 and 3 of this thesis, when describing the eigenmodes of the $U = \tanh(z)$, $B_x = 1$ system, we label the most unstable mode at each k_x as $j = 1$ and label its conjugate stable mode as $j = 2$. Real-space contours corresponding to ϕ_j and ψ_j for $j = 1$ and $j = 2$ at $M_A = 40, k_x = 0.4$ are shown in Fig. 4.2. The streamlines of the flow look qualitatively similar to the piecewise-linear profile (Fraser et al. 2017). While the flow component of the mode can be roughly described as a superposition of two waves of vorticity localized about the edges of the layer (a wealth of literature exists on this subject, see, e.g., Baines & Mitsudera (1994); Heifetz et al. (2015); Heifetz & Guha (2019); Carpenter et al. (2013)), the current density of the mode is more localized about the center of the layer. The stable mode is identical in both ϕ and ψ to the unstable mode under the reflection in $x \rightarrow -x$.

The source of free energy that drives the exponential growth of the unstable mode is the equilibrium flow $U(z)$. In terms of Eqs. (4.3) and (4.4), the growth of the mode is due to the (dissipationless) linear terms on the right-hand side. These terms were derived by linearizing the familiar energy-conserving nonlinearities in Eqs. (4.1) and (4.2) about $U(z)$ and $B_x(z)$. If $U(z)$ and $B_x(z)$ are identified as the horizontally-averaged flow and field and held fixed in time, so that only $k_x \neq 0$ perturbations

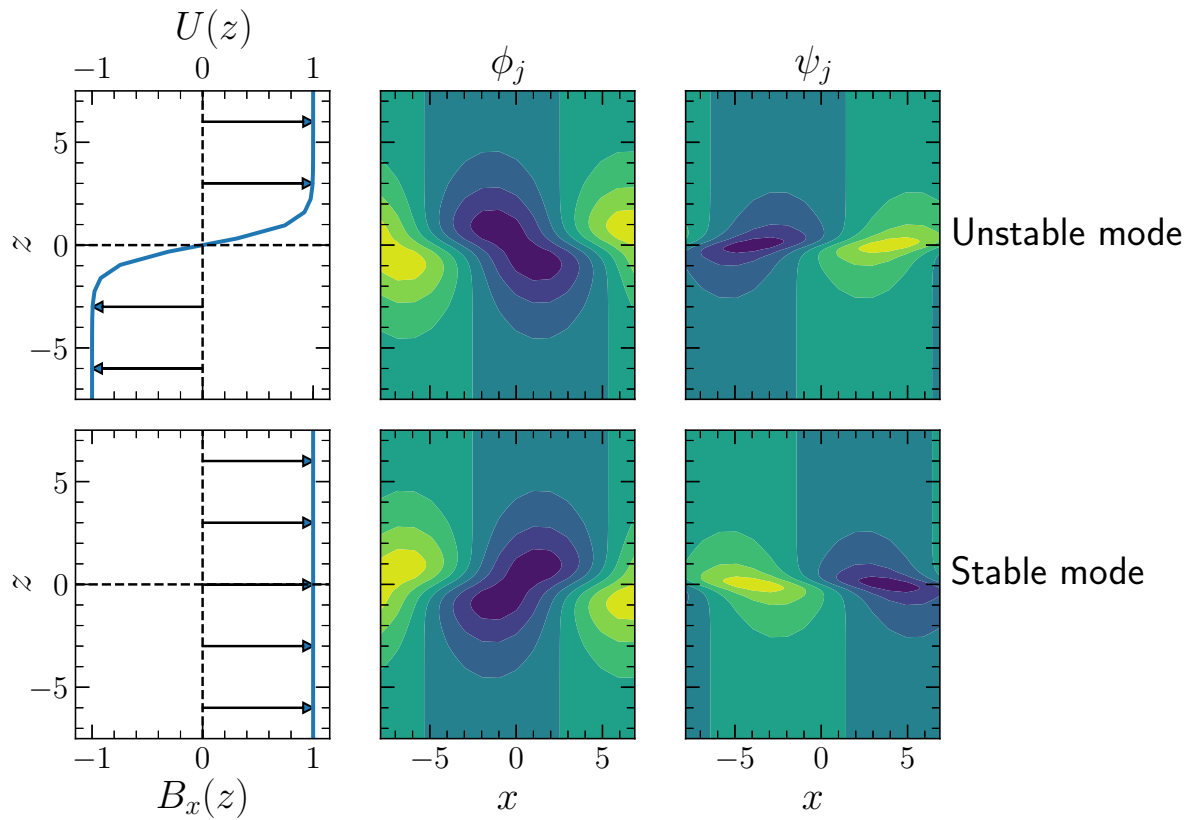


Figure 4.2 The initial $U = \tanh(z)$ unstable equilibrium flow (top left) and uniform field (bottom left) are shown alongside contours of the streamfunction (center column) and flux function (right column) for the unstable (top) and stable (bottom) modes at $k_x = 0.4$ for $M_A = 40$.

are allowed to evolve, as was considered in Fraser et al. (2017), then this exponential growth does not conserve energy, because the energy injected into \vec{f}_1 is not self-consistently removed from the mean flow. This is similarly the case in most δf gyrokinetic simulations with fixed background gradients. However, in direct numerical simulations of Eqs. (4.1) and (4.2), energy is conservatively transferred from the equilibrium to growing perturbations by the nonlinearities. Viewed in terms of a separation between the mean and $k_x \neq 0$ fluctuations, the removal of energy from $U(z)$ occurs via the xz components of the Reynolds and/or Maxwell stress tensors, which we denote as

$$\tau_u \equiv - \left\langle \frac{\partial}{\partial x} \tilde{\phi} \frac{\partial}{\partial z} \tilde{\phi} \right\rangle_x, \quad (4.9)$$

and

$$\tau_b \equiv \frac{1}{M_A^2} \left\langle \frac{\partial}{\partial x} \tilde{\psi} \frac{\partial}{\partial z} \tilde{\psi} \right\rangle_x, \quad (4.10)$$

where $\langle \cdot \rangle_x$ indicates an average in x . These stresses transport horizontal momentum along the vertical axis and evolve the mean flow according to (neglecting viscosity)

$$\frac{\partial}{\partial t} \langle U \rangle_x = \frac{\partial}{\partial z} (\tau_u + \tau_b), \quad (4.11)$$

with a transport of momentum down the gradient, i.e., a flux of x -directed momentum in the $-z$ direction if $U(z) = \tanh(z)$, lowering the kinetic

energy of the mean flow.²

Similarly, the exponential decay of the conjugate stable mode \vec{f}_2 does not conserve energy if $U(z)$ and $B_x(z)$ are held fixed – thus in most gyrokinetic δf simulations, stable modes are a nonconservative energy sink – but does conserve energy when directly simulating Eqs. (4.1) and (4.2), with energy injection into the mean provided by the same stresses (as will be shown in Sec. 4.5.2, a minimal amount of energy is also transferred into the mean field). This is illustrated in Fig. 4.3, where the Reynolds and Maxwell stresses are shown for \vec{f}_1 and \vec{f}_2 at $k_x = 0.4$ for both $M_A = 25$ and

²Regarding the equivalence between energy transfer and momentum transport in the hydrodynamic case, see discussion of the Reynolds-Orr energy equation in Drazin (2002) Sec. 5.3, as well as the last paragraph in Sec. 8.2

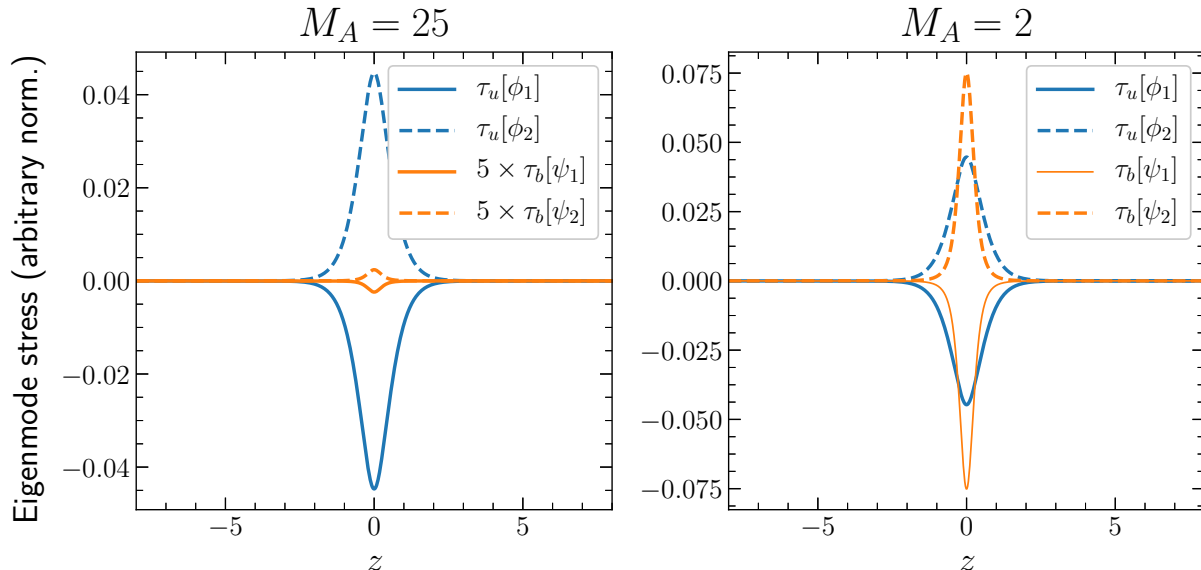


Figure 4.3 $x - z$ components of the Reynolds stress τ_u (blue) and Maxwell stress τ_b (orange) for the unstable mode \vec{f}_1 (solid lines) and stable mode \vec{f}_2 (dashed lines) at $k_x = 0.4$ for $M_A = 25$ (left) and $M_A = 2$ (right). For $M_A = 25$, τ_b is rescaled by a factor of 5 to improve visibility. Modes are normalized to have unit total energy.

$M_A = 2$. For unstable modes, both τ_u and τ_b transport momentum down the gradient, so that they both contribute to a transfer of energy from $U(z)$ to \vec{f}_1 . Likewise, for stable modes, both stresses yield counter-gradient momentum transport, transferring energy from \vec{f}_2 to $U(z)$. The transport of the two modes is symmetric in the sense that $\tau_u[\phi_2] = -\tau_u[\phi_1]$ and $\tau_b[\psi_2] = -\tau_b[\psi_1]$. As M_A is decreased, corresponding to a stronger equilibrium field, the relative amplitudes of τ_u and τ_b change, with $|\tau_b|$ exceeding $|\tau_u|$ for only the strongest equilibrium fields, starting around $M_A \approx 2.5$.

4.4 Hydrodynamic evolution

Here we discuss direct numerical simulations of Eqs. (4.1) and (4.2) and how they vary with M_A and Rm . As the hydrodynamic case is simpler and the effects of stable modes there have already been studied, we begin with an overview of the hydrodynamic system, obtained by solving Eq. (4.1) alone with $\psi = 0$. While 2D, incompressible, unstratified, hydrodynamic shear flows are well-studied and our findings are consistent with previous work, we present an overview for the sake of contrasting with the MHD case. All simulations presented here, both hydrodynamic and MHD, are run with $Re = 500$.

Thanks to our initial perturbations being sufficiently small in amplitude, the initial stage of our simulations is dominated by a well-defined lin-

ear growth phase for each of the linearly unstable horizontal wavenumbers, $k_x = 0.2, 0.4, 0.6$, and 0.8 , after a brief transient stage. This can be seen in Fig. 4.4, where KE_{k_x} , the 1D spectral kinetic energy density defined such that $\text{KE} = \int |\mathbf{v}|^2 dx dz / 2 = \sum_{k_x} \text{KE}_{k_x}$, is plotted for two nearly-identical hydrodynamic simulations whose only difference is the complex phase of different k_x components of the initial perturbation, i.e., $\Delta_\phi(k_x)$ in Eq. (4.7). Consistent with previous work (Dong et al. 2019), the initial condition has a negligible impact on the time at which the fastest-growing Fourier mode, $k_x = 0.4$, first saturates, where saturation can loosely be defined in this context to mean the time at which KE_{k_x} reaches its first local maximum – although for convenience we define saturation of the $k_x = 0.2$ mode as the time at which it reaches its first local maximum *after* the $k_x = 0.4$ mode saturates. The saturation of other modes is more significantly affected by $\Delta_\phi(k_x)$, particularly $k_x = 0.2$, which eventually contains the most energy of the nonzero k_x components. Of the simulations performed, the two shown in Fig. 4.4 are characteristic of the initial conditions leading to the slowest (left) and fastest (right) saturation times for the $k_x = 0.2$ component. Additionally, the linear growth regime ends sooner for the higher k_x modes, $k_x = 0.6$ and 0.8 , than it does for the lower wavenumbers. This will be shown later to be caused by quasilinear flattening affecting these modes

sooner – the linear growth rate calculated from the horizontally-averaged flow $\langle U \rangle_x$ at each time decreases much more rapidly for shorter-wavelength modes than it does for longer-wavelength ones, causing their linear interactions to be overtaken by nonlinear effects sooner. The higher- k_x modes stabilizing first is consistent with the maximum wavenumber for instability decreasing from its initial value as the layer broadens in the hydrodynamic case, see, e.g., Fig. 6 in Hurst et al. (2020).

Without analyzing the role of different linear modes in these simulations in detail, characteristic signatures of inviscid stable modes can already be identified in Fig. 4.4. A close inspection of the kinetic energy in the mean flow $\text{KE}_{k_x=0}$ (plotted on a linear scale in Fig. 4.8) reveals instances of energy

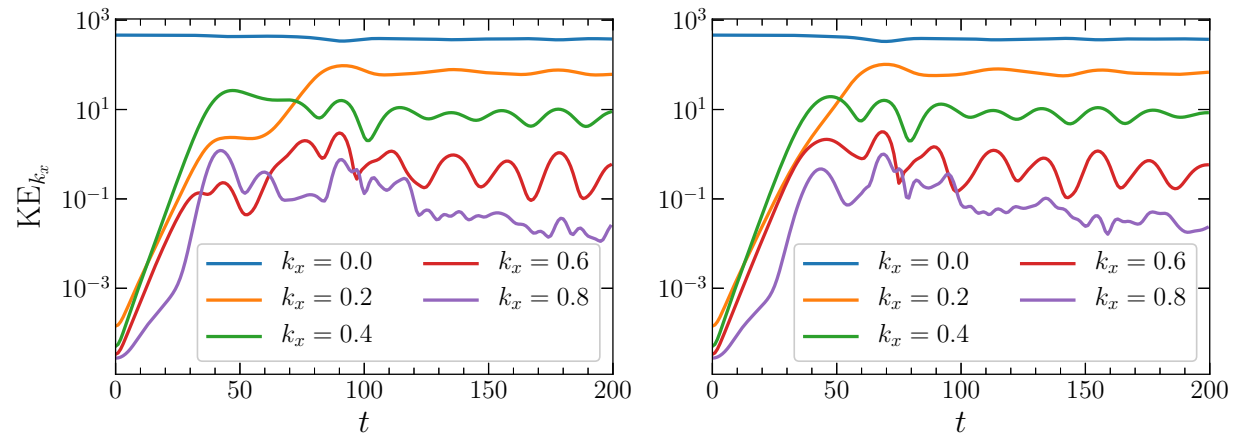


Figure 4.4 Kinetic energy versus time for $k_x = 0$ through 0.8 in two hydrodynamic simulations with different initial conditions, specifically different $\Delta_\phi(k_x)$, corresponding to the two panels. While $\Delta_\phi(k_x)$ has little effect on the saturation time for $k_x = 0.4$ (green) it has a significant effect on the saturation time for $k_x = 0.2$ (orange) (cf. Dong et al. 2019).

transfer back into the mean flow. These events coincide with a loss of energy from large-scale fluctuations following their initial saturation levels. As per the discussion in Sec. 4.3, this is consistent with stable mode activity.

The onsets of saturation for $k_x = 0.4$ and $k_x = 0.2$ are of particular interest as they correspond to large-scale structures observed in the flow. Figure 4.5 shows snapshots of vorticity $\nabla^2\phi$ in color with black overlaid contours of the streamfunction ϕ (corresponding to streamlines of the flow, with regions of closely-spaced contour lines corresponding to faster flow speeds) at four different times for the simulation shown on the left in Fig. 4.4. The four times are chosen to roughly illustrate the initial configuration (after apparent transients have faded), the linear growth regime, the saturation of the $k_x = 0.4$ Fourier mode, and the saturation of the $k_x = 0.2$ Fourier mode. When $k_x = 0.4$ first saturates at roughly $t \approx 40$, this can be seen to correspond to the formation of two coherent vortices. These vortices are connected by thin filaments of vorticity, commonly referred to as braids, that are known to be sites of highly strained flow. As is standard in 2D, unstratified, incompressible, hydrodynamic shear layers, the subsequent evolution consists of neighboring vortices merging to form larger vortices that eventually undergo their own merging process. This progression of mergers typically halts when the resulting vortex size is limited by the

size of the domain. Our domain size restricts this process to only a single merging event where the two precursor vortices merge into one larger vortex. Consistent with previous work (Dong et al. 2019), this merging process is seen to correspond to saturation of the $k_x = 0.2$ Fourier mode, and the time it takes to occur depends significantly on initial conditions. The single-vortex state that follows continues without any dramatic changes as viscosity and our chosen boundary conditions slowly act to dissipate the vortex and presumably relax the system to one of plane Couette flow. This occurs on a longer timescale than what we simulated.

4.5 MHD system, weak-field regime

Compared to its hydrodynamic counterpart, the flow in the MHD system evolves similarly provided that the Lorentz force is weak throughout the simulation. At early times this is guaranteed by a high M_A , corresponding to a weak initial magnetic field. Previous work has shown that an initially weak magnetic field embedded in an electrically conducting fluid can be amplified by vortices (Mak et al. 2017) and regions of high strain (Zweibel 1998; see also Zel’Dovich et al. 1984), both of which are present in this system in the form of the vortices and their connecting braids. In both Mak et al. (2017) and Zweibel (1998) this amplification was shown to increase with Rm , as is the case in our simulations as well. The greater the extent to

which the field is frozen into the flow (i.e. higher Rm), the more efficiently the flow is able to twist and compress field lines and amplify the Lorentz force. Thus, in addition to high M_A , a sufficiently low Rm is necessary for the dynamics to remain nearly hydrodynamic.

The following subsections first present how departures from the hydrodynamic regime can be identified in terms of flow features, energy content, and momentum transport. There, indications of stable mode activity vary-

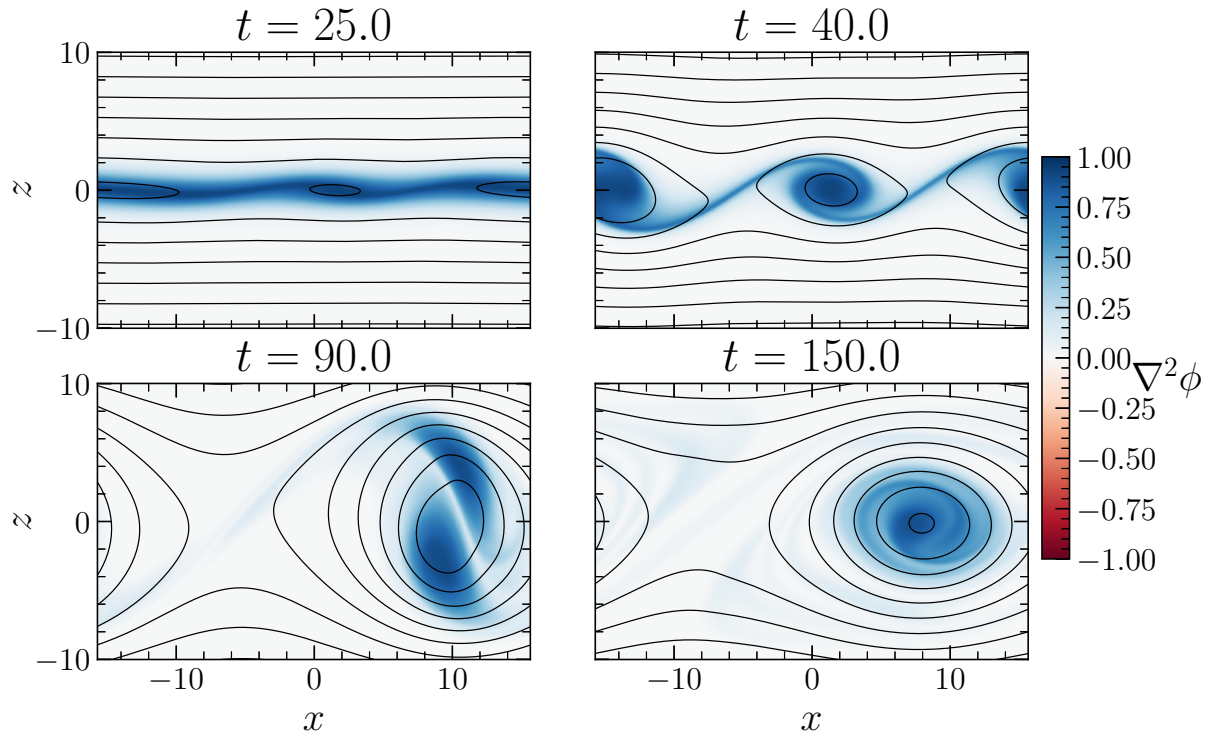


Figure 4.5 Snapshots of the vorticity and streamlines near the shear layer at four different times for the simulation on the left in Fig. 4.4. Color shows vorticity $\nabla^2 \phi$, black lines show contours of the streamfunction ϕ , representing streamlines of the flow. Colorbar normalized with $\nabla^2 \phi = 1$ as the maximum and -1 as the minimum with white as 0 to demonstrate that, here, all of the vorticity is into the page, consistent with the conservative, advection-diffusion nature of the vorticity equation.

ing with field strength provided by the energy and momentum diagnostics are discussed. These indications are discussed to demonstrate that stable and unstable modes provide a useful framework for interpreting the dynamics and the trends with field strength. Several subtleties, justifications, and additional uses for this framework are described in Sec. 4.5.4 and Sec. 4.5.5. However, one simple justification is presented here to lay the groundwork for the remainder of this section, and so that the reader is not expected to be unduly trusting until Sec. 4.5.4.

In Fraser et al. (2017) an expression for the momentum transport S obtained by integrating the Reynolds stress about the edge of the shear layer was given in terms of the amplitudes β_j of stable and unstable modes (see Eq. (2.23) of this thesis). For modes with zero real frequency such as the stable and unstable modes of the equilibrium considered here, the $\beta_m\beta_n^*$ cross terms cancel leaving an expression of the form $S \propto |\beta_2|^2 - |\beta_1|^2$. Despite significant differences between the present system and the one studied in Fraser et al. (2017), this relationship between Reynolds stress and mode amplitudes remains valid. This is shown in Fig. 4.6, where the contribution to τ_u by $k_x = 0.2$ and $k_x = 0.4$ fluctuations are evaluated at $z = 0$ and plotted over time for simulations with different M_A . The expression $|\beta_2|^2 - |\beta_1|^2$ is plotted as well. The two quantities are seen to

agree remarkably well up to a constant of proportionality that depends on k_x but not on M_A . This motivates the use of Reynolds stress as a proxy for the relative amplitudes between stable and unstable eigenmodes.

4.5.1 Flow, field features

Figure 4.7 shows snapshots of the flow and field at $t = 40, 60$, and 150 for a simulation with $M_A = 60$, $\text{Rm} = 250$, and an identical initial $\Delta_\phi(k_x)$ to the simulation shown in Fig. 4.5 (the initial $\Delta_\psi(k_x)$, when varied by itself, was not observed to affect the evolution of the system in any significant way). By the time the fastest-growing mode saturates at $t = 40$, current sheets form primarily along the braids connecting the KH rollers due to

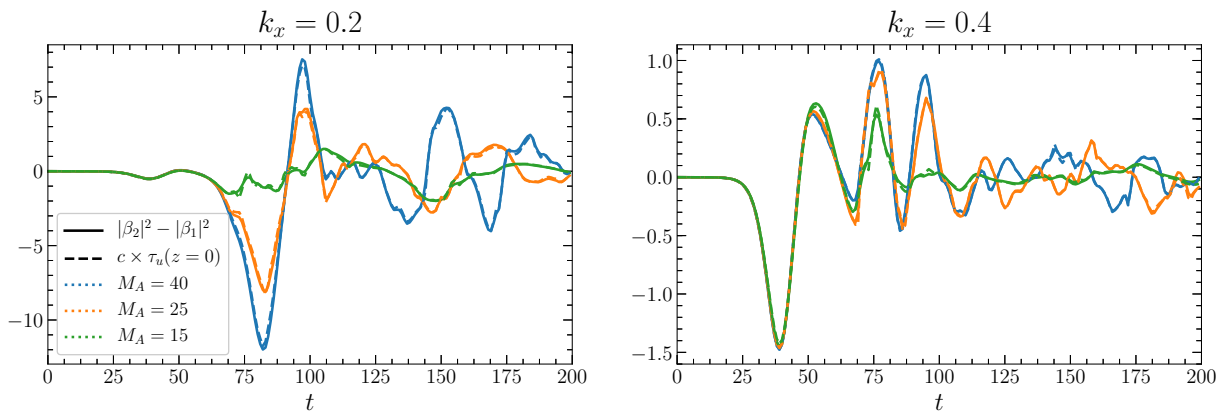


Figure 4.6 Dashed curves show the contribution to Reynolds stress τ_u made by fluctuations at $k_x = 0.2$ (left) and 0.4 (right) evaluated at $z = 0$ versus time for simulations with three different M_A . Solid curves show the quantity $|\beta_2|^2 - |\beta_1|^2$ over time for the same simulations, where β_j is the amplitude of mode \vec{f}_j , described in detail in Sec. 4.5.4. The agreement between the two quantities justifies the use of τ_u as a proxy for relative mode amplitudes.

the high strain rate of the flow. Despite this field amplification, no back-reaction onto the flow is discernible when compared to the hydrodynamic case in Fig. 4.5, and the vortex merging process remains essentially the same. By $t = 150$, well into the single-vortex stage, stronger current sheets have formed both near the stagnation point and at the edge of the vortex, after field lines within the vortex have reconnected and drifted outwards by a process known as flux expulsion (Weiss 1966). Regions of slightly negative vorticity have formed due to the Lorentz force, mostly near the stagnation

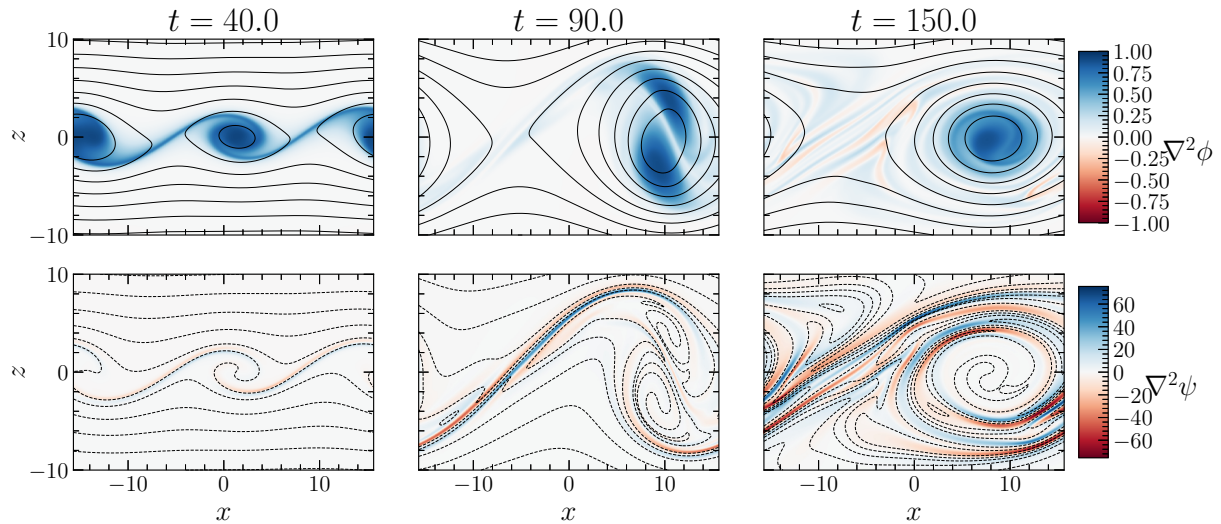


Figure 4.7 Snapshots of the flow (top) and field (bottom) near the shear layer at three times in a simulation with $M_A = 60$ and $Rm = 250$. Black lines are contours of ϕ (top) and ψ (bottom), representing streamlines and field lines, and color represents vorticity (top) and current density (bottom) into the page. Current sheets form early in the simulation along the braids between vortices, as well as at the edges of the vortex at later times. Even at this high M_A and low Rm , the Lorentz force breaks vorticity conservation and introduces some negative vorticity late in the simulation, presenting a departure from the hydrodynamic evolution.

point, though the overall flow structure remains similar to the hydrodynamic case.

4.5.2 Energy content

The top row of Fig. 4.8 shows different components of energy over time for the simulation in Fig. 4.7 in solid, dashed, and dot-dashed lines, with dotted lines shows the kinetic energy for the hydrodynamic simulation in Fig. 4.5. Comparing the solid and dotted lines for the smallest non-zero k_x shows that the initial saturation and merging states exhibit no dramatic changes between the hydrodynamic and MHD simulations. However, the kinetic energy in the largest scales depletes more quickly as time goes on in the MHD case. Meanwhile, the MHD simulation has slightly greater kinetic energy at small scales (purple curve) than the hydrodynamic counterpart, and even more magnetic energy than kinetic energy.³ Evidently, even this weak magnetic field enhances the transfer of energy from large to small scales. In other systems, stable mode activity reduces the rate at which energy is transferred to smaller scales (Makwana et al. 2014), suggesting that the enhanced energy transfer here is a consequence of stable modes

³Figure 4.7 shows the dominant flow structures are broadly isotropic while the dominant field structures are clearly not, as evidenced by the long, thin current sheets. Therefore, while identifying large k_x with small-scale fluctuations and small k_x with large-scale fluctuations seems appropriate for the flow, it is somewhat misleading for the field. For instance, the low- k_x Fourier components of $\hat{\psi}$ certainly include structures that are small scale in z . Nevertheless, this identification provides a helpful framework for interpreting the results. Also, high- k_x components of $\hat{\psi}$ certainly do correspond to small-scale structures.

becoming less important relative to the hydrodynamic case.

The total kinetic energy in $k_x > 0$ modes is significantly greater than the corresponding magnetic energy, which was shown in Mak et al. (2017) to be an indication that the effect of the Lorentz force on the flow is almost

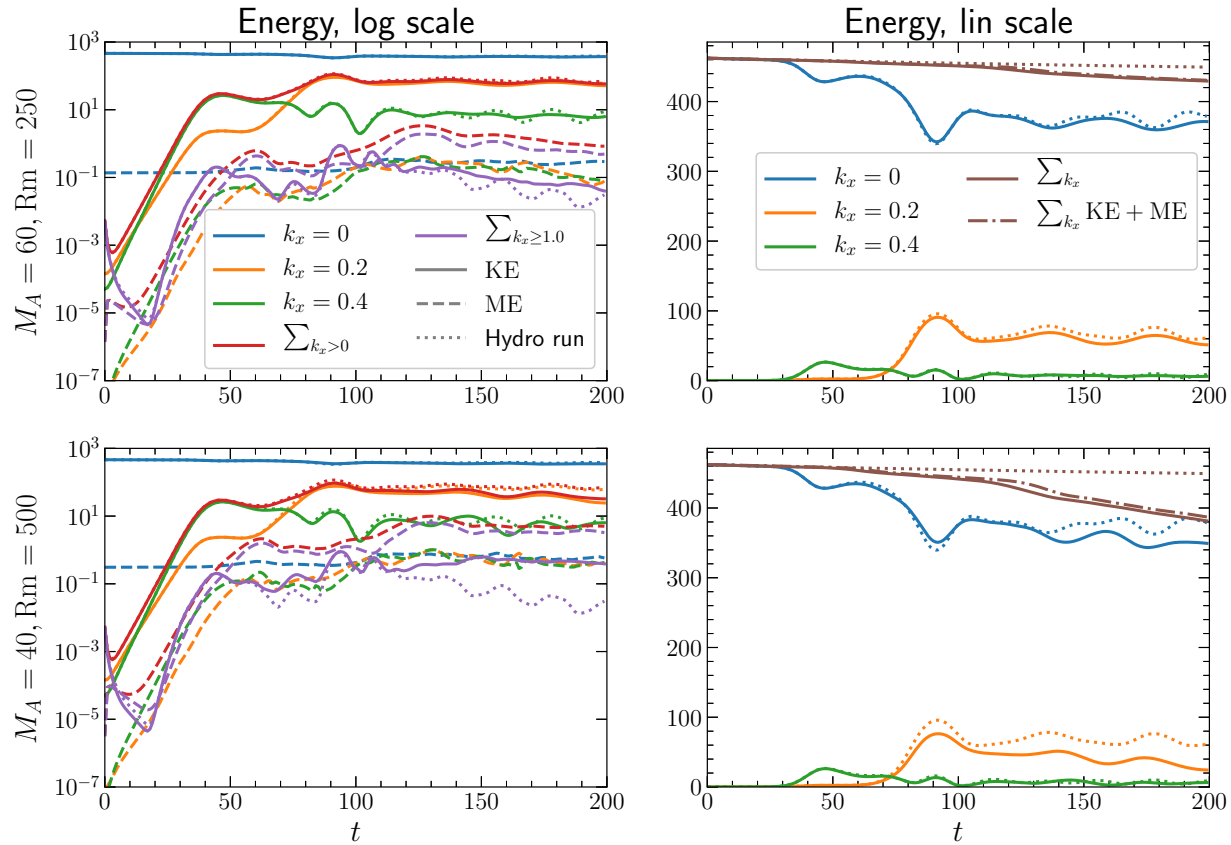


Figure 4.8 Energy components versus time for the simulation shown in Fig. 4.7 with $M_A = 60$ and $Rm = 250$ (top row), and a similar simulation with $M_A = 40$ and $Rm = 500$ (bottom row). The left column plots energy on a log scale and the right on a linear scale. Solid, dashed, and dot-dashed curves correspond to kinetic, magnetic, and total energy, respectively. Dotted curves correspond to the hydrodynamic case (identical between top and bottom rows). Colors indicate different k_x contributions. The initial saturation and merger stages show no obvious changes from the hydrodynamic case, but local minima in $KE_{k_x=0}$ (blue) become less pronounced with stronger fields. Small-scale fluctuations become enhanced with increased field strength.

negligible. By comparing $\text{KE}_{k_x=0.2}$ and $\text{KE}_{k_x=0.4}$ to $\sum_{k_x>0} \text{KE}_{k_x}$, the kinetic energy in the fluctuations is seen to be concentrated in the largest scales. Meanwhile, the fluctuating field is seen to be mostly dominated by smaller scales. This will be shown in Sec. 4.5.3 to be consistent with the contribution to momentum transport made by flow and field fluctuations at different scales. Comparing the total energy summed over all wavenumbers between the hydrodynamic and MHD simulations shows that the added magnetic field, though weak, noticeably increases the rate at which energy is lost to dissipation.

The bottom row of Fig. 4.8 corresponds to a simulation with the same initial conditions, but with $M_A = 40$ and $\text{Rm} = 500$. Compared to the top row, each of the departures from the hydrodynamic case described above is more pronounced, especially later in the simulation when the magnetic field has become more amplified due to the higher Rm . The kinetic energy at the largest scales and the total energy in the whole system both dissipate more quickly, the kinetic energy at small scales is somewhat larger, and the magnetic energy at small scales is much larger. This suggests that stable modes play less of a role as the field strength is increased. While both M_A and Rm have been varied between these two simulations, these trends similarly hold when only one parameter is varied.

With counter-gradient momentum transport understood to be a sign of stable mode activity, and momentum transport being linked to $\text{KE}_{k_x=0}$, additional evidence for stable mode activity can be shown in Fig. 4.8. Whenever $\text{KE}_{k_x=0}$ reaches a local minimum in time, the subsequent increase in $\text{KE}_{k_x=0}$ indicates counter-gradient momentum transport, and thus stable mode amplitudes exceeding unstable mode amplitudes. These local minima in $\text{KE}_{k_x=0}$ are accompanied by local maxima of kinetic energy in most energetic wavenumber, $k_x = 0.2$ or 0.4 , pointing towards significant energy exchange between these modes and the mean flow (as is further demonstrated in terms of Reynolds and Maxwell stresses in the following subsection). The top row of Fig. 4.8 shows that kinetic energy in these large scales generally remains lower in the MHD cases than the hydrodynamic one, while the bottom row shows it becomes even lower in the stronger-field case. The enhanced transfer of energy to small scales caused by the magnetic field has in some sense damped the larger scales. This effective damping leaves an imprint on the signs of stable and unstable mode activity. Comparing the local minimum in $\text{KE}_{k_x=0}$ around $t \approx 90$ between the hydrodynamic and MHD cases shows that the reduced energy content in $k_x = 0.2$ leads to both a decrease in down-gradient transport leading into the minimum and a decrease in counter-gradient transport after the minimum. This is

consistent with a decrease in both unstable and stable mode activity, as is seen in Fig. 4.6 where the difference in square amplitudes of the two modes gets closer to 0 on either side of $t \approx 90$ as M_A decreases. A decrease in this difference can either arise from both stable and unstable mode amplitudes decreasing, or from their amplitudes reaching more similar values (e.g. the stable mode amplitude increasing until it is equal to the unstable mode amplitude). In Sec. 4.5.4, both effects are shown to occur here, with the former more dominant, which is consistent with the observations presented here. The enhanced transfer of energy to small scales and the overall increase in the rate at which kinetic energy is removed from the mean flow suggest a greater disruption of stable mode activity than unstable mode activity. This is reminiscent of the damping term included in Fraser et al. (2018) that preferentially affected large-scale fluctuations and was shown to suppress stable modes more than it suppressed unstable modes.

The enhanced transfer of energy to small scales coincides with an overall increase in energy dissipation. While the MHD case does have more kinetic energy at small scales than its hydrodynamic counterpart, the increased dissipation is almost entirely due to the addition of resistive dissipation. This is seen in Fig. 4.9, where viscous and resistive dissipation are plotted for a variety of simulations, each with the same initial condition but different

M_A and Rm . For simulations where the amplified field is not sufficiently strong, the viscous dissipation remains essentially identical to that of the hydrodynamic case. This threshold depends on both M_A and Rm . For $M_A = 60$, viscosity doesn't increase until Rm reaches 1000, while for $M_A = 40$ the $\text{Rm} = 500$ simulation does exhibit enhanced viscosity while the $\text{Rm} = 250$ case (not shown) does not. Resistive dissipation, on the other hand, matches or even exceeds viscous dissipation, consistent with small scales being dominated more by magnetic than kinetic energy. As expected from Eq. (6) in Zweibel (1998), the local maxima in resistive dissipation are

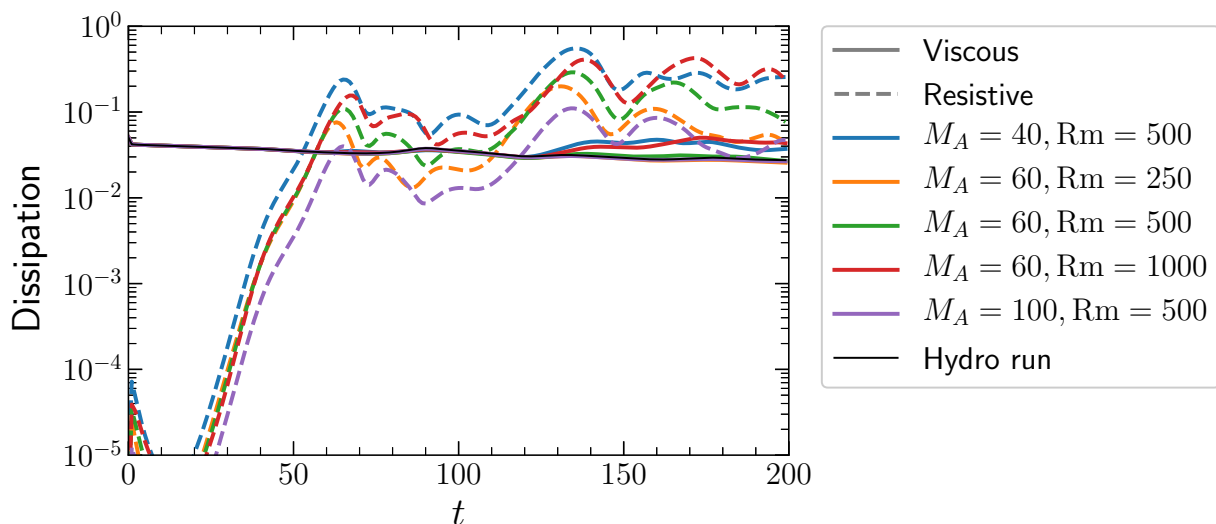


Figure 4.9 Viscous (solid) and resistive (dashed) dissipation over time for simulations with the same initial conditions as those in Figs. 4.5 and 4.7, with different colors corresponding to different M_A and Rm , and black corresponding to the hydrodynamic case. Even a weak magnetic field significantly increases total dissipation relative to the hydrodynamic case. Resistive dissipation increases with Rm , and peaks at a time that increases with Rm . Viscous dissipation is similar to the hydrodynamic case except when the amplified field increases beyond a threshold that depends on both M_A and Rm .

greater and occur later with increasing Rm , as the current sheets formed by the high-strain-rate flow take longer to reach small enough scales that resistivity overtakes flux advection.⁴ While M_A has no clear effect on the time of these local maxima in high- M_A simulations, it does affect the overall level of resistive dissipation, with stronger fields (lower M_A) yielding greater resistive dissipation. This can be understood as a lower M_A increasing the amplitude of the magnetic fluctuations that reach small scales.

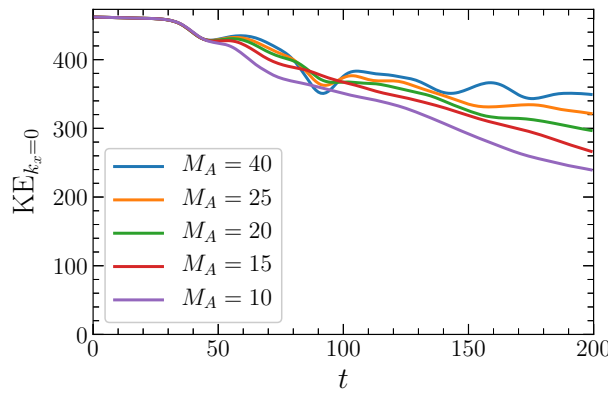


Figure 4.10 Kinetic energy over time in the mean flow, $KE_{k_x=0}$, for a variety of M_A . Each simulation has $Rm = 500$ and the same initial conditions as Fig. 4.7. As field strength increases (M_A decreases), $KE_{k_x=0}$ decreases more rapidly and its local minima, which indicate phases of counter-gradient momentum transport, weaken and gradually cease.

4.5.3 Momentum transport

The previous subsection noted that as magnetic field strength increases, the local minima in time of the kinetic energy of the mean flow $\text{KE}_{k_x=0}$ become less pronounced. Figure 4.10 shows $\text{KE}_{k_x=0}$ versus time for simulations with $\text{Rm} = 500$, the same initial conditions as the simulation in Fig. 4.7, and a variety of M_A . As field strength increases, the local minima become less pronounced and gradually vanish. The minima that occur latest in the simulation are the first to vanish, while the earliest minimum remains until $M_A \approx 10$. Beyond the suppression of these local minima, $\text{KE}_{k_x=0}$ decays more rapidly overall with stronger fields, consistent with the increased transfer to small scales and energy dissipation noted in the previous subsection. This is robust to changes in initial conditions. While different initial conditions affect the exact times at which local minima in $\text{KE}_{k_x=0}$ occur (except for the first one, as was shown in Fig. 4.4), the broad trends described throughout this subsection apply to all our tested initial conditions.

The momentum transport at four different times for the simulation in

⁴This trend is mostly robust to changes in initial conditions. However, note that for initial conditions where the merging of the two initial vortices occurs rapidly, the first peak in resistive dissipation may be determined by the time when the merging process disrupts the first current sheet along the braid between the two vortices (e.g. the current sheet seen at $t = 40$ in Fig. 4.7), rather than being determined by resistive effects disrupting the sheet (Zweibel 1998). For these reasons, care must be taken when studying dissipative processes in KH-unstable systems in MHD to consider appropriate initial conditions, box sizes that permit mergers if relevant (although Mak et al. 2017, were more interested in the dynamics of a single vortex, not necessarily KH), and explicit dissipation wherever possible.

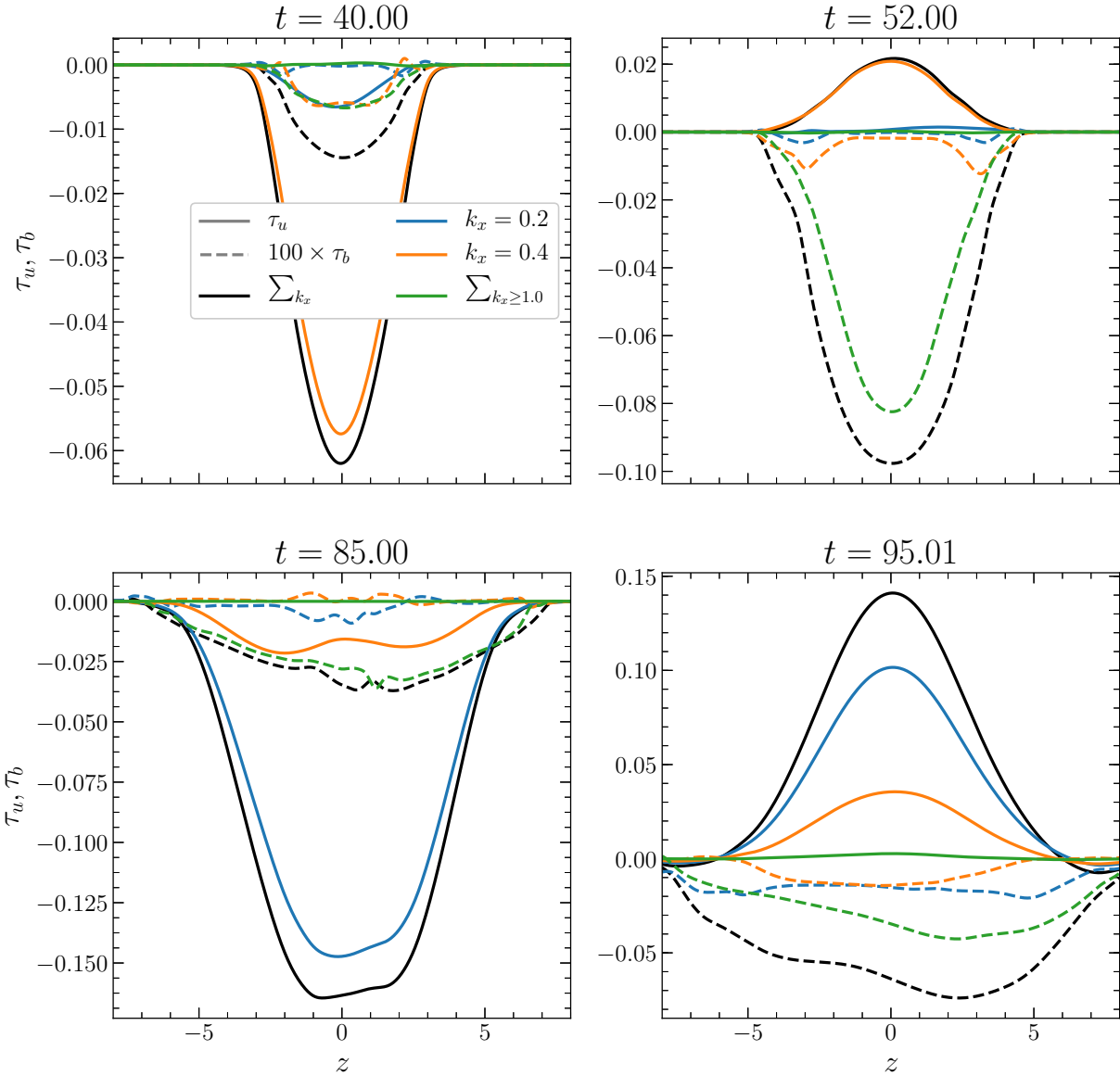


Figure 4.11 Different contributions to momentum transport at four different times for the same simulation as in Fig. 4.7. Solid lines show Reynolds stresses τ_u and dashed lines show Maxwell stresses τ_b (rescaled by a factor of 100 for improved visibility). Black lines are the total Reynolds and Maxwell stresses, while different colors indicate contributions from different k_x . While τ_b is generally dominated by larger k_x and is always negative, τ_u is dominated by smaller k_x and changes sign over time.

Fig. 4.7 is broken into different components in Fig. 4.11. The transport is separated both into Reynolds stress τ_u versus Maxwell stress τ_b and into contributions from different k_x . The four times shown are shortly before and after the first two local minima in $\text{KE}_{k_x=0}$. At all times, Reynolds stress dominates Maxwell stress by over an order of magnitude. The Reynolds stress is dominated first by $k_x = 0.4$ and then by $k_x = 0.2$, consistent with these scales containing the majority of the kinetic energy in the fluctuations about the mean. This further demonstrates that the local minima in $\text{KE}_{k_x=0}$ are due to nonlinear interactions with these two wavenumbers, serving to establish the connection made in the previous subsection between Fig. 4.6 and trends in $\text{KE}_{k_x=0}$. The shapes of the Reynolds stress curves at these scales resemble the Reynolds stresses of the eigenmodes shown in Fig. 4.3, with the curves broadening at later times, consistent with the broadening of the flow profile. The Maxwell stress, on the other hand, is dominated by scales beyond the initially unstable range, aside from the very first panel, again consistent with the breakdown of magnetic energy shown in Fig. 4.8. The Maxwell stress curves bear less of a resemblance to those of the eigenmodes shown in Fig. 4.3, particularly as time goes on. When counter-gradient momentum transport does occur, it is always due to the Reynolds stress changing sign. The Maxwell stress consistently transports

momentum down the gradient, though not in a way that is captured by a simple Fick's law.

It can be shown that a linear combination of \vec{f}_1 and \vec{f}_2 alone will always yield Reynolds and Maxwell stresses of the same sign, with the sign determined by whichever mode has a higher amplitude. Thus, because τ_u and τ_b have opposite signs at some times in these simulations, models that incorporate only these two modes (Fraser et al. 2018) cannot accurately describe both τ_u and τ_b . It is therefore not immediately obvious that down-gradient and counter-gradient momentum transport can be taken as universal indicators of unstable and stable mode activity, as was done in discussing $\text{KE}_{k_x=0}$. Fortunately, we have demonstrated in Fig. 4.6 that isolating the τ_u contribution to transport does provide such an indicator. Furthermore, τ_u dominates over τ_b at weaker field strengths (where this threshold depends on M_A , Rm, and t). Thus, their combined momentum transport, which can be gleaned from timetraces of $\text{KE}_{k_x=0}$, can be traced to stable mode activity.

Figure 4.12 shows how the Reynolds and Maxwell stresses change with M_A , focusing on the first two counter-gradient transport phases. As field strength increases, either because of a stronger initial field from a decreased M_A or more field amplification from an increased Rm (not shown), $|\tau_b|$

increases. This reduces the net counter-gradient transport during these phases and increases down-gradient transport at other times. In the first phase of counter-gradient transport, τ_u remains mostly unchanged with M_A . Thus, the relative amplitudes between stable and unstable modes does not significantly change with M_A at this time (this is further confirmed by referring back to Fig. 4.6). So while stable mode activity does become less prominent at this time as field strength increases, it is not due to a clear

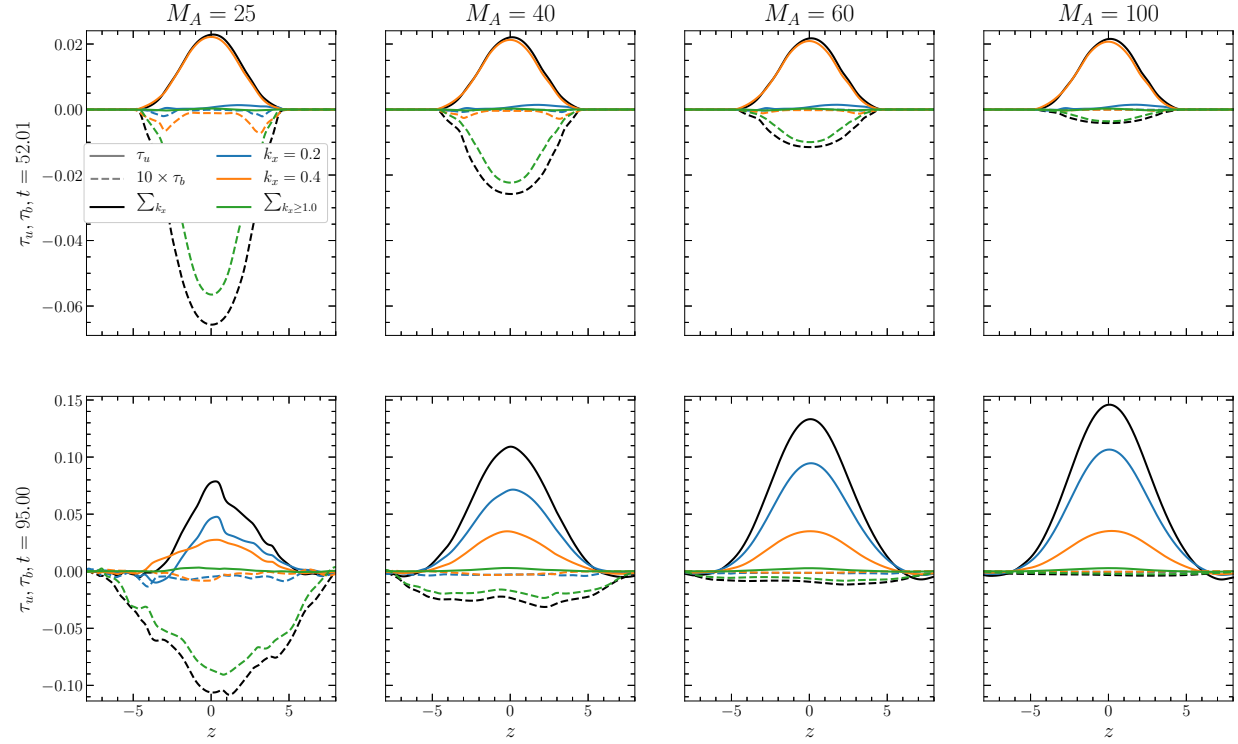


Figure 4.12 The same breakdown of stresses as in Fig. 4.11, but for four simulations with $Rm = 500$ and different M_A (one column per simulation). The two rows correspond to the first two instances of counter-gradient momentum transport. Note τ_b is rescaled by a factor of 10. As M_A decreases, τ_b becomes more dominant, reducing net counter-gradient transport. At earlier times $|\tau_u|$ varies little with M_A , but at later times it decreases with stronger fields

suppression of stable modes relative to unstable ones (cf. Fraser et al. 2018) and a corresponding decrease in counter-gradient τ_u . Instead, the influence of large-scale stable modes has become less prominent due to an increase in energy transfer to small scales leading to increased $|\tau_b(k_x)|$ for large k_x .⁵ For $Rm = 500$, this holds true for all simulations with $M_A \gtrsim 5$. For lower M_A , the counter-gradient $\tau_u(k_x = 0.4)$ at this time does become partially reduced and then fully removed as M_A decreases, and τ_b remains down-gradient but becomes dominated by larger scales.

In the second phase of counter-gradient transport, the dominant contributor to the Reynolds stress, $k_x = 0.2$, becomes noticeably weaker with stronger fields. This trend in τ_u amplitudes is similar to what happens during the down-gradient transport phases at $t = 40$ and 85 : $|\tau_u|$ becomes weaker as field strength increases at later times (the second local minimum of $KE_{k_x=0}$), but does not change with M_A at earlier times (the first local minimum). However, the variation in $|\tau_u|$ with M_A is slightly greater during counter-gradient phases than down-gradient ones. Using τ_u as a proxy for relative amplitudes of stable and unstable modes, this would suggest that both stable and unstable mode amplitudes are reduced as field strength increases, with a slightly larger effect on stable modes.

⁵In terms of the P_t analysis presented in Appendix C, one might speculate that this can be related to an increase in the denominator in Eq. (C9), rather than a decrease in the numerator.

From these results, the overall increase in down-gradient transport and decrease in $\text{KE}_{k_x=0}$ with field strength can be interpreted as a combination of two factors. First, reduced counter-gradient transport from large-scale flow fluctuations, and second, enhanced down-gradient transport from small-scale field fluctuations. The former is a direct result of decreased stable mode amplitudes (Fraser et al. 2017), while the latter is an indirect result of stable modes playing a less prominent role in this system, and thus allowing more energy to reach small scales (Makwana et al. 2014).

4.5.4 Directly calculating stable mode excitation

The potential for large-scale inviscid stable modes to drive counter-gradient momentum transport provided they reach sufficient amplitude has been presented in Fraser et al. (2017) for a simpler system and Fig. 4.3 for the present one. Conversely, reversals in τ_u have been used as a proxy for stable mode activity throughout this section, justified in large part by the observation presented in Fig. 4.6 that τ_u evaluated at the center of the layer for a given wavenumber is directly proportional to $|\beta_2|^2 - |\beta_1|^2$ at that same wavenumber. Here, we perform eigenmode decompositions of our nonlinear simulations to more carefully validate this proxy and specify the physical meaning of the mode amplitudes plotted in Fig. 4.6 when considering a system where the mean flow evolves freely.

At every time t in a simulation of Eqs. (4.1) and (4.2), the system state $\hat{f}(k_x, z, t) \equiv (\hat{\phi}(k_x, z, t), \hat{\psi}(k_x, z, t))$ evaluated at a wavenumber k_x for which we have an appropriate (defined in Appendix A) set of eigenmodes $\{\vec{f}_j(k_x, z)\}$ can be expressed as

$$\hat{f}(k_x, z, t) = \sum_j \beta_j(k_x, t) \vec{f}_j(k_x, z). \quad (4.12)$$

In this section, we calculate the complex, time-dependent amplitudes β_j of various eigenmodes \vec{f}_j as the system evolves in our nonlinear simulations. This is done using similar methods to Hatch et al. (2011), Terry et al. (2014), and Fraser et al. (2018). Mathematical details concerning why these amplitudes are well-defined and unique, how they can generally be calculated, modifications to previous methods (Hatch et al. 2011; Terry et al. 2014; Fraser et al. 2018) that are often necessary, and how they compare to what are known as either projections (Pueschel et al. 2016; Faber et al. 2018; Whelan et al. 2018, 2019; Pueschel et al. 2019) or cosines of Hermitian angles (Dong et al. 2019), are provided in Appendix A. Practical details specific to this system and to Dedalus are discussed in Appendix B. Appendix C presents how the nonlinear perturbation equations of a given system, here Eqs. (4.3) and (4.4), are used to derive equations for the time-evolution of the mode amplitudes given by Eq. (C8). These equations then allow the propensity for different modes to nonlinearly interact and the role of stable

modes in instability saturation to be quantified without a direct numerical simulation of the system (Terry et al. 2006; Makwana et al. 2011; Fraser et al. 2017). The same methods described in these appendices are also described in Chapter 6 of Burns (2018), where they are used to study the dissipation of orbital energy by tidal processes in binary neutron stars due to nonlinear coupling of p-modes and g-modes.

Section 4.3 described the eigenmodes of the $U = \tanh(z)$, $B_x = 1$ equilibrium about which our nonlinear simulations are perturbed. However, as the system evolves and turbulent fluctuations influence the structure of the mean flow $\langle U \rangle$ and field $\langle B_x \rangle$, the eigenmodes and eigenvalues of the original equilibrium may become less appropriate. Importantly, the amplitudes and growth rates of a set of eigenmodes relate to the energy transfer between fluctuations and *the equilibrium about which the modes are defined* (see, e.g., the last paragraph in Sec. III. A. of Makwana et al. 2011). If the mean flow and field differ from their equilibrium profiles, then while the amplitudes of the eigenmodes of the equilibrium will here be shown to still serve as a proxy for energy transfer to and from the mean, an exact relationship requires expanding fluctuations in terms of the eigenmodes of $\langle U \rangle$ and $\langle B_x \rangle$. Additionally, the width in z of the eigenmodes, and hence their corresponding Reynolds and Maxwell stresses, depends

on the width of the shear layer about which they are calculated (see, for instance, Chandrasekhar 1961, Sec. 102, Eq. (46)). Thus, the broadening of the stresses over time in this system, shown in Fig. 4.11, cannot be captured by stable and unstable modes that do not account for the broadening of the layer.⁶ Here we analyze the system in terms of the eigenmodes of the original equilibrium as well as the eigenmodes of the mean flow and field, obtained by solving Eqs. (4.5) and (4.6) using $\langle U \rangle$ and $\langle B_x \rangle$ in place of U and B_x . Both sets of modes were verified to be valid bases. To distinguish them from eigenmodes and amplitudes corresponding to the equilibrium, eigenmodes calculated using $\langle U \rangle$ and $\langle B_x \rangle$ will be denoted $\vec{f}_{\langle j \rangle}$, their frequencies and growth rates $\omega_{\langle j \rangle}$ and $\gamma_{\langle j \rangle}$, and their amplitudes $\beta_{\langle j \rangle}$. The calculations presented here were improved by a z -resolution that was greater than what might otherwise be necessary for well-resolved simulations of this system.

Figure 4.13 shows how the growth rates $\gamma_{\langle j \rangle}$ evolve over time for the most unstable mode at the four initially-unstable wavenumbers for a simulation with $M_A = 40$, $Rm = 500$, and the same initial conditions as Fig. 4.7. Even when the mean flow has hardly evolved in the first few timesteps in the simulation, the growth rates begin to noticeably

⁶Note that, as explained in Appendix A, the eigenmodes of both systems are complete. Therefore the system state, including the broadening of the stresses, is exactly reproduced when the summation in Eq. (4.12) is taken over all of the modes of either system. But this is merely a result of the completeness of the two bases, and not a physically meaningful consequence of the modes themselves

decline, particularly at the higher wavenumbers. The highest wavenumbers stabilizing first is consistent with the maximum wavenumber for instability decreasing from its initial value (here, $k_x = 1$) as the layer broadens in the hydrodynamic case, see, e.g., Fig. 6 in Hurst et al. (2020). This explains the earlier end of the linear growth phase for higher wavenumbers that was noted in Sec. 4.5.2.

As the layer broadens and growth rates decrease, the full spectrum of eigenvalues at each wavenumber initially remains consistent with the original spectrum – which is not shown, but is essentially identical to Fig. 2 (a) in Fraser et al. (2018). Likewise, the general structure in z of $\vec{f}_{\langle 1 \rangle}$ and $\vec{f}_{\langle 2 \rangle}$ initially resembles \vec{f}_1 and \vec{f}_2 , with the mode broadening as the layer width increases. However, departures of $\langle U \rangle$ from a broadened tanh profile

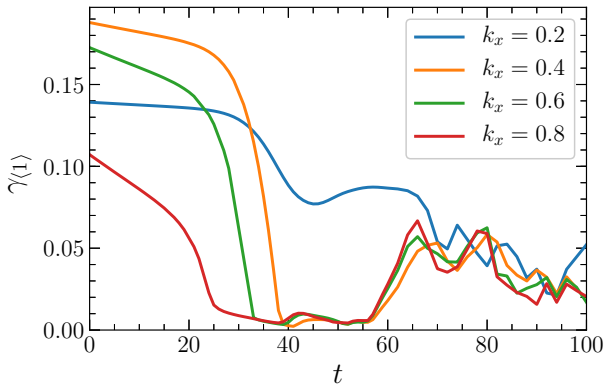


Figure 4.13 Growth rate for the eigenmodes of $\langle U \rangle$ and $\langle B \rangle$ taken from a simulation with $M_A = 40$, $Rm = 500$, and the same initial conditions as Fig. 4.7. Different colors correspond to different wavenumbers. For each wavenumber and at each time, only the most unstable growth rate is plotted. Even when perturbations are small and the energy removed from the mean flow appears negligible at early times, the growth rates at higher k_x decline rapidly.

often introduce new unstable and conjugate stable modes with finite real frequency. These modes are localized to regions other than the center of the layer, often localized instead to new inflection points. Changes in $\langle B_x \rangle$ appear to separately introduce new modes at times as well, and we note that Tatsuno & Dorland (2006) have shown how nonuniform magnetic fields can destabilize shear flows in the absence of inflection points. The modes found here can form in addition to the existing unstable KH mode, can replace the KH mode with two conjugate pairs of finite-frequency modes, or can emerge after the KH modes have already stabilized at that wavenumber, such as the $k_x \geq 0.4$ unstable modes that emerge around $t \approx 60$ in Fig. 4.13. Each mode's complex frequency is well within the bounds of the modified semicircle theorem derived by Hughes & Tobias (2001). While these complications could be avoided by replacing the mean flow with a fitted, broadened tanh profile of the form $U = \tanh(z/d)$, the mean flow does not resemble such a profile. This is demonstrated in the MHD simulations in Palotti et al. (2008) and Mak et al. (2017) as well as the hydrodynamic experiments of Gaster et al. (1985) (see their Eqn. (5.2) and Fig. 2), with Wu & Zhuang (2016) (see their Table 1) showing that these discrepancies cause significant changes to the eigenmode structure and even the range of unstable wavenumbers. A detailed investigation of these modes, such as

their scaling with different system features, their effects on transport, or their use in reduced models, is beyond the scope of this work.

Figure 4.14 shows mode amplitudes for the most unstable and conjugate stable mode for the four initially-unstable wavenumbers for a simulation with $M_A = 40$ and $\text{Rm} = 500$, calculated using both the modes of the original equilibrium and of the mean flow at each time. Leading into saturation, both sets of amplitudes are consistent with expectations in

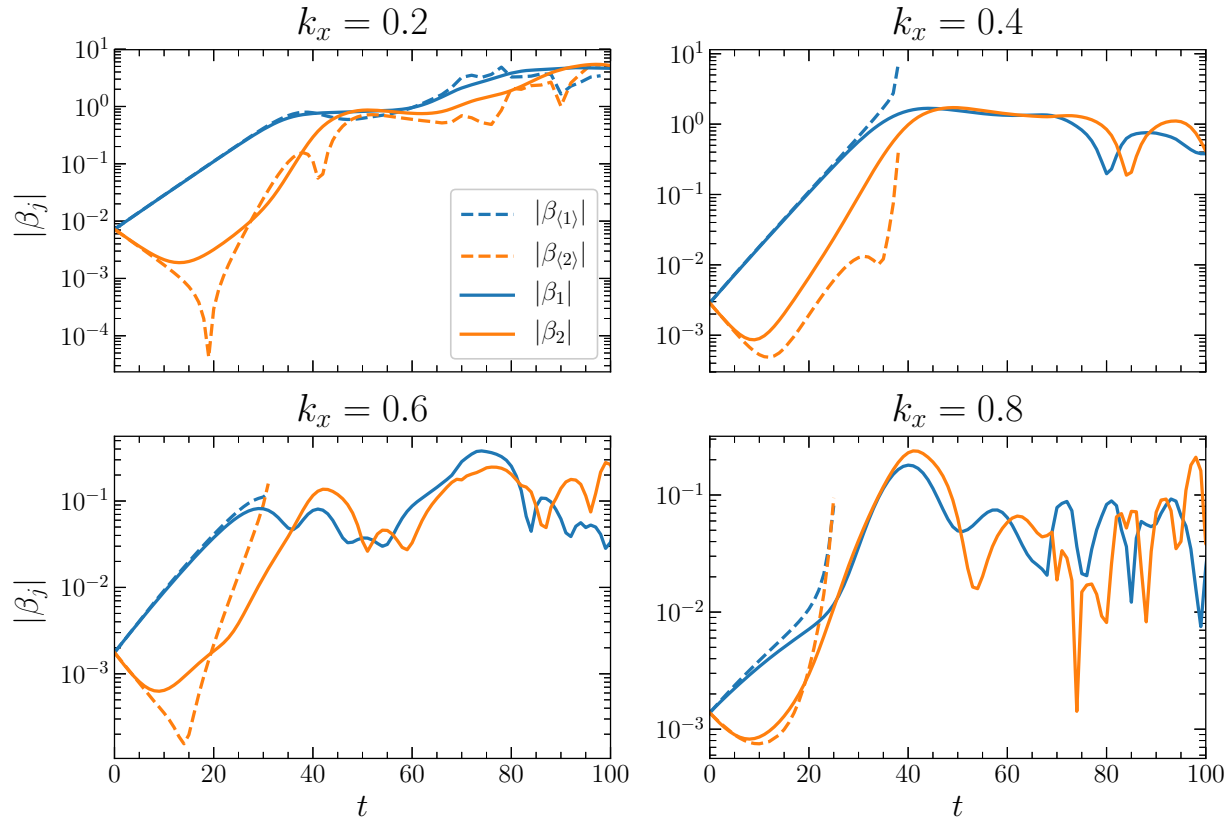


Figure 4.14 Mode amplitudes of the most unstable (blue) and conjugate stable (orange) modes for the same simulation as in Fig. 4.13. Dashed lines are mode amplitudes using a basis of eigenmodes of perturbations about the mean flow and field, solid lines are using eigenmodes of perturbations about the initial equilibrium.

systems where unstable modes nonlinearly drive stable modes (Terry et al. 2006; Makwana et al. 2011; Fraser et al. 2017, 2018), with the stable mode decaying linearly before being nonlinearly driven while the unstable mode is still growing linearly. Periods where $|\beta_2|$ appears to grow at the same rate as $|\beta_1|$, when it is expected to and eventually does grow faster, can be attributed to differences between \vec{f}_j and the more relevant $\vec{f}_{\langle j \rangle}$.⁷ Instances where the $|\beta_{\langle 2 \rangle}|$ decreases briefly and dramatically before quickly increasing again can be attributed to a difference in the complex phases of different terms on the right-hand side of Eq. (C8): when one term overtakes another and becomes dominant, $\beta_2(t)$ briefly passes through or near 0 in the complex plane before growing in amplitude.

Figure 4.6 showed that the sign of $|\beta_2|^2 - |\beta_1|^2$ at a given wavenumber corresponds to the sign of the Reynolds stress for that wavenumber, $\tau_u(k_x)$, evaluated at $z = 0$. Whenever $\tau_u(k_x)$ reverses for a given wavenumber and drives counter-gradient momentum transport, $|\beta_2|$ surpasses $|\beta_1|$ at that wavenumber. Figure 4.14 shows that this holds for $\beta_{\langle j \rangle}$ and β_j despite the concerns regarding the latter described above. Meanwhile, the eigenmodes

⁷Suppose the true stable mode amplitude in some system evolves as $\beta_2(t) = \beta_2(0)e^{-|\gamma|t} + \beta_1^2(t)$, and the unstable mode amplitude as $\beta_1(t) = \beta_1(0)e^{|\gamma|t}$ (see Terry et al. 2006, Eqns. (22-25)). If a mode that differs slightly from \vec{f}_2 is used to calculate $\beta_2(t)$ from simulation data, then an error of the form $\epsilon\beta_1$ will almost always be introduced. This will cause the apparent stable mode amplitude to briefly evolve as $\beta_2(t) \sim \epsilon\beta_1(t)$ before the $\beta_2(t) \sim \beta_1^2(t)$ term becomes dominant if $|\epsilon| \gtrsim |\beta_1(0)|$. If the modes are nonorthogonal under the inner product used to calculate β_j , then ϵ can become quite large for even small differences in \vec{f}_2 .

of the mean flow/field become difficult to interpret once the unstable KH mode stabilizes or is replaced by multiple finite-frequency modes. While we have shown that magnetic fields generally bring the quantity $|\beta_2|^2 - |\beta_1|^2$ closer to 0, thus far we have not identified whether that occurs by decreasing both mode amplitudes or by decreasing their ratio. For this reason, Fig. 4.15 shows $|\beta_1|$ and $|\beta_2|$ over time at $k_x = 0.2$ and 0.4 for three different M_A . Generally, decreasing M_A causes both mode amplitudes to decrease and also brings them closer to equipartition.

4.5.5 Approximating fluctuations with truncated eigenmode decompositions

Fraser et al. (2018) studied a driven shear flow and found that the fluctuating flow and Reynolds stress at the relevant scales could be approxi-

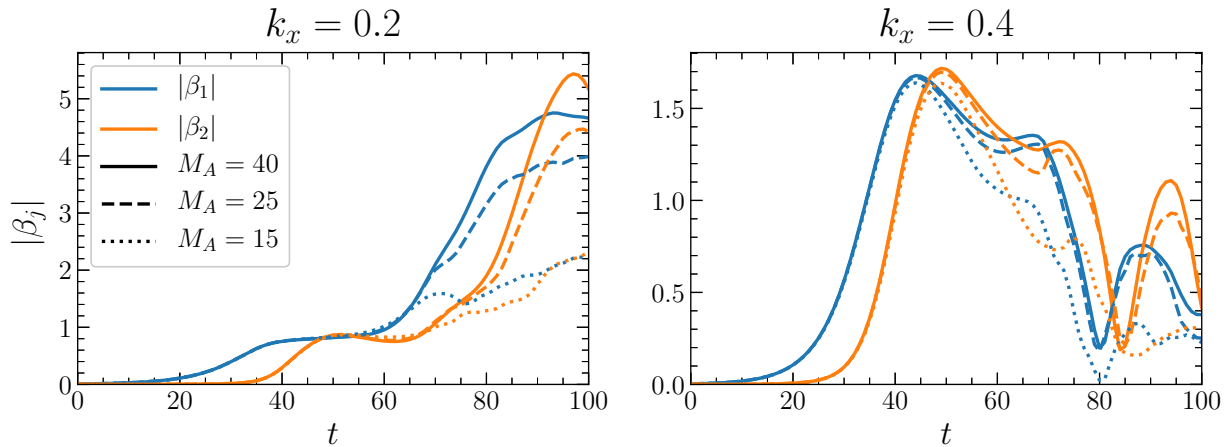


Figure 4.15 Mode amplitudes $|\beta_2|$ (orange) and $|\beta_1|$ (blue) at $k_x = 0.2$ (left) and 0.4 (right) for $M_A = 40$ (solid), 25 (dashed), and 15 (dotted lines). As M_A decreases, both mode amplitudes are reduced while also trending closer towards equipartition.

mated by truncating the summation in Eq. (4.12) to simply two eigenmodes per horizontal wavenumber, where one was the unstable KH mode and the other its conjugate stable mode. Reduced models for the scaling of momentum transport with the external forcing were constructed using this approximation and were compared to models where only the unstable mode was considered. In parameter regimes where stable modes reached significant amplitudes, the models performed significantly better when stable modes were included; in regimes where stable modes were suppressed relative to unstable modes, the two models performed equally well. This served as a useful metric for assessing how stable mode activity varied with system parameters. Here, we employ the same methods as an additional metric to demonstrate the reduction of stable mode activity with increasing field strength.

Figures 4.16-4.18 show, as functions of time, the resulting errors when the state \hat{f} at a given k_x is approximated by truncating the summation in Eq. (4.12) to a subset of eigenmodes. Two errors, one for ϕ and one for ψ , are calculated according to

$$\text{err}_\phi = \frac{\|\hat{\phi}_{\text{exact}} - \hat{\phi}_{\text{approx}}\|_{\text{KE}}^2}{\|\hat{\phi}_{\text{exact}}\|_{\text{KE}}^2}, \quad (4.13)$$

and

$$\text{err}_\psi = \frac{\|\hat{\psi}_{\text{exact}} - \hat{\psi}_{\text{approx}}\|_{\text{ME}}^2}{\|\hat{\psi}_{\text{exact}}\|_{\text{ME}}^2}, \quad (4.14)$$

where $\|\hat{\phi}\|_{\text{KE}}^2$ and $\|\hat{\psi}\|_{\text{ME}}^2$ are the kinetic and magnetic energy of a given $\hat{\phi}$ and $\hat{\psi}$. Figures 4.16 and 4.17 correspond to the $k_x = 0.2$ and $k_x = 0.4$ fluctuations, respectively, for the simulation in Fig. 4.14, while Fig. 4.18 corresponds to $k_x = 0.2$ fluctuations in an identical simulation but with $M_A = 7.5$. In each figure, approximations using both \vec{f}_j and $\vec{f}_{\langle j \rangle}$ are compared. When quasilinear flattening stabilizes modes at a given wavenumber, approximations built using eigenmodes of the mean flow and field become unreliable. However, even when quasilinear flattening has set in, approxima-

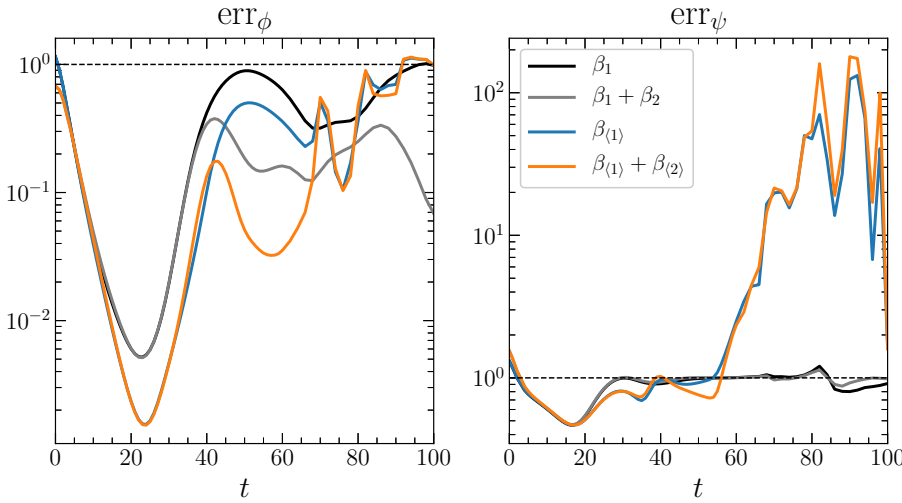


Figure 4.16 Error over time for approximations of the flow (left) and field (right) at $k_x = 0.2$ using a truncated eigenmode expansion for a simulation with $M_A = 40$ and $\text{Rm} = 500$. Black and grey curves use β_j and \vec{f}_j , while other curves use $\beta_{\langle j \rangle}$ and $\vec{f}_{\langle j \rangle}$. The horizontal dashed line indicates an error of 1. Flow fluctuations are well-described when stable modes are included, with $\beta_{\langle j \rangle}, \vec{f}_{\langle j \rangle}$ models performing better than the β_j, \vec{f}_j ones. Each approximation describes magnetic fluctuations poorly.

tions using eigenmodes of the initial equilibrium retain some fidelity. Before quasilinear flattening stabilizes modes, the $\vec{f}_{\langle j \rangle}$ modes generally describe fluctuations better. This is expected given that they reflect the broadening of the layer with time, which was shown in plots of τ_u in Sec. 4.5.3 to cause the fluctuations to broaden as well. For higher M_A , including the conjugate stable mode in the expansion significantly reduces the error in the approximated flow, particularly when counter-gradient momentum transport occurs. This further demonstrates the significance of the stable mode activity in these systems. At lower M_A , including the conjugate stable mode in the expansion makes comparatively less of a difference in the error, reflecting that stable modes have less of an impact when the magnetic field is strong. For all cases explored, these approximations have very little success in describing the field fluctuation. This may indicate that the flow at these scales is dominated more by interactions with the mean flow and stable and unstable modes at large scales, while the field is dominated by more complex interactions.

4.6 Conclusions

In turbulence driven by unstable, freely-evolving shear layers in MHD, the addition of a magnetic field has been observed to enhance energy transfer to small scales and increase turbulent momentum transport (Palotti

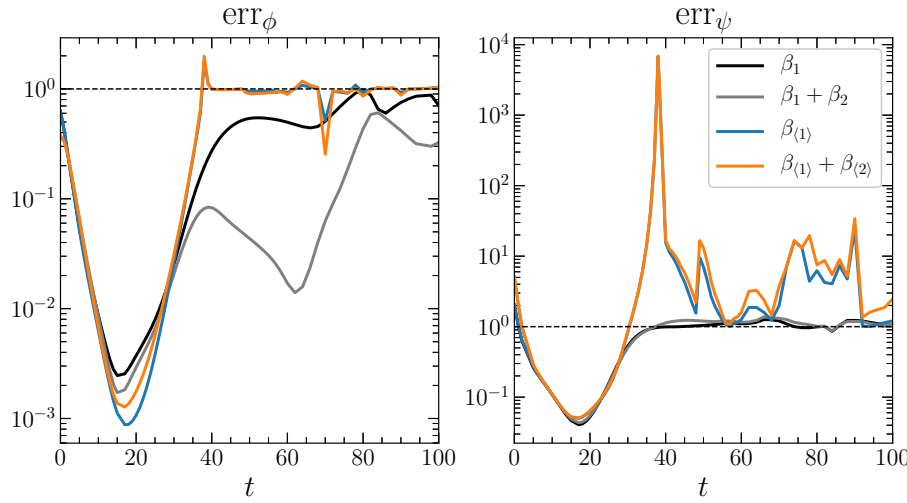


Figure 4.17 Identical to Fig. 4.16, but the $k_x = 0.4$ fluctuations are approximated. Unlike the $k_x = 0.2$ fluctuations, here the \vec{f}_j modes describe the system well for significantly longer than the $\vec{f}_{\langle j \rangle}$ modes, except near $t \approx 20$. This is to be expected as $\gamma_{\langle j \rangle}$ approaches 0 much sooner at this k_x .

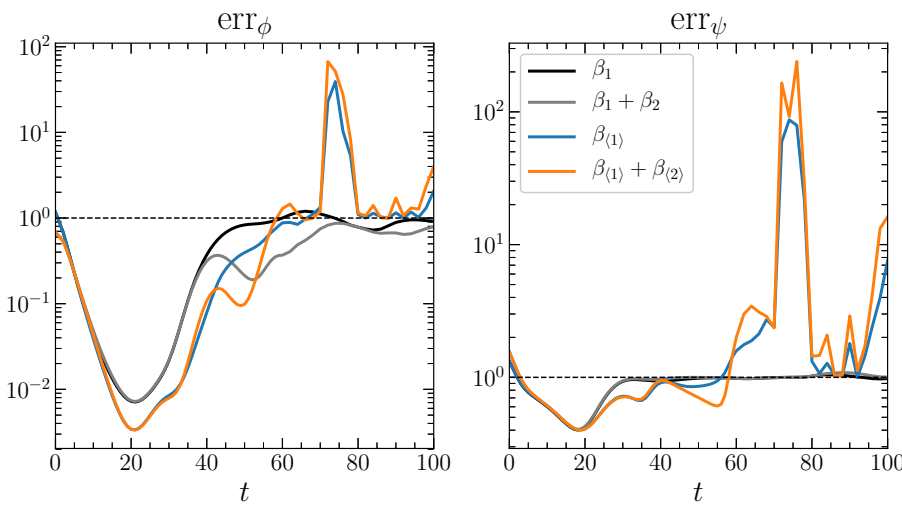


Figure 4.18 Identical to Fig. 4.16, but for $M_A = 7.5$. Here, including the stable mode makes less of an improvement to the approximations, consistent with them playing less of a role in the dynamics at lower M_A .

et al. 2008; Mak et al. 2017) despite stabilizing the driving instability (Chandrasekhar 1961). Here, we have investigated the role of large-scale, dissipationless stable modes in this system in an effort to identify a cause for these trends. In the MHD system, as in other systems where dissipationless stable modes have been investigated (Fraser et al. 2017, 2018), these modes transfer energy from large-scale fluctuations back to the driving momentum gradient when they are significantly excited. This shrinks the shear layer and reduces the energy in fluctuations that might otherwise cascade to smaller scales. Thus, one might expect that the enhanced transfer to small scales and increased broadening rate with stronger magnetic fields is consistent with less stable mode activity. We have shown this to be the case.

In Fraser et al. (2018), changes in stable mode activity with an added damping term could be predicted based on how the damping affected the eigenvalues. Here, changes in stable mode activity as equilibrium field strength is varied cannot be predicted from changes in eigenvalues alone. This is due to the magnetic field preserving the conjugate symmetry between stable and unstable modes such that stable modes have damping rates exactly equal to the growth rates of unstable modes at the same scales. Instead, to demonstrate that the observed trends can be understood in terms of these modes, we rely on post-processing analyses of direct numerical

simulations of the system. We use these analyses to track the amplitudes of stable and unstable modes through the evolving turbulence, finding that stable mode activity becomes less prominent at stronger fields. This is demonstrated first by identifying the relationship between Reynolds stress and the relative excitation of stable and unstable modes, allowing Reynolds stress to serve as a proxy for stable mode activity. As field strength increases, the momentum transport corresponding to stable mode activity becomes less prominent for two reasons. At some times, particularly later in the simulation when the field has amplified, this is partly because the counter-gradient Reynolds stress caused by stable modes becomes weaker. At other times, it is entirely because the down-gradient Maxwell stress due to small-scale magnetic fluctuations becomes stronger with stronger fields. As an additional means to demonstrate this trend in stable mode activity, turbulent fluctuations are approximated using combinations of stable and unstable modes, then compared to approximations in terms of unstable modes alone. In the same regimes where stable modes are seen to be less prominent, their inclusion in these approximations provides less of an improvement. In performing these analyses, we have found that the same eigenmode decompositions used in systems with a fixed or otherwise quasi-stationary unstable profile driving the turbulence are also effective in this

system, where the mean flow that drives instability changes in time.

Simulations with a sufficiently weak magnetic field appear to evolve nearly hydrodynamically provided that Rm is not sufficiently large to permit significant field amplification. However, even for very weak magnetic fields, the reduction in stable mode activity relative to the hydrodynamic case leads to more energy cascading to small scales, especially in the form of magnetic fluctuations. This drives an increase in resistive dissipation that generally exceeds the viscous dissipation in the hydrodynamic case, with this dissipation *increasing* with Rm for the small range of values studied here. Viscous dissipation increases with field strength as well, provided the field is stronger than some threshold that depends on Rm . Thus, even in the presence of a magnetic field much too weak to significantly affect the linear instability, free shear layers in MHD seem to dissipate energy much faster than the hydrodynamic counterpart, with the reduction of stable mode activity providing an underlying explanation.

A Constructing a basis with the linear modes

Here we describe how the eigenmodes obtained from solving Eqs. (4.5) and (4.6) are used to form a basis for a vector space, and how their amplitudes are tracked over time in nonlinear simulations of Eqs. (4.1) and (4.2).

First, just as the notation \vec{f}_j was introduced in Sec. 4.2.2 out of convenience to represent an entire eigenmode, including both its ϕ and ψ components, we rewrite Eqs. (4.5) and (4.6) as

$$i\omega \hat{\mathcal{M}}[\hat{f}] = \hat{\mathcal{L}}[\hat{f}], \quad (\text{A1})$$

where $\hat{\mathcal{M}}$ and $\hat{\mathcal{L}}$ are 2×2 matrices representing the coefficients and linear differential operators acting on $\hat{\phi}$ and $\hat{\psi}$ in Eqs. (4.5) and (4.6), and $\hat{f} \equiv (\hat{\phi}, \hat{\psi})$. Hats over quantities are meant to indicate that they correspond to the Fourier-transformed (in x) system, but the hat is suppressed when referring to eigenmodes \vec{f}_j . The matrix $\hat{\mathcal{M}}$ being different from simply the identity operator makes this system a *generalized* eigenvalue problem, unlike the linearized equations considered in Hatch et al. (2011), Terry et al. (2014), and Fraser et al. (2018), and thus requires modifications to the methods employed in those papers for calculating mode amplitudes.

At a given k_x , suppose the eigenmodes \vec{f}_j of Eq. (A1) form a complete basis in the sense that for any state \hat{f} , the component corresponding to that k_x can be expressed as a linear combination of eigenmodes of the form

$$\hat{f}(k_x, z) = \sum_j \beta_j(k_x) \vec{f}_j(k_x, z), \quad (\text{A2})$$

where β_j is the amplitude of mode \vec{f}_j , and can be thought of as a coordinate in the eigenmode basis. We verify that the eigenmodes in our numerical

calculations are complete by checking that they are linearly independent and that the number of eigenmodes returned by the solver, including those on the continuum of marginally stable modes (Case 1960), matches the degrees of freedom (product of the z resolution and the number of fields). In finite-dimensional systems such as the numerically-discretized system here, this implies that, for any given \hat{f} , the amplitudes β_j in Eq. (A2) are unique. Note that these notions of completeness, linear independence, and uniqueness are all well-defined without needing to introduce an inner product (Axler 1997). Hence, while the eigenmodes \vec{f}_j in the system considered here are certainly non-orthogonal under standard choices of inner product, the mode amplitudes β_j are well-defined and unique. Furthermore, while we do use an inner product, as described below, to calculate the mode amplitudes in practice – and the eigenmodes are indeed non-orthogonal under this inner product – *the resulting mode amplitudes are independent of the choice of inner product used.* This is one benefit of considering mode amplitudes in favor of what are called *projections* in recent gyrokinetic studies (Pueschel et al. 2016; Faber et al. 2018; Whelan et al. 2018, 2019; Pueschel et al. 2019), and have also been employed in at least one recent hydrodynamic study (Dong et al. 2019), where they were identified as the cosines of the familiar *Hermitian angles* (see brief review by Scharnhorst 2001) between

the state vector and the eigenvectors. The Hermitian angles are often more straightforward to calculate in practice,⁸ and have intuitive interpretations when the cosine is 0 or 1 (e.g. their usage in Dong et al. (2019)), but they depend on the choice of inner product. While mode amplitudes are sometimes less straightforward to calculate in practice, they can directly inform reduced models when some nonlinear interactions can be neglected in favor of others (Terry et al. 2009, 2018; Hegna et al. 2018) or when the system state is well-described by a severe truncation of the set of eigenmodes (Fraser et al. 2018). Furthermore, equations for their time-evolution can be directly constructed from the original equations governing the system (Terry et al. 2006; Makwana et al. 2011; Fraser et al. 2017) by a change of basis from the dynamical fields to the eigenmodes. Note that if the eigenmodes are mutually orthonormal under some inner product, then the cosine of the hermitian angle and the mode amplitudes are equivalent up to a factor of the norm (induced by that inner product) of the state vector.

Calculating the mode amplitudes of a given state from a nonlinear simulation can be done by constructing a set of modes $\{\vec{g}_i\}$ that, with the eigenmodes $\{\vec{f}_j\}$, form a biorthogonal system under some chosen inner

⁸Indeed, at the time of this writing, potentially-significant code development would be necessary to calculate the amplitudes of eigenmodes obtained with the iterative eigenvalue solvers employed by the GENE code. These iterative solvers are often necessary given the massive matrices encountered in fully 5D gyrokinetic calculations. Iterative solvers were not necessary in Fraser et al. (2018) because only two spatial dimensions were considered.

product $\langle \cdot, \cdot \rangle$ such that $\langle \vec{g}_i, \vec{f}_j \rangle = \delta_{i,j}$, where $\delta_{i,j}$ is the Kronecker delta. Once this so-called dual basis $\{\vec{g}_i\}$ is obtained, the mode amplitudes β_j in Eq. (A2) can be calculated according to $\beta_j = \langle \vec{g}_i, \hat{f} \rangle$. In previous work (Hatch et al. 2011; Terry et al. 2014; Fraser et al. 2018), the linearized equations were analogous to Eq. (A1), but $\hat{\mathcal{M}}$ was simply the identity operator, so that the linearized system was an ordinary eigenvalue problem, i.e., $\hat{\mathcal{L}}[\vec{f}_j] = i\omega_j \vec{f}_j$, rather than a generalized eigenvalue problem. For ordinary eigenvalue problems in finite-dimensional vector spaces, if $\hat{\mathcal{L}}$ is diagonalizable, then the dual basis $\{\vec{g}_i\}$ is given by the eigenmodes of $\hat{\mathcal{L}}^\dagger$, which we denote as $\vec{g}_i = \vec{f}_i^\dagger$. Here $\hat{\mathcal{L}}^\dagger$ is the Hermitian adjoint of $\hat{\mathcal{L}}$ with respect to some inner product $\langle \cdot, \cdot \rangle$.⁹ Note that the notion of Hermitian adjoint requires selecting an inner product, which is then the inner product under which $\{\vec{f}_i^\dagger\}$ and $\{\vec{f}_j\}$ form a biorthogonal system. If $\hat{\mathcal{L}}$ is an $N \times N$ matrix rather than a linear differential operator, as is the case when doing numerical calculations with finite resolution, then the left and right eigenvectors of $\hat{\mathcal{L}}$ form a biorthogonal system under the usual complex dot product. This was used to calculate the mode amplitudes in Hatch et al. (2011), Terry et al. (2014), and Fraser et al. (2017).

When dealing with a generalized eigenvalue problem, as in Eq. (A1), it

⁹If $\hat{\mathcal{L}}$ is self-adjoint, i.e., $\hat{\mathcal{L}}^\dagger = \hat{\mathcal{L}}$, then $\vec{f}_j^\dagger = \vec{f}_j$ and the eigenmodes, properly normalized, form an orthonormal basis so that the mode amplitudes can be calculated in the more familiar way: $\beta_j = \langle \vec{f}_j, \hat{f} \rangle$.

can be shown that the eigenmodes \vec{f}_i^\dagger of the adjoint system

$$\hat{\mathcal{L}}^\dagger[\vec{f}_i^\dagger] = -i\omega_i^* \hat{\mathcal{M}}^\dagger[\vec{f}_i^\dagger] \quad (\text{A3})$$

satisfy a modified form of biorthogonality, namely $\langle \vec{f}_i^\dagger, \hat{\mathcal{M}}[\vec{f}_j] \rangle = \delta_{i,j}$, or, equivalently,

$$\langle \hat{\mathcal{M}}^\dagger[\vec{f}_i^\dagger], \vec{f}_j \rangle = \delta_{i,j}. \quad (\text{A4})$$

This provides our dual basis $\{\vec{g}_i\}$ that can be used to calculate the mode amplitudes: for any state \hat{f} given by Eq. (A2), the mode amplitudes can be calculated using

$$\beta_j = \langle \hat{\mathcal{M}}^\dagger[\vec{f}_i^\dagger], \hat{f} \rangle. \quad (\text{A5})$$

The mode amplitudes discussed in Sec. 4.5.4 were calculated using this expression. Note that the normalization of the eigenmodes affects the resulting mode amplitudes. In this work, all eigenmodes are normalized to have unit total energy, so that if a state is given by Eq. (A2) where only a single β_j is nonzero, then the energy of the state is by $|\beta_j|^2$. Additional details particular to this system and the Dedalus code are described in Appendix B

B Details of inner product used in this work

Every eigenmode we use in this work is obtained from a finite Chebyshev series representation of the ideal system Eqs. (4.5) and (4.6). Thus, all

linear operators and modes become finite-dimensional matrices and vectors, with entries given by their Chebyshev series expansion coefficients for each of the fields. In this work, the inner product $\langle \cdot, \cdot \rangle$ that is used for adjoints and mode amplitudes is the ordinary complex dot product in terms of these Chebyshev series coefficients for each field. As a result of Dedalus only solving formally first-order differential systems of equations, the fields relevant to the present system, for example, are not just ϕ and ψ , but also their derivatives in z . The summation over the Chebyshev series coefficients for this inner product includes a summation over each of these fields as well. While this is not a physically motivated inner product, such as an energy-based inner product, it is practically convenient. Under this inner product, the matrix of some operator's Hermitian adjoint is simply the conjugate transpose of the original matrix. Thus, calculating left eigenvectors with Dedalus, which requires replacing the eigenvalue problem Eq. (A1) with its adjoint Eq. (A3), is easily done by modifying the code to apply conjugate transposes to the matrices $\hat{\mathcal{M}}$ and $\hat{\mathcal{L}}$ before they are passed to the underlying linear algebra packages.

C Nonlinear coupling of linear modes

Using the biorthogonality relation Eq. (A4) provides mode amplitudes from a given system state according to Eq. (A5), which was used to calculate

mode amplitudes from nonlinear simulations in this work. If, instead of the state \hat{f} , an appropriate inner product with the governing equations is considered, one obtains the governing equations in the eigenmode basis.

In Appendix A, the linearized system Eqs. (4.5) and (4.6) was written in a generic form given by Eq. (A1). Here, we similarly consider a generic form of the nonlinear equations for the perturbations, Eqs. (4.3) and (4.4), given by

$$\frac{\partial}{\partial t} \vec{\mathcal{M}}[\vec{f}] = \vec{\mathcal{L}}[\vec{f}] + \vec{\mathcal{N}}[\vec{f}, \vec{f}], \quad (\text{C6})$$

where $\vec{\mathcal{N}}$ is a bilinear operator.

For systems of this form, taking the inner product of the equations with \vec{f}_j^\dagger on the left yields

$$\frac{\partial}{\partial t} \beta_j = i\omega_j \beta_j + \langle \vec{f}_j^\dagger, \vec{\mathcal{N}}[\vec{f}, \vec{f}] \rangle, \quad (\text{C7})$$

which can be compared to Eq. (9) in Terry et al. (2006) or Eq. (16) in Fraser et al. (2017).¹⁰ Expanding each \vec{f} in the nonlinearity according to Eq. (A2) allows this to be rewritten as

$$\frac{\partial}{\partial t} \beta_j = i\omega_j \beta_j + \sum_{m,n} \langle \vec{f}_j^\dagger, \vec{\mathcal{N}}[\vec{f}_m, \vec{f}_n] \rangle \beta_m \beta_n. \quad (\text{C8})$$

¹⁰Some abuse of notation is committed here for the sake of brevity. The methods described in Appendix A were considered in the context of separate k_x in systems that had been Fourier transformed. Thus, either each of the equations in this Appendix should be replaced by their Fourier transforms, which would introduce cumbersome notation as the nonlinearities become convolutions and $\vec{\mathcal{N}}$ would then depend on k_x and k'_x , or the subscript j must be understood to enumerate the eigenmodes at all wavenumbers and the inner product understood to include an integral in x . These details do not aid the discussion and are left out.

This is equivalent to Eqs. (4.3) and (4.4), but expressed in terms of eigenmode amplitudes β_j rather than the physical fields ϕ and ψ . The second term on the right-hand side describes three-mode nonlinear interactions, specifically how mode j is influenced by nonlinear interactions with modes m and n , and can be understood as the same nonlinearities in Eqs. (4.3) and (4.4) written in the eigenmode basis.¹¹ The complex numbers $\langle \vec{f}_j^\dagger, \vec{\mathcal{N}}[\vec{f}_m, \vec{f}_n] \rangle$ are called nonlinear coupling coefficients, and have been calculated by different means in previous work on stable modes in instability-driven turbulence (Terry et al. 2006; Makwana et al. 2011) as well as an unstable shear flow (Fraser et al. 2017). Others have derived them in Dedalus using the same methods as what is presented here in order to study nonlinear coupling of p- and g-modes in binary neutron stars Burns (2018). If these coefficients are nonzero for couplings involving two unstable modes and a stable mode, then the stable mode is nonlinearly driven by unstable modes despite its negative linear growth rate.

The remainder of this appendix presents calculations of these coupling coefficients and demonstrates their use for the system at hand. We calculate

¹¹Note that the derivation of Eq. (C8) implicitly assumes that \vec{f}_j and \vec{f}_j^\dagger are independent of time. If they do vary with time, then additional linear terms that are off-diagonal appear in Eq. (C8), just like the terms proportional to the time derivative of the Hamiltonian that appear when considering adiabatically-changing potentials in quantum mechanics (see e.g. Sakurai & Napolitano 2017, Eqn. (5.6.10)). This can be shown by following standard textbook methods for analyzing adiabatically-changing potentials, with care taken to respect that the linearized system here is a generalized eigenvalue problem and is not self-adjoint.

for a range of different M_A the nonlinear coupling coefficients that involve various combinations of unstable and stable modes. These are then used to calculate the threshold parameter P_t (described below) to assess whether nonlinearities involving both stable and unstable modes play a significant role in saturating the linear instability relative to nonlinearities involving unstable modes alone, and how this assessment varies with M_A . We include these results here as a demonstration of how the method above can be employed and because the results are consistent with the trends observed in nonlinear simulations. However, there remain subtle details in the results suggesting a small possibility that a minor error exists in the numerical implementation of the methods described here. These potential errors could not be fully resolved in time for submission of this thesis. The results are included nonetheless for the reasons described above, but the reader is cautioned to note these potential errors.

After obtaining appropriate left and right eigenvectors with Dedalus, the vector $\vec{\mathcal{N}}[\vec{f}_m, \vec{f}_n]$ is constructed by inserting two right eigenvectors into the nonlinearities in Eqs. (4.3) and (4.4). Here, each vector includes a variety of fields as its components (see Appendix B), and care is taken to insert the appropriate fields into the nonlinearities, and to map these nonlinearities onto the appropriate field components of the vector $\vec{\mathcal{N}}$. Because the

nonlinearities in the original equations are only present in the equations for $\partial_t \nabla^2 \phi$ and $\partial_t \psi$, only those components of the vector $\vec{\mathcal{N}}$ are nonzero. The equation for, e.g., $\partial_z \phi$ that is input into Dedalus is $\phi_z \equiv \partial_z \phi$, which contains no nonlinearities, and thus the ϕ_z component of $\vec{\mathcal{N}}$ is zero. The nonlinear coupling coefficients are then computed by taking the inner product shown in Eq. (C8). In the present system, the wavenumbers k_x for the modes \vec{f}_j^\dagger , \vec{f}_m , and \vec{f}_n are k_x , k'_x , and $k''_x \equiv k_x - k'_x$ respectively to satisfy the wavenumber matching condition, where each of these is nonzero. Just as an eigenvector's normalization affects the resulting mode amplitudes, it also affects the coupling coefficients. Here eigenvectors are normalized to have unit total energy.

Following the notation of Makwana et al. (2011) and Fraser et al. (2017), we write the nonlinear coupling coefficients involving only unstable and stable modes as $C_m(k_x, k'_x)$ if they enter into the equation for $\partial_t \beta_1(k_x)$ and $D_m(k_x, k'_x)$ if they enter into the equation for $\partial_t \beta_2(k_x)$, where $m = 1$ indicates a coupling to two unstable modes at k'_x and $k - k'_x$, $m = 2$ and 3 a coupling to one stable and one unstable mode, and $m = 4$ a coupling to two stable modes. A sampling of these coupling coefficients for $M_A = 40$ and $M_A = 15$ are shown in Fig. 4.19. From this figure alone, it is not clear what to make of the observed changes with M_A . An increase in $|C_1|$ with M_A

alone might not imply that couplings involving only unstable modes become more important if the other coefficients increase with M_A as well. For this reason, these coefficients are used to calculate the threshold parameter P_t .

For a derivation and detailed discussion of P_t see Terry et al. (2006). The parameter was similarly evaluated in Makwana et al. (2011). Here, P_t is calculated using the modified definition described in Fraser et al. (2017).

We calculate the ratio

$$P_t = \left[\frac{\max |2C_2\beta_1(k'_x)\beta_2(k''_x)|}{\max |C_1\beta_1(k'_x)\beta_1(k''_x)|} \right]_{t=t_s}, \quad (\text{C9})$$

where unstable modes are assumed to grow linearly, stable modes are as-

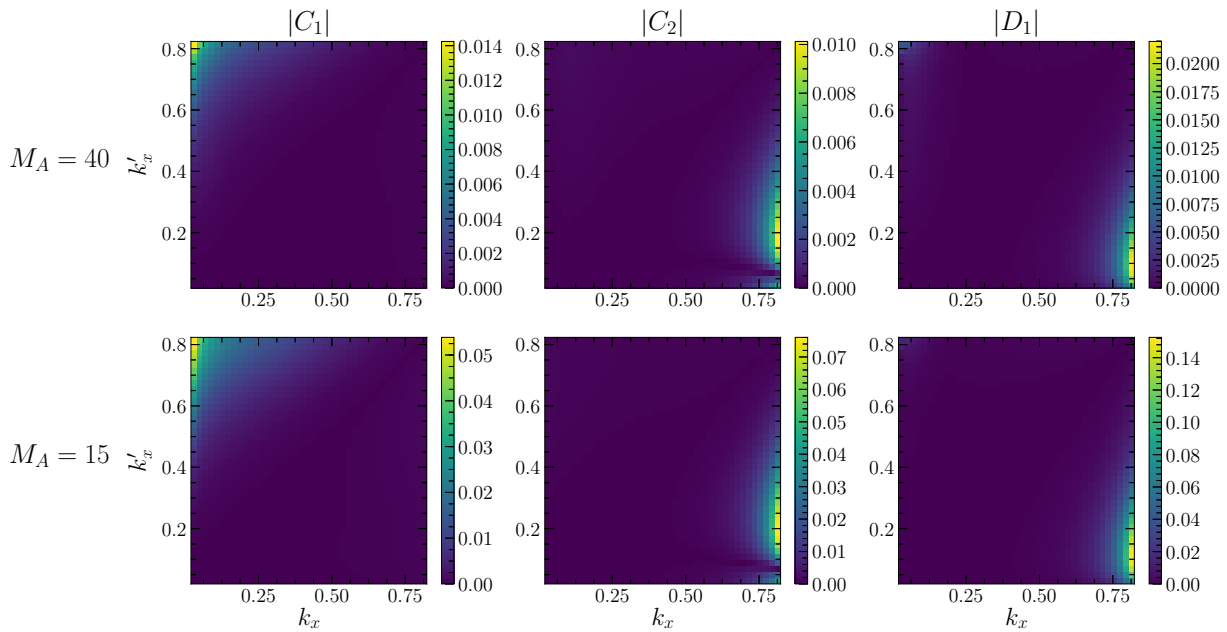


Figure 4.19 Coupling coefficients between stable and unstable modes for the equilibrium studied here. Top row corresponds to $M_A = 40$, bottom row to $M_A = 15$. In the notation of Eq. (C8), columns are, from left to right, $\langle \vec{f}_1^\dagger, \vec{\mathcal{N}}[\vec{f}_1, \vec{f}_1] \rangle$, $\langle \vec{f}_1^\dagger, \vec{\mathcal{N}}[\vec{f}_1, \vec{f}_2] \rangle$, and $\langle \vec{f}_2^\dagger, \vec{\mathcal{N}}[\vec{f}_1, \vec{f}_1] \rangle$. Data provided courtesy of J.M. Schroeder.

sumed to decay before being nonlinearly pumped as given by the parametric instability approximation (see Fraser et al. 2017, Eq. (21)), and t_s is the saturation time, defined here as the time at which the nonlinearity reaches the linear term in Eq. (C8) for the most unstable mode. The maximums taken in Eq. (C9) are over different values of k'_x , where k_x corresponds to the most unstable wavenumber. Unlike previous work, here the initial eigenmode amplitudes and complex phases are varied with k_x in the same fashion as the initial conditions of the nonlinear simulations in this chapter. This is done to ensure that trends in P_t with M_A are robust to different initial conditions. In calculating P_t , wavenumbers above $k_x = 0.83$ are neglected. As k_x approaches 1, numerical convergence becomes a challenge when calculating the eigenmodes. Even if growth rates are sufficiently converged, the coupling coefficients involve a product of three eigenmodes and P_t relies on multiple coupling coefficients. Thus, P_t is extremely sensitive to small errors in mode structures. Neglecting these wavenumbers is justified by their minimal energy content and contribution to saturation as observed in simulations. With these wavenumbers neglected, P_t is well-converged for $Nz = 4096$, which still allows for reasonable computation times using the sparse eigenvalue routines in Dedalus.

Results are shown in Fig. 4.20, where each curve represents a different

set of pseudo-random complex phases for the initial condition. Evidently P_t grows with increasing M_A for a variety of initial conditions. This is broadly consistent with the simulation results presented in this chapter, where stable modes are shown to dominate more at higher M_A . By comparing calculations of P_t to direct numerical simulations of a variety of systems, Makwana et al. (2011) found that $P_t \gtrsim 0.3$ implies stable modes are important contributors to instability saturation. Thus Fig. 4.20 appears to imply that stable modes are extremely important at all M_A . However, as discussed in Fraser et al. (2017), many of the assumptions built into this calculation become less valid if $|\beta_2|$ reaches amplitudes comparable to $|\beta_1|$, which indeed occurs for a broad range of M_A as shown in Fig. 4.15.

References

- Axler, S. 1997, Linear Algebra Done Right, Undergraduate Texts in Mathematics (Springer New York)
- Baines, P. G., & Mitsudera, H. 1994, Journal of Fluid Mechanics, 276, 327–342
- Biskamp, D. 2003, Magnetohydrodynamic Turbulence (Cambridge University Press)
- Burns, K. J. 2018, PhD thesis, Massachusetts Institute of Technology
- Burns, K. J., Vasil, G. M., Oishi, J. S., Lecoanet, D., & Brown, B. P. 2020, Physical Review Research, 2, 23068
- Carpenter, J. R., Tedford, E. W., Heifetz, E., & Lawrence, G. A. 2013, Applied Mechanics Reviews, 64, 060801

- Case, K. M. 1960, Physics of Fluids, 3, 143
- Chandrasekhar, S. 1961, Hydrodynamic and Hydromagnetic Stability (Oxford University Press)
- Dong, W., Tedford, E. W., Rahmani, M., & Lawrence, G. A. 2019, Phys. Rev. Fluids, 4, 063902
- Drazin, P. G. 2002, Introduction to Hydrodynamic Stability (Cambridge University Press)
- Drazin, P. G., & Reid, W. 1981, Hydrodynamic Stability (Cambridge University Press)
- Faber, B. J., Pueschel, M. J., Terry, P. W., Hegna, C. C., & Roman, J. E. 2018, Journal of Plasma Physics, 84, 905840503
- Fraser, A. E., Pueschel, M. J., Terry, P. W., & Zweibel, E. G. 2018, Physics of Plasmas, 25, 122303

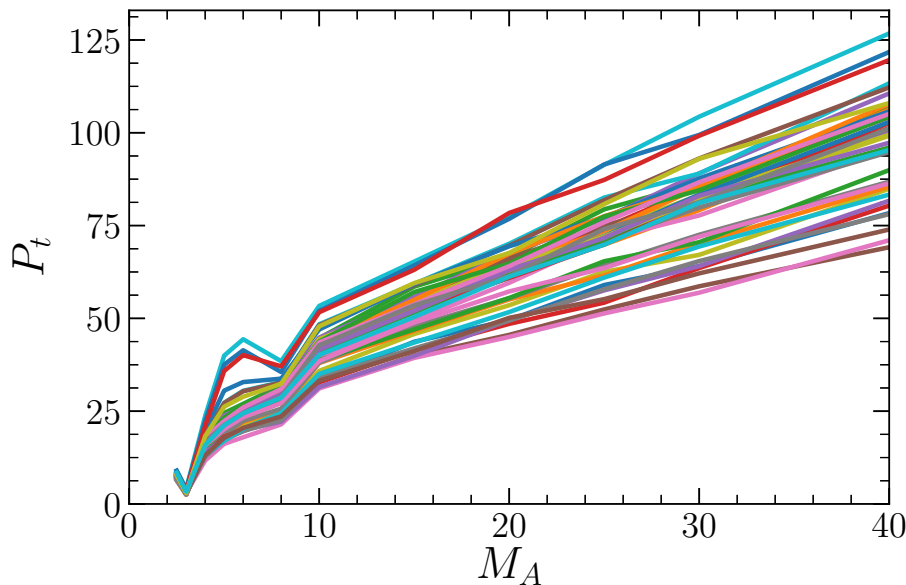


Figure 4.20 Threshold parameter P_t evaluated over a range of M_A . Each curve corresponds to a different set of pseudo-random complex phases for the initial eigenmode amplitudes, showing the extent to which trends are robust under different initial conditions. The decrease in P_t as M_A decreases suggests nonlinear coupling between stable and unstable modes becomes less dominant relative to unstable-only couplings at saturation for stronger fields. Data provided courtesy of J.M. Schroeder.

- Fraser, A. E., Terry, P. W., Zweibel, E. G., & Pueschel, M. J. 2017, Physics of Plasmas, 24, 062304
- Fraser, A. E., Terry, P. W., Zweibel, E. G., Pueschel, M. J., & Schroeder, J. M. 2020, Bulletin of the American Physical Society
- Gaster, M., Kit, E., & Wygnanski, I. 1985, Journal of Fluid Mechanics, 150, 23–39
- Hatch, D. R., Terry, P. W., Jenko, F., et al. 2011, Physics of Plasmas, 18, 055706
- Hegna, C. C., Terry, P. W., & Faber, B. J. 2018, Physics of Plasmas, 25, doi:10.1063/1.5018198
- Heifetz, E., & Guha, A. 2019, Phys. Rev. E, 100, 043105
- Heifetz, E., Mak, J., Nycander, J., & Umurhan, O. M. 2015, Journal of Fluid Mechanics, 767, 199–225
- Ho, C., & Huerre, P. 1984, Annual Review of Fluid Mechanics, 16, 365
- Hughes, D., & Tobias, S. 2001, Proceedings of the Royal Society of London. Series A: Mathematical, Physical and Engineering Sciences, 457, 1365
- Hurst, N. C., Danielson, J. R., Dubin, D. H. E., & Surko, C. M. 2020, Physics of Plasmas, 27, 042101
- Lecoanet, D., McCourt, M., Quataert, E., et al. 2016, Monthly Notices of the Royal Astronomical Society, 455, 4274
- Mak, J., Griffiths, S. D., & Hughes, D. W. 2017, Phys. Rev. Fluids, 2, 113701
- Makwana, K. D., Terry, P. W., Kim, J.-H. H., & Hatch, D. R. 2011, Physics of Plasmas, 18, 012302
- Makwana, K. D., Terry, P. W., Pueschel, M. J., & Hatch, D. R. 2014, Physical Review Letters, 112, 095002
- Palotti, M. L., Heitsch, F., Zweibel, E. G., & Huang, Y. 2008, The Astrophysical Journal, 678, 234–244
- Pueschel, M. J., Faber, B. J., Citrin, J., et al. 2016, Physical Review Letters, 116, 085001

- Pueschel, M. J., Hatch, D. R., Ernst, D. R., et al. 2019, *Plasma Physics and Controlled Fusion*, 61, 034002
- Sakurai, J. J., & Napolitano, J. 2017, *Modern Quantum Mechanics*, 2nd edn. (Cambridge University Press)
- Scharnhorst, K. 2001, *Acta Applicandae Mathematicae*, 69, 95
- Tatsuno, T., & Dorland, W. 2006, *Physics of Plasmas*, 13, 092107
- Terry, P. W., Baver, D. A., & Gupta, S. 2006, *Physics of Plasmas*, 13, 022307
- Terry, P. W., Baver, D. A., & Hatch, D. R. 2009, *Physics of Plasmas*, 16, 122305
- Terry, P. W., Faber, B. J., Hegna, C. C., et al. 2018, *Physics of Plasmas*, 25, 012308
- Terry, P. W., Makwana, K. D., Pueschel, M. J., et al. 2014, *Physics of Plasmas*, 21, 122303
- Weiss, N. O. 1966, *Proceedings of the Royal Society of London. Series A. Mathematical and Physical Sciences*, 293, 310
- Whelan, G. G., Pueschel, M. J., & Terry, P. W. 2018, *Physical Review Letters*, 120, 175002
- Whelan, G. G., Pueschel, M. J., Terry, P. W., et al. 2019, *Physics of Plasmas*, 26, 082302
- Wu, X., & Zhuang, X. 2016, *Journal of Fluid Mechanics*, 787, 396–439
- Zel'Dovich, Y. B., Ruzmaikin, A. A., Molchanov, S. A., & Sokoloff, D. D. 1984, *Journal of Fluid Mechanics*, 144, 1–11
- Zweibel, E. G. 1998, *Physics of Plasmas*, 5, 247

Chapter 5

Summary and Conclusions

5.1 Summary and conclusions

Shear flows are ubiquitous in physical systems, including several astrophysical examples. Understanding and predicting how shear-driven turbulence modifies the transport of heat, particles, and momentum across the flow is important to understanding how shear flows affect the evolution of systems where they are found. The work presented in this thesis has developed and employed a combination of analytical and numerical methods to probe how basic shear-flow instabilities saturate. Specifically, the role that large-scale stable (damped) eigenmodes play in saturation of the instability and their excitation in shear-flow-driven turbulence were investigated, and their utility in constructing reduced transport models was explored. Three separate studies were performed, each involving a different flow profile and including different physical effects. Despite these differences, each study found that stable modes are generally excited to the point that they affect instability saturation, can influence turbulent transport, and properly accounting for them can improve reduced models.

The nonlinear coupling between large-scale stable and unstable eigenmodes appears to be a fundamental aspect of KH-unstable flows. I describe it as fundamental because, while details unique to a given system may pro-

duce parameter regimes where their excitation is weak, they are present in any basic KH-unstable system. Indeed, their existence results from simple symmetries of the underlying equations (Qin et al. 2019; Zhang et al. 2020). Even when symmetry-breaking terms such as dissipation may appear to preclude their existence, separating the equations into dissipationless and dissipative components allows their role to be uncovered nonetheless, as was done in Chapters 3 and 4.¹ Barring their suppression, stable modes transport momentum up the equilibrium flow gradient and transfer energy back to the unstable flow. While this transfer of energy is conservative in the simulations presented here (unlike the important nonconservative damping that stable modes provide in other systems, e.g. Terry et al. 2006), it still affects the manner in which the instability saturates and the structure of the ensuing turbulence. Furthermore, understanding the dynamics in terms of these modes provides a useful framework for explaining trends with system parameters.

This framework is not only useful for qualitative understanding, but was shown here to directly inform quantitative reduced models. In the context of plasma turbulence driven by drift-wave instabilities, a variety of reduced

¹Furthermore, this separation allows their stability to be fully attributed to conservative energy transfer to the equilibrium. Stable modes investigated without this separation will include dissipative contributions to their linear dynamics.

models incorporating stable mode physics have been constructed (e.g. Terry et al. 2018; Hegna et al. 2018; Whelan et al. 2018). These range from mixing-length-like scaling relations to detailed statistical closure theories. These models have come after roughly two decades of work studying stable modes in drift-wave turbulence. Unlike the drift-wave case, the models presented in this thesis were not closed, and were thus incomplete. Mode amplitudes were inserted from simulations rather than calculated analytically. However, this thesis presents only the first three steps towards understanding the role of stable modes in shear-driven turbulence. After one or two decades of further study, I fully expect models similar to recent drift-wave turbulence theories to be possible here as well. The results presented here clearly indicate that such models merit investigation.

A final aspect of this work that bears highlighting is its relation to the large body of existing work on stable modes. The continued investigation of stable modes in local plasma turbulence has shown their excitation to be an almost universal aspect of these systems (e.g. Makwana et al. 2011). However, previous work had not considered non-local systems that do not lend themselves to assumptions of quasi-homogeneity. The KH instability is fundamentally non-local in the sense that uniform shear alone is insufficient to drive instability, and, in the shear layer problem, eigenmodes extend

on either side of the layer. Although this work only touched on the KH instability, demonstrating the importance of stable modes in these systems establishes that they are not limited to local systems alone. This motivates future work investigating their potential role in other instabilities including magnetorotational, Rayleigh-Taylor, Raleigh-Benard, or tearing modes, to name just a few examples. Wherever possible, the notation and methods presented in the appendices of Chapter 4 were generalized so that future studies in other systems can employ these same methods.

5.2 Future work

Several different future directions are motivated by or related to the work presented in this thesis. Here I briefly describe three of them, two of which are already underway by others, and one that I recently submitted as a postdoctoral fellowship proposal.

Stable modes in driven shear flows in MHD

The one that is most directly related is currently underway by a new PhD student. Comparing Chapters 3 and 4 of this thesis, the presence or absence of a flow-aligned magnetic field and the inclusion or lack of forcing were two significant differences between the systems. Some of the results, including the difficulty in describing magnetic fluctuations in Chapter 4,

could not be clearly attributed to the magnetic field or to lack of forcing. Similarly, it is unclear whether the reduction in stable mode activity with stronger magnetic fields is simply due to the enhanced layer broadening rate causing unstable modes to stabilize more quickly, thus reducing the time over which they nonlinearly drive stable modes. It is plausible that the trends with field strength would change significantly if the layer were maintained by a forcing similar to the one considered in Chapter 3, so that instability persists and a quasi-stationary state of driven turbulence ensues. A quasi-stationary state would also enable a more direct comparison to the eddy viscosity model presented in Parker & Constantinou (2019), and thus may enable a momentum transport model in which the Reynolds stress is described by stable and unstable modes while the Maxwell stress is described by a magnetic eddy viscosity.

Stable mode effects in unstable current sheets

In Williams (2019) (see Fig. 7.1 and surrounding discussion), a collisionless tearing instability was shown in the gyrokinetic framework to exhibit a conjugate stable mode similar to the stable modes studied here. Explicit resistivity can be shown to break any potential conjugate symmetry in a resistive MHD framework, thus precluding the existence of a lone stable

mode at large scales. However, the methods presented here can still be employed in the collisionless gyrokinetic case to study the conjugate stable mode. Alternatively, thanks to the flexibility of the Dedalus code, the same analyses applied to the KH system in Chapter 4 can be applied to fluid models of unstable current sheets. While the conjugate stable mode is not explicitly a part of the spectrum if resistivity is included, stable mode effects can still be investigated by proxy similar to the proxies motivated in Chapter 4. Alternatively, each of the large number of resistive stable modes found at large scales (see MacTaggart 2018, Fig. 1) can be inspected directly. By calculating their contributions to the energy in arbitrary perturbations, their conservative energy transfer to the mean can be separated from their nonconservative dissipation, similar to the different contributions to the Reynolds-Orr energy equation (see Drazin 2002, Sec. 5.3).

Understanding the turbulent interiors of stars: shear-flow instabilities and stable modes

Based on surface observation and asteroseismic inferences, radiation zones in stars across the Hertzsprung-Russel (HR) diagram are known to exhibit additional mixing of chemical composition and angular momentum beyond what is predicted by standard stellar models. I proposed to explore

these “missing mixing” problems and identify whether improved models of shear-driven turbulent transport can alleviate them. In the near future, I hope to study turbulence driven by *stratified* shear flows with and without magnetic fields in order to construct reduced models of turbulent transport. These models would be tested in parameter regimes (e.g. values of viscosity and diffusivity) that are accessible to simulations, then extrapolated to parameter regimes more relevant to stellar interiors.

This research would build on the work presented in this thesis on unstratified fluids and plasmas. Under the Boussinesq approximation, which is appropriate for stellar interiors (Spiegel & Veronis 1960), the conjugate symmetry between stable and unstable modes is preserved even with density stratification included (Chandrasekhar 1961). Thus, while significant coupling between the two modes in the stratified case remains to be demonstrated, one would expect that the unstratified case is approached in the limit of weak stratification, similar to the weak-field case exhibiting similar behavior to the hydrodynamic case in Chapter 4. Under the proposed research, parameter regimes where stable modes are or are not important would be distinguished using direct numerical simulations. The ability for the threshold parameter P_t to predict the importance of stable modes would be explored, with P_t calculated either using the methods of Chapter 2 or

Chapter 4. If P_t provides a valuable predictor, then it could be used in stellar evolution codes as a quick assessment at each timestep to determine whether existing turbulent transport models should be used (if stable modes are predicted to be unimportant at that time) or if they should be replaced with models that account for stable modes (if they are predicted to be important at that time). Thus, this work has the potential to yield simple improvements to stellar evolution codes that can then be tested to see whether improved models alleviate the missing mixing problems.

References

- Chandrasekhar, S. 1961, Hydrodynamic and Hydromagnetic Stability (Oxford University Press)
- Drazin, P. G. 2002, Introduction to Hydrodynamic Stability (Cambridge University Press)
- Hegna, C. C., Terry, P. W., & Faber, B. J. 2018, Physics of Plasmas, 25, doi:10.1063/1.5018198
- MacTaggart, D. 2018, Journal of Plasma Physics, 84, doi:10.1017/s0022377818001009
- Makwana, K. D., Terry, P. W., Kim, J.-H. H., & Hatch, D. R. 2011, Physics of Plasmas, 18, 012302
- Parker, J. B., & Constantinou, N. C. 2019, Phys. Rev. Fluids, 4, 083701
- Qin, H., Zhang, R., Glasser, A. S., & Xiao, J. 2019, Physics of Plasmas, 26, 032102
- Spiegel, E. A., & Veronis, G. 1960, Astrophysical Journal, 131, 442
- Terry, P. W., Baver, D. A., & Gupta, S. 2006, Physics of Plasmas, 13, 022307
- Terry, P. W., Faber, B. J., Hegna, C. C., et al. 2018, Physics of Plasmas, 25, 012308
- Whelan, G. G., Pueschel, M. J., & Terry, P. W. 2018, Phys. Rev. Lett., 120, 175002
- Williams, Z. R. 2019, PhD thesis, University of Wisconsin-Madison
- Zhang, R., Qin, H., & Xiao, J. 2020, Journal of Mathematical Physics, 61, 012101